Z. Kristallogr. 214 (1999) 14–56

Complex surface structures studied by low-energy electron diffraction

M. Gierer[I] and H. Over[II]

[I] Ludwig-Maximilians-Universität München, Institut für Kristallographie, Theresienstr. 41, D-80333 München, Germany
[II] Fritz-Haber-Institut der Max-Planck-Gesellschaft, Faradayweg 4–6, D-14195 Berlin, Germany

Received July 15, 1998; accepted July 20, 1998

Dedicated to the 75th birthday of Professor Franco Jona, one of the pioneers in LEED

Contents

Abstract. Structural results of complex surface structures determined by employing the method of low-energy electron diffraction (LEED) are reviewed. LEED is the prime crystallographic technique in surface science, and its ranking among the surface crystallographic methods is comparable to x-ray diffraction for determining the structure of bulk materials. Various kinds of complexity are considered, starting with the atomic geometries of semiconductor surfaces which are heavily reconstructed exhibiting far-reaching relaxations down to deeper layers. A next class of systems are coadsorbate phases on metal surfaces whose complexity comes from the presence of various species. In this section also the structure of larger molecules on metal surfaces is discussed. In the last two chapters we concentrate on surfaces violating the two-dimensional translational symmetry. The simplest systems are incommensurate overlayers on metal surfaces. Each layer possesses translational symmetry, but the compound system breaks it. In a next step we also disregard the translational symmetry of each layer and focus on the structure of quasicrystal surfaces.

* Correspondence author (e-mail: over@fhi-berlin.mpg.de)

I. Introduction

The low-energy electron diffraction (LEED) method was developed by a concerted endeavor of theoreticians and experimentalists in the late 1960s. This is nicely reflected in the author list of LEED publications at those days containing names frequently encountered. Examples are (Jespen, Marcus, Jona), (Pendry, Anderson), (Tong, Rhodin), (Forstmann, Berndt) and others. The names of Paul Marcus & Franco Jona are still frequently found in the current literature. Franco Jona took the first reliable LEED IV data of the Al(100), Al(110) and Al(111) surfaces [1] which were the best data at that time, and many theoretical groups used these data as a test-bench for their theoretical approaches of the multiple scattering problem in LEED. Franco Jona wanted to give a talk on this subject at the Physical Electronics Conference of 1969 in order to generate discussion on the then unknown procedure for collecting IV data. It is remarkable and also characteristic for the acceptance of LEED within the surface science community in those days that this paper was turned down as not interesting and not appropriate for a surface science conference [2]. A brief account of the history of LEED can be found in Refs. [3–7]. The present review article will be dedicated to Franco Jona's 75th birthday and the impact he had on LEED and on our own research work.

Nowadays, the LEED method has reached a maturity which renders this method a standard technique in surface crystallography. This is demonstrated by the fact that about 50% of the newly determined surface structures are solved by LEED. Therefore, LEED has to be considered as the prime crystallographic technique in surface science, and its ranking among the surface crystallographic methods is comparable to that of x-ray diffraction for the structure determination of bulk materials. Yet, to put LEED on the same level with bulk-x-ray diffraction is probably exaggerated since in x-ray diffraction a number of methods are available allowing to arrive at an approximate guess of the structure more or less directly from the experimental data, such as Patterson function and Fourier synthesis. In bulk-x-ray diffraction, there are also direct methods which allow a structure determination directly from the intensities as long as the structures are of limited complexity. So far, no equivalent method has been developed in the case of LEED, where a good initial guess of the structure is equally required.

In this article we report on the atomic geometry of complex surface structures which were determined by using low-energy electron diffraction (LEED) and whose particular selection is closely related to our own research activities. The complexity of surface structures enters the structure determination in various ways. If the two-dimensional unit cells are large, many plane waves are required in the multiple scattering calculations in order to properly expand the outgoing LEED field. Large unit cells can also accommodate many atoms making a structure determination quite elaborate. This kind of complexity is encountered, e.g., in the adsorption of big molecules on metal surfaces (section 3.8). Another facet of complexity emerges when the substrate is heavily reconstructed, making the overlayer periodicity run over several layers. In this case, many atomic coordinates have to be considered simultaneously in the structure refinement. Prominent examples of this kind of complex surface structures are semiconductor surfaces which are frequently strongly reconstructed, exhibiting far-reaching relaxations down to deeper layers (chapter 2). Another example of complex surface structures are surfaces with unit cells accommodating several different species, such as coadsorbate phases on metal surfaces (chapter 3). The loss of symmetry according to the 17 possible two-dimensional space groups is always a problem in that the computing time for LEED intensity calculations depends critically on the actual symmetry. But an even more dramatic reduction of symmetry is encountered when the two-dimensional periodicity is violated. The simplest examples are incommensurate overlayers on metal surfaces. Each layer still possesses translational symmetry, but the compound system breaks the translational symmetry (chapter 4). The situation becomes more involved when we also throw overboard the translational symmetry of each layer and focus on the surface structure of quasi-crystals (chapter 5). We will end this article with a conclusion and an outlook (chapter 6).

II. Semiconductor surfaces

2.1 Introduction

Many elemental and III-V compound semiconductors crystallize into diamond and zinc blende structure, respectively, which emphasizes the importance of sp^3 hybridization for the bond formation. Hence, bulk-terminated semiconductor surfaces are inevitably unstable because of the large number of unpaired sp^3-type dangling bonds on them which raises the surface energy prohibitively high. The dangling bonds are formed with a bulk-truncated surface due to missing binding partners (cf. Fig. 1a). On the clean semiconductor surfaces, surface atoms rearrange in position and form new bonds in order to reduce the number of unpaired bonds. The most prominent reconstruction is certainly the (7×7) structure of Si(111) (cf. Fig. 1b). The new bonds often introduce elastic stress into the surface region. The balance between electronic and stress energies gives rise to an array of superlattices found on reconstructed semiconductor surfaces of different materials, e.g., (2×1), (2×2), $(\sqrt{3} \times \sqrt{3})\,R30°$, (7×7), $c(2 \times 8)$, etc. Irrespective of the manifold superlattices, there are only a few distinct structural motifs (building blocks), such as dimers, trimers, and adatoms, setting up the superstructure. The reader can find a detailed discussion of a number of reconstructed structures and the reasons why they are formed on clean Si(111), Ge(111), GaAs(110) and GaAs(111) surfaces in [8–10]. It is interesting to note that these dangling bonds dictate the surface activity of semiconductor surfaces, such as of silicon surfaces [11]. When foreign atoms and molecules are present at the surface, they are simply used to pair up the dangling bonds. For instance, if all dangling bonds are capped by atomic hydrogen chemisorption, the semiconductor surface is passivated, i.e., its ability to react with other molecules becomes negligible.

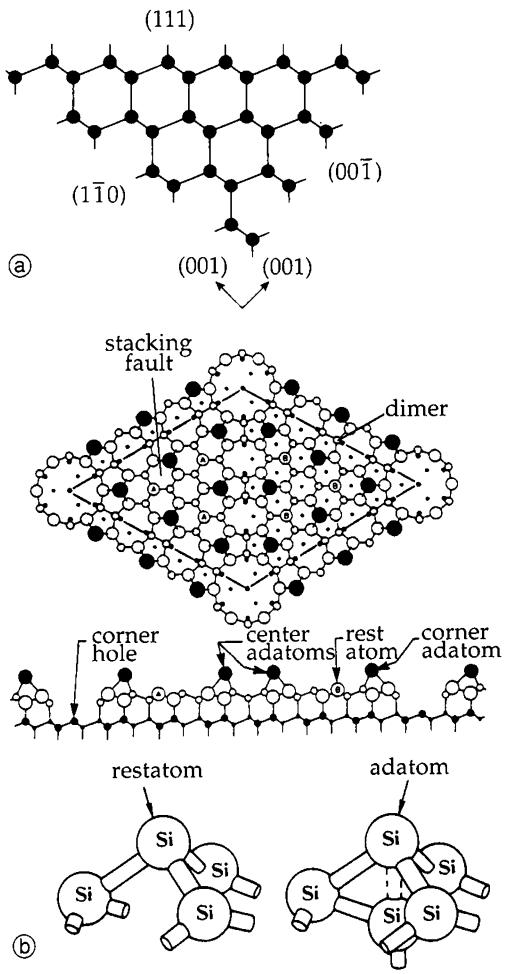

Fig. 1. **a**) The formation of dangling bonds on the unreconstructed surfaces of the three low index planes of Si and Ge. Si (Ge) atoms in the bulk are tetrahedrally coordinated. **b**) The DAS model for the Si(111)–7 × 7 structure, indicating the various structural elements which stabilizes this reconstruction, i.e. Dimer, Adatoms, and Stacking fault.

2.2 The (2 × 1) reconstruction of the (001) surfaces of Si and Ge

Each surface atom of the bulk-terminated (001) surface of Si (and also Ge) carries two dangling bonds, resulting in an unacceptably high surface energy. The surface energy is lowered by reducing the number of dangling bonds via rebonding. From the observation of a (2 × 1) LEED pattern Schlier and Farnsworth (40 years ago!) [12] concluded that the main structural element of the Si(001)–(2 × 1) surface is formed by Si dimerization along the [110] direction which reduces the density of dangling bonds by 50%. Later this structural feature has been identified by theory and experiment [13].

Complete crystallographic data of the clean Si(001)-(2 × 1) surface were provided by a recent LEED analysis [14] and summarized in Fig. 2. The main structural features are the following: The topmost Si atoms are asymmetrically displaced along the [110] direction by 1.0 Å and 0.7 Å, respectively, so as to form the Si dimers. The dimer bond length is 2.25 ± 0.08 Å which is slightly smaller than the bond length found in Si bulk (2.35 Å). The Si dimer bond length found with LEED agrees well with values derived by ab-initio calculations such as

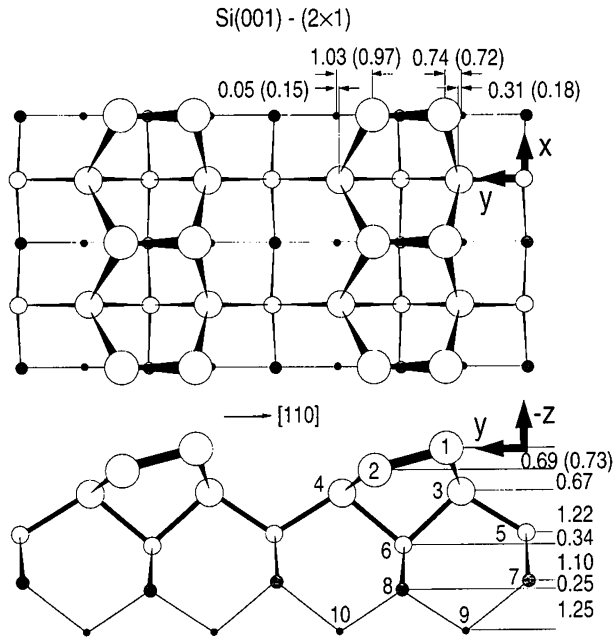

Fig. 2. Structure model and the main structural characteristics of the Si(001)–2 × 1 surface derived from a LEED analysis. All parameters are given in Å [14].

2.23 Å [15] and 2.25 Å [16]. The dimerization of the topmost Si layer induces strong local strain fields in the surface region, resulting in displacements of Si atoms in even deeper layers. In particular, Si atoms in the second layer are shifted laterally by about 0.2 Å, while vertical displacements of these Si atoms were not found. As a result of the pairing in the second Si layer, a pronounced buckling is observed with third layer Si atoms which amounts to 0.34 ± 0.05 Å. This buckling in turn leads to a rumpling of the fourth layer by 0.25 ± 0.07 Å. On symmetry grounds, a substantial buckling in the fifth Si layer is excluded, and due to the limited elastic mean free path of the electrons, the LEED analysis was not sensitive to distortions in even deeper Si layers. Another important detail of the Si(001)–(2 × 1) surface structure represents the tilting of the Si dimers. The vertical separation between the up and down atoms in the dimers is 0.73 ± 0.05 Å which, together with its lateral asymmetry, provides bond lengths between the dimer atoms and the second layer Si atoms directly underneath, comparable with the bulk values.

It is instructive to correlate this geometric structure with the electronic structure of the Si(001)–(2 × 1) surface. The unreconstructed (001) surface of Si has two dangling orbitals per surface atoms, each of them being filled with one electron. It is well established that the energy of this surface is lowered by about 1 eV when adjacent surface atoms form a new surface bond from dangling bonds, the so-called dimers, so that only one bond per surface atom remains unsaturated [17]. This would explain the appearance of symmetric Si dimers. The clean Si(001)–(2 × 1) surface, however, exhibits buckled dimers because the half filled bands of dangling bonds of a symmetric dimer rearrange themselves into one (more) filled orbital (this Si atom moves outwards) and one (more) empty orbital (the corresponding Si atom moves inwards) [17]. The energy difference between symmetric and asym-

metric Si dimers is about 0.1 eV, while the two possible asymmetric dimer configurations are practically degenerated [15]. In the molecular orbital language, the down atom adopts a planar quasi sp^2 configuration, while the up atom in the dimer adopts a p^3 configuration. This kind of symmetry lowering is frequently observed in solid state physics, and it is referred to as Peierls distortions or Jahn-Teller effect. The crucial point is the existence of half filled bands in the symmetric configuration. In addition, the dangling bonds within a buckled dimer are not independent but rather they interact and combine to form a weak π bond which turns out to be of paramount importance for the hydrogen adsorption on this surface (cf. the discussion below). A first strong hint for the presence of buckled dimers on the clean Si(001)–(2 × 1) surfaces goes back to photoelectron emission studies [18] and STM spectroscopy [19] which both demonstrated that the Si(001)–(2 × 1) surface is non-metallic. With symmetric dimers the Si(001) surface should become metallic because the band associated with the dangling bonds is half filled. Recent high-resolution photoelectron emission data revealed even two inequivalent types of surface silicon atoms which were assigned to be the up and down atoms of buckled dimers [18]. In early total-energy calculations [16, 20] the dimers were found to be asymmetric as well as buckled producing a surface with semiconducting properties compatible with the above-mentioned experiments.

From the preceding discussion both a rapid flipping between the buckled dimer configurations or a statistical (static) distribution of these buckled dimers would be equally conceivable. Upon cooling below 200 K the (2 × 1) structure transforms reversibly into a c(2 × 4) structure [21]. In the c(2 × 4) neighboring dimers are statically tilted in the opposite direction, reducing the total energy per surface atom by a small amount on the order of 10 meV [22]. Upon raising the temperature, the tilted Si dimers start to flip from one asymmetric dimer configuration to the other. This view received direct support by recent low-temperature STM investigations [23] that imaged this phase transition. At room temperature, a large portion of the surface was covered with apparently symmetric dimers, while upon cooling to low temperatures (120 K), an increase of dimers in the asymmetric configuration was observed. Hence, the STM images at room temperature, showing predominantly symmetric dimer configurations, were argued to be a consequence of time averaging. The Si(001)–(2 × 1) surface is then simply characterized by Si dimers which are rapidly switching between the orientations in the up and down direction.

A recent surface x-ray diffraction (SXRD) analysis [24] indicated that also the clean Ge(001)–(2 × 1) surface constitutes surface dimers which are inclined out of the surface at an angle of about 17°; the separation between up and down atoms turned out to be 0.7 Å. A detailed comparison of the structural parameters discloses the atomic geometries of the (2 × 1) reconstructions on Ge(001) and Si(001) to be very much alike, in particular when the different lattice constants are taken into account. In the following, we will see that this (general) property of Ge and Si is frequently encountered.

Adsorption of hydrogen on the (001) surface of Si (Ge) changes the (2 × 1) reconstruction of the clean surface, and it is generally believed to lift the Jahn-Teller distortion, resulting in a symmetric dimer configuration with presumably two H atoms per dimer ('monohydride': $\theta = 1.0$) [25]. Further uptake of hydrogen requires bond breaking of the dimers which is characterized by a transformation of the (2 × 1) structure into a defective (1 × 1) 'dihydride' surface ($\theta = 2.0$) [26]. The following discussion focuses on the crystallographic data of the deuterized Ge(001) surface. Deuterium D = ^{2}H was used since LEED is more sensitive to the position of D than to that of H because of the smaller thermal movements owing to its larger mass, while H and D have identical chemical properties. A LEED structure analysis of Ge(001)–(2 × 1)–D [27] indicated that upon D adsorption the dimer bond length of 2.4 ± 0.2 Å remains unchanged, compared to the clean surface. Both Ge dimer atoms are capped by D chemisorption. The D-covered Ge dimers are symmetric so that the main effect of D adsorption on the Ge(001)–(2 × 1) surface consists in a back bending of the Ge dimers from 17° tilting to 0°. The D atoms sit on top of the Ge atoms (Ge–D bond length: 1.6 ± 0.2 Å), thus saturating the remaining dangling bonds. The detailed atomic geometry is summarized in Fig. 3. The dimer-induced distortions in deeper substrate layers turn out to be quite similar in both the clean [24] and the D-covered (2 × 1) structures in line with the view that the lateral shifting of the topmost Ge atoms forming the dimers is chiefly responsible for these distortions.

The pairing of D atoms is controlled by the attractive interaction between unpaired dangling bonds of the dimer atoms (so-called π bonding) rather than by a direct attraction between the D atoms [28, 29]. Since the adsorption of single D atoms on a dimer destroys the attractive π interaction between dangling bonds within a Ge dimer,

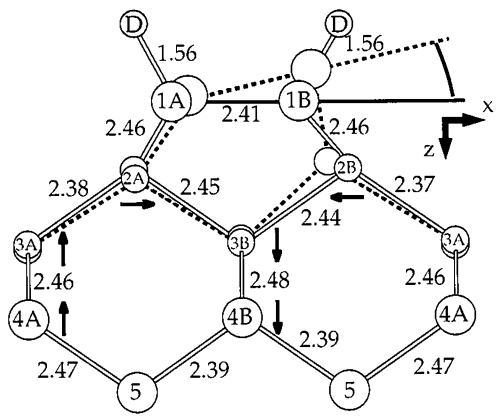

Δx(1A) = +0.80(8)	$d_\perp$(D–Ge) = 1.35(20)
Δx(1B) = -0.80(8)	$<d_{12}>$ = 1.18(5)
Δx(2A) = -0.05(10)	$<d_{23}>$ = 1.34(5)
Δx(2B) = +0.05(10)	$<d_{34}>$ = 1.45(5)
Δz(3) = 0.12(5)	$<d_{45}>$ = 1.38(8)
Δz(4) = 0.14(5)	d_{56} = 1.44(8)

Fig. 3. Structure model and fit parameters for the Ge(001)–(2 × 1)–D surface [27] as obtained from a LEED-IV analysis. The dashed lines indicate the structure of the clean Ge(001) surface (taken from Ref. [24a]). The values indicated are the bond lengths in Å between touching Ge atoms.

adsorption for a second D atom on the same dimer is energetically more favorable than occupying another dimer and thereby destroying a further π bonding, even though the direct interaction between neighboring D atoms might be repulsive.

2.3 Metal-induced $(\sqrt{3} \times \sqrt{3})$ R30° reconstructions on the (111) surface of Si and Ge

The bulk-terminated (111) surfaces of Ge and Si possess one dangling bond per surface atom whose density is high enough to let both surfaces reconstruct in a quite complex manner. The thermodynamically stable Si(111) surface is the (7 × 7) reconstruction, while the Ge(111) surface reconstructs into a c(2 × 8) superstructure. The stabilization of the (111) surfaces of elemental semiconductors is well understood and is mainly driven by the reduction of the number of dangling bonds at the surface, without introducing too much strain in the surface region. Mainly two structural elements meeting this principle have been identified so far. Most notably, the so-called adatoms are able to saturate three dangling bonds on (111) surfaces, while creating only one new dangling bond. This structural motif is known to stabilize the clean Ge(111)–c(2 × 8) surface [30] and is also a major stabilizing factor of the dimer-adatom-stacking-fault (DAS) model of the clean Si(111)–(7 × 7) surface [31]. The second structural element that efficiently reduces the number of dangling bonds was originally found on (001) surfaces whose bulk-truncated structure consists of atoms carrying two unsaturated bonds (cf. section 1.2). In pairing up two adjacent atoms, i.e., forming so-called dimers, the number of dangling bonds can be halved. On the Si(111)–(7 × 7) surface (cf. Fig. 1b), one half of the (7 × 7) unit cell contains a stacking fault between the top two Si double layers, while the other half shows the normal stacking sequence. These two (triangular-shaped) regions are interconnected by Si dimers which reduce efficiently the number of dangling bonds. It is important to mention that the difference in the surface geometries of the clean Si(111) and Ge(111) surfaces is quite singular in that normally the surface structures of Si and Ge – in particular adsorbate-induced reconstructions – agree well with one another [32].

Adsorption of noble metals Au and Ag and also of alkali metals, Li and Na, on the (111) surfaces of Ge and Si leads to structures with $(\sqrt{3} \times \sqrt{3})$ R30° periodicity. Although the surface unit cell is rather small, the structure determination took more than 15 years of intense research work [33], employing a host of surface sensitive techniques. Eventually two models have emerged for the case of Si(111) which are consistent with most of the experimental results, namely the so-called honeycomb-chained trimer (HCT) model (cf. Fig. 4) describing the Ag/Si(111)–$(\sqrt{3} \times \sqrt{3})$ R30° surface [34] and the conjugate HCT model (CHCT) (cf. Fig. 5) found with Au/Si(111)–$(\sqrt{3} \times \sqrt{3})$ R30° [35, 36]. Both models are characterized by a missing top-Si layer that is replaced by noble metal atoms. While Ag adsorption forces the remaining Si atoms in the top layer to create Si trimers centered above fourth-layer Si atoms, Au leaves these Si atoms almost at the bulk positions and forms Au trimers instead.

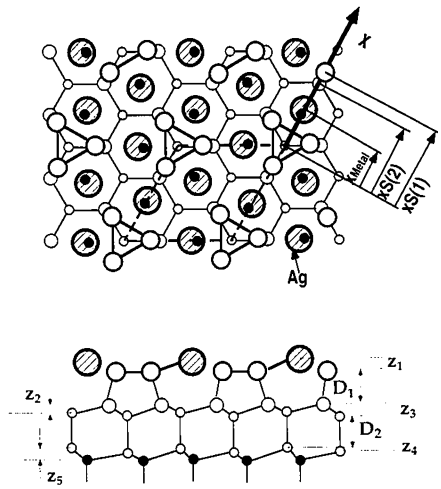

Fig. 4. Schematic top and side view of Ag-induced reconstructions on the Si(111) and the Ge(111) surface. The main building block of the honeycomb-chained trimer (HCT) model is the Si(Ge) trimer. The biggest circles denote Ag atoms.

In the HCT configuration for Si(111)–Ag the Si trimerization pairs up two dangling bonds on each Si atom. The remaining Si electron is paired with the s valence electron of the Ag atom creating a non-metallic surface. The bonding picture for the case of Au–Si(111) is more complex. While the Si atoms are no longer nearest neighbors in the plane, they nevertheless form bonds through the Au trimers, resulting in six-atom clusters of three Si atoms and three Au atoms each (shadowed region in Fig. 5). The CHCT reconstructed surface is metallic.

The reason for the HCT and the CHCT formation on Si(111) was attributed to the relative strengths of the metal-metal and Si-Si bonds. The Au-Au bond with 2.29 eV is stronger than the Ag-Ag bond with 1.69 eV [33, 37, 38], and the Si-Si bond energy is 3.39 eV. For the Si(111)–$(\sqrt{3} \times \sqrt{3})$ R30°–Au surface, the Au trimer bond formation is obviously more important for total energy balance than the formation of Si trimers. By contrast, the energy gain due to metal trimerization is smaller for

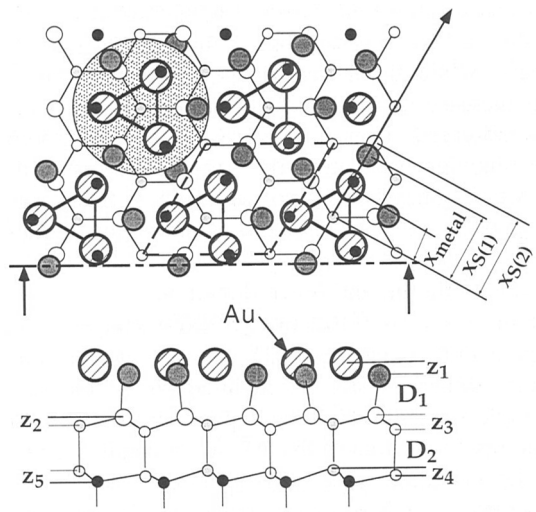

Fig. 5. The conjugate honeycomb-chained trimer (CHCT) model of the Au-induced reconstruction on the Si(111) and Ge(111) surface. The main building block represents the Au trimer. The largest circles denote Au atoms, and Si(Ge) atoms in layers 2, 3, and 4 are depicted with decreasing radii. The solid circles denote sixth-layer atoms.

Ag and therefore the formation of Si trimers wins out. From this simple argument, the structure of Si(111)–$(\sqrt{3} \times \sqrt{3})$ R30°–Li can be predicted. Since the Li–Li bonding (1.14 eV) is even weaker than that of Ag, one monolayer of Li should induce a HCT reconstruction.

Solely based on the chemical similarities between Ge and Si and the fact that the relative strength of the metal-metal bond and the semiconductor-semiconductor bond do not reverse the order in going from the Si to the Ge system (the Ge–Ge bond strength is 2.84 eV), one expects to find similar bond configurations also with Ge(111). A previous SXRD study has identified the CHCT model for the Ge(111)–$(\sqrt{3} \times \sqrt{3})$ R30°–Au surface [39]. For the Ge(111)–$(\sqrt{3} \times \sqrt{3})$ R30°–Ag surface, however, a SXRD investigation favored the CHCT model [40] in contrast to the case of Si(111). Recent LEED analyses have clarified this issue, showing that the Ge(111) and Si(111) surfaces do react identically to the chemisorption of Au and Ag [41, 42]. It turned out that Ag forms the HCT model on both Si(111) and Ge(111), while Au forms the CHCT model on both substrates. In Table 1 the characteristic bond lengths and in Table 2 the atomic coordinates are compiled. As expected, the metal-metal bond lengths are identical for the cases of Si(111) and Ge(111). The bond length between the trimer substrate atoms increases when going from Si(111) to Ge(111) which parallels the respective lattice constants. It is quite interesting that the metal-Si(Ge) bond length depends only on the size of the substrate atom.

From the above considerations of bond strengths we have already conjectured that Li (and Na) adsorption will also lead to the HCT formation on Si(111) and Ge(111). Quantitative LEED has indeed shown that 1 ML of Li atoms forms the HCT structure on Si(111) [43]. From the striking similarities of experimental LEED-IV curves of Ge(111)–$(\sqrt{3} \times \sqrt{3})$ R30°–Ag and Ge(111)–$(\sqrt{3} \times \sqrt{3})$ R30°–Li [44], there is also strong evidence that Li adsorption drives the Ge(111) surface (as with Si(111)) into a HCT configuration. This was recently confirmed by a full-dynamical LEED analysis [45].

Table 1. Comparison of the $(\sqrt{3} \times \sqrt{3})$ R30° reconstruction formed by Ag and Au on Si(111) or Ge(111). The crystallographic data were obtained by using quantitative LEED. Main result: the surface structures found by the adsorption of Ag and Au are almost identical on Si(111) and Ge(111).

System: $(\sqrt{3} \times \sqrt{3})$R30°	metal-metal n–n distance	bond lengths: substrate trimer	model	metal-Si(Ge) bond length
Ag/Si [45]	3.47 ± 0.12 Å	2.49 ± 0.08 Å	HCT	2.36 ± 0.16 Å
Au/Si [35]	2.80 Å	–	CHCT	2.42 Å
Ag/Ge [38]	3.58 ± 0.06 Å	2.72 ± 0.08 Å	HCT	2.52 ± 0.14 Å
Au/Ge [39]	2.81 ± 0.07 Å	–	CHCT	2.50 ± 0.14 Å

Table 2. Atomic coordinates in Å for the Ag-induced HCT reconstruction of Ge(111) in comparison to the Si(111) case. The same comparison was carried out with the Au-induced CHCT reconstruction on Ge(111) and Si(111). Note that the parameters for the HCT model on Ge(111) and Si(111) are almost identical if the different lattice constant is considered (Si: 5.43 Å, Ge: 5.66 Å). The same conclusion is valid for the Au-induced CHCT reconstruction. Structural parameters of the bulk indicate that this parameter was not optimized in that LEED analysis.

	Ag/Ge(111) [38]	Ag/Si(111) [45]	Au/Ge(111) [39]	Au/Si(111) [35]
X_{Metal}	2.93 ± 0.06	2.85 ± 0.12	1.62 ± 0.07	1.62
$X_{S(1)}$	5.35 ± 0.06	5.21 ± 0.08	4.07 ± 0.07	3.98
$X_{S(2)}$	4.78 ± 0.01	4.47 ± 0.09	4.58 ± 0.09	–
Z_1	0.70 ± 0.04	0.78 ± 0.05	0.51 ± 0.05	0.56
D_1	2.43 ± 0.03	2.30 ± 0.04	2.44 ± 0.03	bulk
Z_2	0.73 ± 0.03	0.66 ± 0.07	0.68 ± 0.12	bulk
Z_3	1.06 ± 0.05	1.03 ± 0.07	0.92 ± 0.07	bulk
D_2	2.20 ± 0.03	2.05 ± 0.04	2.23 ± 0.03	bulk
Z_4	0.19 ± 0.05	0.19 ± 0.05	0.22 ± 0.05	bulk
Z_5	0.86 ± 0.05	0.85 ± 0.07	0.96 ± 0.07	bulk

2.4 Metal-induced (3 × 1) reconstructions on the (111) surface of Si and Ge

The deposition of monovalent metal atoms, such as Ag and also of the alkali metals Li, Na, K, on the (111) surfaces of Ge and Si, leads not only to the formation of a HCT reconstruction with $(\sqrt{3} \times \sqrt{3})$ R30° symmetry at a metal coverage of 1 ML, but is also able to produce surface structures with (3 × 1) periodicity at a metal coverage of $^1/_3$ ML. This reconstruction has received considerable experimental attention over the past 10 years. Recently, it was found that this reconstruction exhibits unusual chemical [46] and electronic properties [47] in that the Si(111)–(3 × 1)–Na surface is less reactive against oxidation and its surface-state band gap is extraordinarily large (about 1 eV). Although the surface unit cell is again quite small, the atomic geometry has not been determined so far. Also for this surface reconstruction many models have been proposed in the literature over the past 10 years, and most of them have been discarded after the metal coverage was pinned down to be $^1/_3$ [48]. Essentially, two promising candidates are left in the literature which have been discussed in the context of STM images and tunneling spectroscopy [49], electronic properties (UPS, ARUPS) [50], and ab-initio calculations [51]. These are the Seiwatz model [48] and the extended Pandey model [51] (cf. Fig. 6). The Seiwatz model is characterized by fivefold rings of Si(Ge) atoms which form a kind of π-bonded chains as also found for the Si(111)–2 × 1 surface [52].

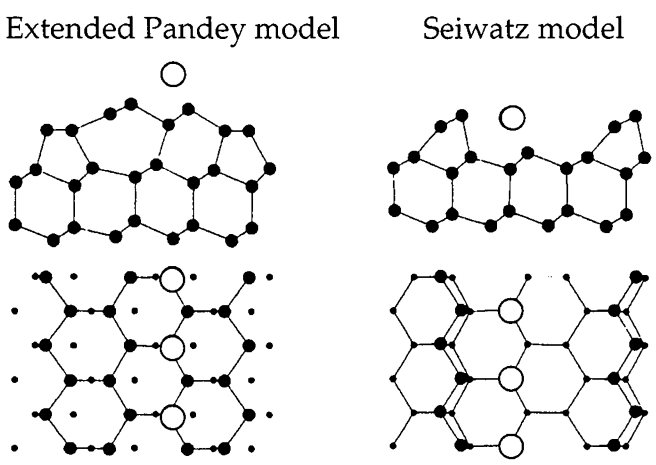

Fig. 6. Side and top view of the idealized geometries of the (a) Seiwatz and the (b) extended Pandey model.

The extended Pandey model consists of a sevenfold ring carrying the π-bonded chain in combination with a five and a six-members ring of Si. An intuitive notation is therefore 567567 model and 500500 model for the extended Pandey and the Seiwatz model, respectively (cf. Fig. 6). It is important to note that none of these models has ever been confirmed by a surface crystallographic technique such as LEED or surface x-ray diffraction (SXRD). In this sense, the atomic geometry of the (3 × 1) surface reconstruction of Si(111) has to be considered as unknown.

In this section, we report that even these two models can be turned down on the basis of recent x-ray and electron diffraction data. Rather a different structure model has been developed that fits SXRD data and LEED data as well. Before elaborating on this novel structure model for the (3 × 1) reconstructions of Si(111) and Ge(111), we recall a previous LEED observation which is very helpful for rejecting proposed structure models. Fan and Ignatiev [53] have shown that the LEED-IV curves of the Si(111)–(3 × 1)-metal system and the LEED-IV curves of the Ge(111)–(3 × 1)-metal system are almost independent of the kind of adsorbed metal atom. Therefore the LEED data are not determined by the metal atoms themselves but rather by the metal-induced surface reconstruction of the Ge(111) and Si(111) surface which should be identical for all metals used [54]. Referring back to section 1.3, where we found close resemblance between the $(\sqrt{3} \times \sqrt{3})$ R30° reconstruction of Ge(111) and Si(111), one may anticipate that the surface reconstructions of Ge(111)–3 × 1 and Si(111)–3 × 1 are also similar. If we can determine the surface structure for one surface, say Si(111)–(3 × 1), then the corresponding Ge(111)–(3 × 1) reconstruction can be found by just scaling the Si coordinates to Ge. This is a very important and helpful feature since it allows us to circumvent the problem with multiple local minima in the r-factor surfaces, i.e., different surface structures exhibiting similar good agreement between calculated and experimental diffraction data: It is very unlikely that Ge(111)–(3 × 1) and Si(111)–(3 × 1) produce coincident local minima in the r-factor surface due to different lattice constants and scattering properties. Restricting the analysis to the case of Li, we can safely neglect scattering from the metal overlayer focusing only on the substrate reconstruction. If the experimental LEED/SXRD data of both Ge(111)–(3 × 1)–Li and Si(111)–(3 × 1)–Li can be fitted with the same model structure of surface reconstruction, this strongly supports the assumption of having now found the true surface structure.

The new structure model proposed here goes back to a recent SXRD study of the Si(111)–(3 × 1)–Li surface [55] which favored a model, denoted as 560560 model: the substrate reconstruction consists of consecutive five member and six member rings, separated by empty channels (cf. Fig. 7). This model can be viewed as being a compromise between the Seiwatz and the extended Pandey model: Either one adds a six fold ring to the Seiwatz model or one removes the sevenfold ring from the extended Pandey model to arrive at the 560560 model. The model structure favored by SXRD was strongly puckered in that the six fold ring is by about 1 Å higher than the fivefold

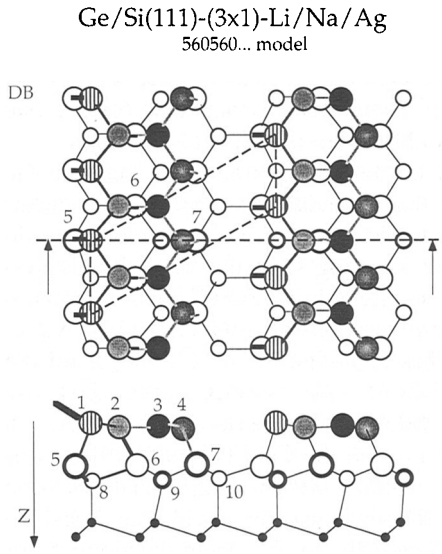

Fig. 7. The top and side view of the 560560 ... model which is favored by SXRD and LEED to be the actual surface reconstruction of the Li–(3 × 1) of Si(111) and Ge(111). The atomic coordinates in angstroms of atom N (N = 1, 2, ... 10) can be found in Table 3.

Table 3. Atomic coordinates in Å for the 560560 reconstruction of Si(111)–(3 × 1)–Li without considering the Li atoms. Presumably, Li binds to the dangling bond associated with atom 1 in Fig. 7. In columns (a) to (c) the history of the combined SXRD/LEED is summarized starting with the model originally proposed by SXRD.

Atom	(a) 1st SXRD [55] (x, z)/Å	(b) 2nd LEED [57, 58] (x, z)/Å	(c) 3rd SXRD [58] (x, z)/Å
1	(1.90, 1.00)	(0.88, 0.00)	(0.86, 0.00)
2	(2.60, 0.46)	(2.38, 0.26)	(2.33, 0.35)
3	(5.04, 0.00)	(4.42, 0.17)	(4.62, 0.23)
4	(6.00, 0.54)	(5.78, 0.32)	(5.78, 0.35)
5	(0.05, 2.94)	(0.09, 2.45)	(0.13, 2.35)
6	(3.03, 2.88)	(3.28, 2.41)	(3.29, 2.35)
7	(6.49, 2.78)	(6.51, 2.39)	(6.51, 2.44)
8	(0.96, 3.82)	(0.86, 3.25)	(1.22, 3.26)
9	(4.30, 3.69)	(4.61, 3.17)	(4.28, 3.26)
10	(7.62, 3.56)	(7.66, 3.12)	(7.83, 3.01)

ring (cf. Table 3, left). The succession of the surface structure determination is summarized in Table 3. Using the SXRD structure model as an input for a full-dynamical analysis of the Si(111)–(3 × 1)–Li LEED data only results in a very bad fit (best Pendry r-factors reached are between 0.7 and 0.8). Hence, it seemed that the structure model proposed by SXRD is not the ultimate solution. In a next step, an exhaustive structural search based on the 560560 model was performed. Using a newly developed method in LEED (the so-called envelope method [56]), we could find an acceptable agreement between theory and experiment on the basis of the 560560 model as quantified by an r-factor of 0.36 (cf. Table 3, middle). This model structure is characterized by a topmost layer which is almost flat, i.e. the fivefold and the six fold rings have the same height. With a very similar model the LEED data of the Ge(111)–(3 × 1)–Li surface could be fitted as well, lending additional support that we now found the true surface structure of the Si(111)–(3 × 1)–Li surface.

In order to resolve the discrepancy between LEED and SXRD, the structural parameters found by LEED were re-

piped as a trial model into a SXRD analysis. The structure refinement by SXRD results in an equally good agreement with the experimental data as for the original 560560 model (Table 3, left). The structural parameters agree within the error bars with those determined by LEED (cf. Table 3, middle and right).

From the structure analysis of the Li-induced (3 × 1) reconstruction of Ge(111) and Si(111) it can be concluded that neither SXRD nor LEED alone may be able to solve such complex surface structures. Only the combined effort of SXRD and LEED succeeded eventually in solving the (3 × 1) reconstruction of the (111) surfaces of Si and Ge.

The structural characteristics of the Si(111)–(3 × 1)–Li surface can be described as follows: The substrate reconstruction consists of consecutive five-member and six-member rings which are separated by empty channels. The atoms labeled 3 in Fig. 7 exhibit an almost planar bond configuration within 0.15 Å which indicates rehybridization from sp^3 (bulk-like) to sp^2. Hence, the dangling bond of atom 3 is empty. Atom 4 adopts a p^3 bonding configuration with a fully occupied dangling bond. The bond lengths from atom 3 to 2 and from 3 to 4 are about 8% shorter than the bulk bond length. The bond angles of the coordination shell of atom 3 are around 120° which is consistent with a sp^2 rehybridization. The bond lengths for atom 4 with its nearest neighbors are slightly longer than the bulk bond length. Altogether, there appears to flow electronic charge from atom 3 to atom 4, thereby reducing the number of dangling bonds by 2 per (3 × 1) unit cell. This view is supported by recent DFT calculations [58]. The only dangling bond left on the surface is located on atom 1. The role of the alkali metal is that of a donor which passivates the dangling bond, so that no unsaturated bonds remain.

This structure model is convincing in many respects since it easily allows to explain other experimental findings. For instance, the charge transfer from atom 3 to atom 4 transforms the otherwise metallic surface into a semiconducting one [47]. The observed double stripes in fill-state STM images and single stripes in empty state STM images can be reconciled by assigning the rows of empty state to atom 3 and assigning the rows of the filled states to atoms 1 and 4 [49]. Recent DFT calculations have confirmed this view [58]. Also the transformation from the (3 × 1) structure to the $(\sqrt{3} \times \sqrt{3})$ R30° phase by depositing more metal on the surface can easily be rationalized. Beyond a coverage of 1/3, the bonding configuration of atom 3 becomes destabilized via additional electronic charge density. Thereby atom 3 is replaced by a metal atom, and the neighboring substrate atoms trimerize, for instance atom 4 and 2, to form the $(\sqrt{3} \times \sqrt{3})$ R30° phase. Last, also the energetics of the 560560 surface is expected to be quite favorable since the total energy of the Seiwatz and the extended Pandey model are almost degenerated and the 560560 model represents a compromise between these structure models. A recent DFT study by Seitsonen [58] found that the 560560 model is by 0.4 eV more favorable than the 500500 and 567567 model.

2.5 The (2 × 2) reconstructions of clean GaAs(111) and GaAs($\bar{1}\bar{1}\bar{1}$)

Different from elemental semiconductors, compound III-V semiconductors, such as GaAs, minimize their surface energies (i.e., the number of dangling bonds) by filling the group V dangling bonds and emptying group III dangling bonds. This results in a type of ionic bonding. Generally, the composition of the surface is governed by the requirement of a charge-neutral surface region. This criterion leads to the so-called electron counting rule [59] which determines the allowed stoichiometries for the surface compounds. Depending on the preparation conditions, the close-packed polar faces of GaAs form, among other superstructures, two surface structures with (2 × 2) symmetry. One is prepared under As-rich conditions, and the resulting reconstruction is referred to as GaAs($\bar{1}\bar{1}\bar{1}$)–(2 × 2). On the basis of STM images [60], the main structural element of this surface was proposed to be the As trimer which was also favored from first principle calculations [61, 62]. The other (2 × 2) surface is prepared under Ga-rich conditions, and the (111) surface of GaAs reconstructs into a so-called Ga vacancy model [63]. This kind of structure has also been observed for other III–V semiconductors, such as GaP, GaSb and InSb [10].

Let us start the discussion with the Ga vacancy model which was determined previously by LEED [63] and whose structural parameters are summarized in Fig. 8. The Ga vacancy generates three additional As dangling bonds which exactly compensate the remaining three Ga dangling bonds. In other words, the removal of one Ga atom causes the surface to be stoichiometric. This effect is called autocompensation which turns the former polar surface into a non-polar one. The charge transfer is also obvious from the structural results (cf. Fig. 9). Every Ga

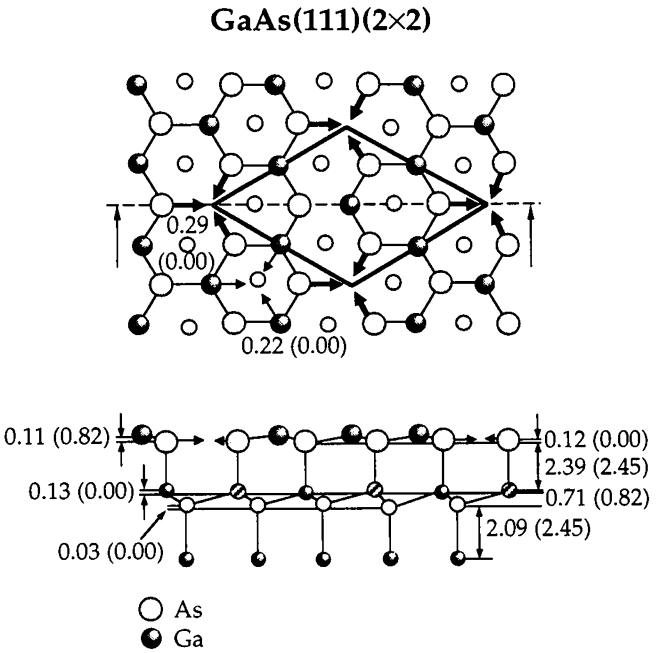

Fig. 8. The top and side view of the (2 × 2) Ga vacancy structure on the GaAs(111) surface. The main structural characteristics consists of a missing Ga atom and an almost flat Ga + As double layer [44]. The numbers in brackets are corresponding bulk values.

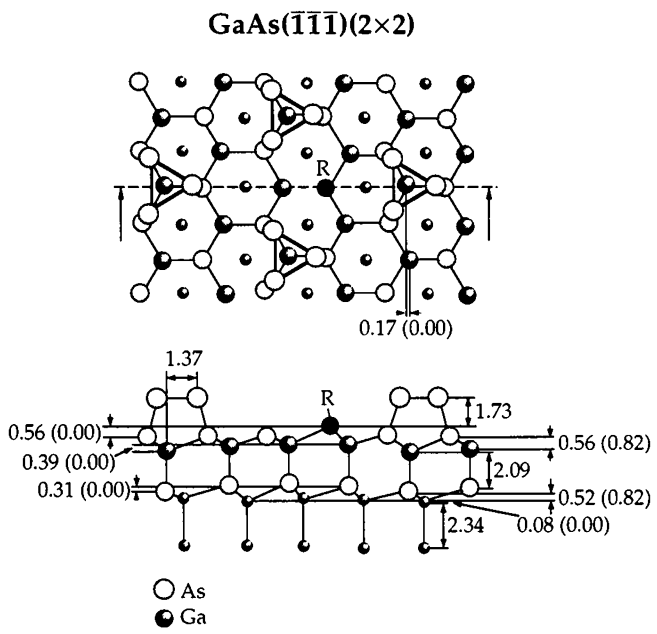

Fig. 9. The top and side view of the (2 × 2) As trimer structure on the GaAs($\bar{1}\bar{1}\bar{1}$) surface as derived from LEED intensity data [44]. The numbers in brackets are corresponding bulk values.

atom carrying a dangling bond is bonded to an As atom which also possesses a dangling bond. To practice the so-called electron counting rule we rationalize this charge transfer in more detail. In the GaAs bulk structure, Ga and As supply $^3/_4$ and $^5/_4$ electrons to each bonding, respectively. This means without charge transfer, the dangling bonds of Ga and As carry $^5/_4$ and $^3/_4$ electrons, respectively. Charge transfer from the Ga atoms to the coordinated As atoms leaves an empty dangling bond at the Ga and forms a non-bonding lone pair (a filled dangling bond) at the As atom. This charge transfer is accompanied by a relaxation of the Ga atoms towards the plane of the As atoms below. The topmost Ga–As double layer becomes almost planar, i.e., the Ga atom adopts a sp^2-like orbital hybridization. On the other hand, the As atoms move towards the vacancy (as indicated by the arrows in Fig. 8) so as to adopt p^3 hybridization. The Ga vacancy in combination with the relaxations of Ga and As in the outermost layer induces a strain field which is partially relieved by displacements of Ga and As atoms in the second Ga–As double layer in form of a buckling of 0.1 Å.

The As trimer structure was determined by a quantitative LEED intensity analysis [64] as shown in Fig. 9. The As trimers are bonded to three As atoms in the next layer which are centered directly above the Ga atom in the second layer. The As–As distance in the As trimer is 2.37 ± 0.08 Å, i.e., only somewhat smaller than in the As_4 cluster (2.44 Å) and than the theoretically predicted values of 2.44 Å [61] and 2.46 Å [62]. The trimer is located 2.29 Å above the plane defined by the three attached As atoms underneath. This value is identical to the calculated value of 2.28 Å [61]. The rest atom (R in Fig. 9) pops up by 0.56 Å, indicating that this atom undergoes a rehybridization towards p^3, i.e., its dangling bond is filled with two electrons. Obviously, also for this reconstruction a charge transfer takes place, however, this time from the As trimer to the As rest atom. To elucidate this charge transfer, we apply again the electron counting rule. As already mentioned, Ga and As provide $^3/_4$ and $^5/_4$ electrons to each saturated bonding (occupied by two electrons), respectively, in a bulk-like environment. The As atoms in the trimer put one electron into the bondings with the other trimer atoms and $^3/_4$ electron to the back-bonding with the As atom underneath; note that the As atom underneath, which is more or less bulk-like, already supplies $^5/_4$ electrons to the bonding to the As trimer atom. Since the valency of As is 5, each of the dangling bonds in the As trimer would have to carry $^9/_4$ electrons in the dangling bond (i.e., $^1/_4$ electron too many). However, by transferring $^1/_4$ electron from each trimer As atom to the As rest atom, all As trimer atoms in the trimer have fully occupied dangling bonds, and the As rest atom is also satisfied.

The As trimer formation greatly distorts the substrate lattice, and therefore, large relaxations down to the sixth atomic layer are present to relieve the strain. In particular, the LEED analysis [64] found a vertical buckling of the Ga atom in the third layer and of the As atom in the fourth layer of 0.39 Å (z_3) and 0.31 Å (z_4), respectively, and a lateral displacement of a Ga atom of 0.17 Å (Δx_2). A quite similar pattern of strain relief was found for the Si trimer model for the Si(111)–($\sqrt{3} \times \sqrt{3}$) R30°–Ag surface [65].

2.6 Concluding remarks

Clean and adsorbate-covered semiconductor surfaces are frequently strongly reconstructed. Their particular surface structures are dominated by the tendency to reduce the number of dangling bonds, without introducing too much strain and leaving the surface electronically neutral. Main structural elements identified so far are dimers, trimers, and adatoms. Very often adsorbate-induced surface structures found on Si are equally found on Ge and vice versa. This can be employed in the determination of the atomic geometry (bypassing local minima in the r-factor surface) by measuring and analyzing a particular surface phase on both Ge and Si.

The surface structures discussed in this chapter are considered to be complex in two different ways. First, the reconstruction leads to surface structures which are very different from a bulk-terminated surface, and second, the reconstruction causes a strain field in the surface region which is relieved by large relaxations down to deep layers. Accordingly, the overlayer unit cell consists of at least four to five layers.

III. Coadsorption systems: structure and reactivity at metal surfaces

3.1 Introduction

This particular class of adsorption systems is relevant to the understanding of elementary steps in heterogeneously catalyzed reactions. It is well documented that in heterogeneously catalyzed reactions the reactants have to adsorb

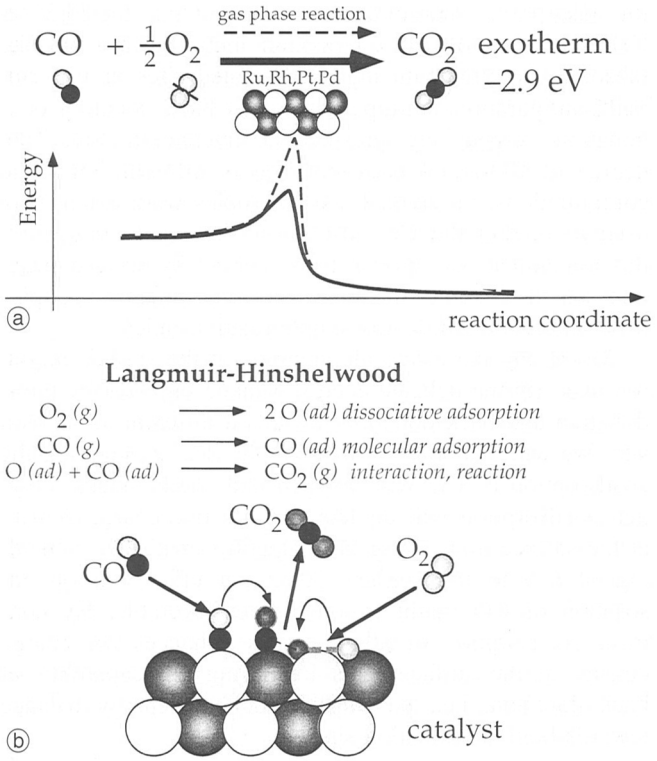

Fig. 10. (**a**) Qualitative potential curve as a function of the reaction coordinate with (solid line) and without employing a catalyst. The activation barrier is essentially determined by the O—O bonding. (**b**) The elemental steps according to the Langmuir-Hinshelwood mechanism are shown which occur during the CO oxidation reaction over a metal surface.

on the metal surface prior to their recombination [66]. This is the so-called Langmuir-Hinshelwood mechanism [67]. Let us now focus on a particularly simple reaction, e.g., the catalytic oxidation of carbon monoxide over platinum group metal surfaces, which is also important in the context of reducing the automotive emissions. This reaction is probably the most extensively studied reaction under ultra-high vacuum (UHV) as well as under real reaction conditions, qualifying it as a model system in surface chemistry and physics. The oxidation reaction of CO is exothermic by about 2.9 eV. However, its efficiency is low in the gas phase (homogeneous reaction) due to the high activation barrier imposed by the strong O-O binding, which has to be broken prior to the actual oxidation step of CO (cf. Fig. 10a). To lower this activation barrier, catalysts containing platinum group metal particles as the active centers are employed. Fig. 10b illustrates the CO oxidation reaction process over a platinum group metal surface. Here the molecular oxygen adsorbs dissociatively, thus automatically providing a kind of atomic oxygen species, which is able to react with adsorbed CO to form CO_2. CO_2 is weakly bound on the metal surface and therefore immediately released into the gas phase under reaction conditions. Charge density with proper symmetry (in particular d-charge density) from the metal surface interacts with the anti-bonding molecular orbitals of oxygen and causes oxygen molecules to dissociate upon approaching the surface. CO molecules chemisorb molecularly on the surface. They are able to strike adsorbed oxygen atoms due to their high mobility at the surface and occasionally form an activated complex (reaction intermediate) from which the recombinative reaction to CO_2 takes place. There are two points worthwhile to notice. First, structural and other properties of this activated complex may be closely related to corresponding properties of a mixed CO + O coadsorbate system which can be studied by surface sensitive techniques. Second, the CO oxidation reaction is still an activated process – although the activation barrier is substantially lowered compared to the homogeneous reaction – since the adsorbed oxygen atoms form quite strong bonds to the metal surface. The microscopic mechanism, which determines this activation barrier involved in the CO oxidation process, has still to be clarified. Generally, the binding energy of oxygen on the catalyst's surface governs how efficiently CO can be oxidized at the metal surface. Is the oxygen-metal binding energy too small (such as for Ag, and Cu), then oxygen dissociation is the rate-limiting step, resulting in a quite low turnover rate for the CO oxidation. The turnover rate [68] is defined as the number of CO_2 molecules produced per second and surface metal atom at a given CO partial pressure. But also for strong oxygen-metal bonds (such as for Ru) the activity is quite low. Right in between these extremes the reactivity for CO oxidation is highest (volcano curve), as found for Rh and Pt, which therefore are also essential constituents in the three-way automobile exhaust catalyst.

Even if a metal surface (in a metal catalyst) is not very active in terms of a particular reaction, its activity (and selectivity) can be markedly improved by using additives and promoters. One of the most prominent promoters are the alkali metals which serve as electronic modifiers [69]. For instance, it has been observed that under UHV conditions the Ru(0001) surface is not active at all in oxidizing CO. However, small quantities of Cs which were added to the surface increased the reaction probability by several orders of magnitude [70]. A dramatic increase in the reactivity of Ru(0001) is also accomplished when the CO oxidation reaction takes place under heavily oxidizing conditions which are able to maintain a (1×1)—O overlayer at the surface [71]. In this high O coverage phase, oxygen is notably less strongly bound (about 0.8 eV) [72] than in the low O coverage (2×2) phase which effect presumably is responsible for the observed high activity of this surface.

From this motivation the outline of the following chapter is straight forward. Starting with some general remarks on the bond formation of CO on transition metal surfaces (Blyholder model), we will be investigating the interaction of CO and O on platinum group metal surfaces such as Ru, Rh, and Ni. Next, we are discussing the high-coverage phase of oxygen on Ru(0001) and its impact on the high efficiency of the CO oxidation reaction. Third, we are concentrating on the interaction of Cs with CO which is aimed at receiving additional insight into the promoter effect of alkali metals in the CO oxidation reaction and the interrelation between electronic and structural properties of this coadsorbate system. Finally, we present some (preliminary) structural data for the ternary system consisting of CO, O, and Cs.

3.2 The chemisorption of CO molecules on transition metal surfaces: The Blyholder model

The most important molecular orbitals (MO) of the CO molecule, determining its reactivity, are the non-bonding 5σ (Highest Occupied MO: HOMO) and the anti-bonding $2\pi^*$ MO (Lowest Unoccupied MO: LUMO). The filled 5σ state acts as a donor state, while the $2\pi^*$ MO serves as an acceptor state. Upon chemisorption of a CO molecule on a transition metal surface, the 5σ–CO MO donates part of its electronic charge to band states of the metal substrate, exhibiting σ symmetry (σ donation, σ bonding). This process of σ donation is counterbalanced by back donation of charge density with π symmetry from the metal to the $2\pi^*$ MO of the CO. This back donation strengthens the metal-CO bond (back bonding) and concomitantly weakens the internal C–O bond. The C–O bond weakening can readily be monitored by vibrational spectroscopy, e.g., high-resolution electron loss spectroscopy (HREELS) and infrared absorption spectroscopy (IRAS): The C–O stretch frequency becomes the smaller the stronger the back bonding is developed. This concerted donor-acceptor mechanism is called Blyholder model [73] and the essential processes are illustrated in Fig. 11. The predominant contribution to the CO-metal bond comes from the back bonding. Is the back donation suppressed by missing *d*-charge density near the $2\pi^*$ MO level (as encountered with the quasi s-*p* metals, Cu, Ag, and Au), then the CO-metal bond is always weak [74]. From simple symmetry arguments, i.e., optimizing the overlap between MOs of CO with states of the substrate, it is clear that the CO adsorption site and therefore the minimum in the potential energy surface – PES – of this adsorption system is determined by the relative importance of σ donation and π back donation for the CO-metal bonding. The overlap of CO $2\pi^*$ orbitals with metal d_π orbitals works best in high-coordinated adsorption sites, while the overlap between CO–5σ and metal d_σ orbitals is maximized for on-top adsorption. Therefore, one may infer that the PES for CO chemisorption on a transition metal surface has the (absolute) minimum in high-coordinated sites or in terminal configuration (on-top sites) when back donation or σ donation, respectively, prevails the interaction. Since the degree of CO-metal back bonding is different for these configurations, vibrational spectroscopies were extensively used to predict the CO adsorption site. Quite frequently this assignment has proven to be correct by surface structure sensitive methods, but there are also many examples in the literature where this simple relation failed.

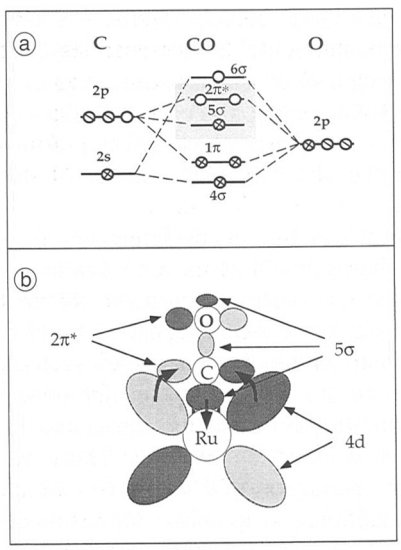

Fig. 11. (**a**) Molecular orbitals (MO) of CO, in particular the lowest unoccupied MO (LUMO) and the highest occupied MO (HOMO) are shown as linear combination of atomic orbitals. (**b**) Blyholder model: Charge transfer from the CO 5σ to the metal atom and back donation from Ru to the CO $2\pi^*$ MO.

Modifying the electronic situation at the surface might, however, tip the delicate energy balance imposed by the σ donation and back donation towards a different adsorption site. We will elaborate on this simple idea by studying the coadsorption of CO with oxygen and alkali metals. Oxygen coadsorption will deplete the effective charge density at the surface, thus being in competition with the π bonding of CO to the surface. As a net effect, on-top adsorption of CO might become more favorable. By contrast, coadsorption of alkali metals enhances the charge density at the surface, thus improving the capability of back donation, i.e., pushing the delicate energy balance towards high-coordination sites.

3.3 CO and O coadsorbed on the close-packed surfaces of Ru, Rh, and Ni

These metal surfaces are selected because Ru and Rh behave quite complementary with respect to their ability to catalyze the CO oxidation reaction. Ru is a quite poor catalyst under UHV conditions [75] and the reaction probability of an impinging CO molecule to be oxidized is below 10^{-5} at 550 K. Rh, on the other hand, shows reaction probabilities of $\geq 10\%$ for a sample temperature of 550 K [76]. Under strong oxidizing conditions, this sequence is reversed. Ru indicates reaction probabilities of 1% at 550 K [77], while Rh is inactive due to surface oxide formation [78].

For not too heavy CO loadings, CO molecules adsorb in on-top positions on Rh(111) [79] and Ru(0001) [80, 81], while on Ni(111) CO molecules chemisorb in threefold hollow sites [82]. This distinct adsorption behavior of CO motivated us to also study the Ni(111) surface and how the CO adsorption site might be affected by modifying the electronics at the surface. Obviously, a quite delicate energy balance within the Blyholder model determines the particular CO adsorption site on the clean transition metal surfaces. Upon flushing the surface with electron charge density (by alkali metal adsorption) or depleting the surface charge density (by oxygen adsorption), the adsorption site of CO molecules may change between high-coordinated and on-top positions.

As evidenced by thermal desorption spectroscopy, generally, the coadsorption of oxygen and CO destabilizes both species on the surfaces compared to the case for which each of these species is chemisorbed alone on the surface. The reason is that CO (owing to its back bonding) and oxygen (as a strongly electronegative species) compete for the same electron charge density offered by the substrate surface. Structurally, the coadsorption of CO

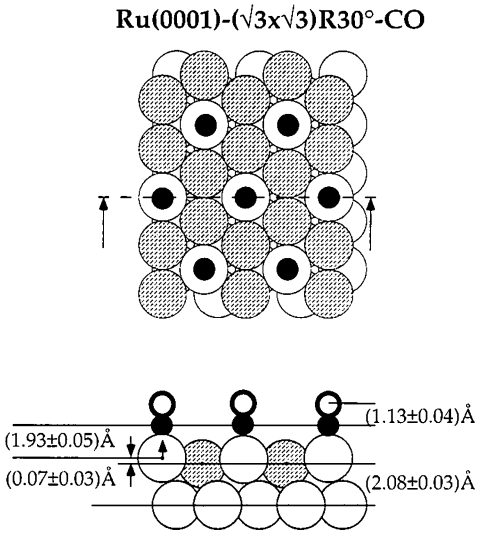

Fig. 12. The bond configuration of CO on Ru(0001) forming a $(\sqrt{3} \times \sqrt{3})$ R30° overlayer. CO resides in on-top position and induces an outward displacement of the attached Ru atom by 0.07 Å [81].

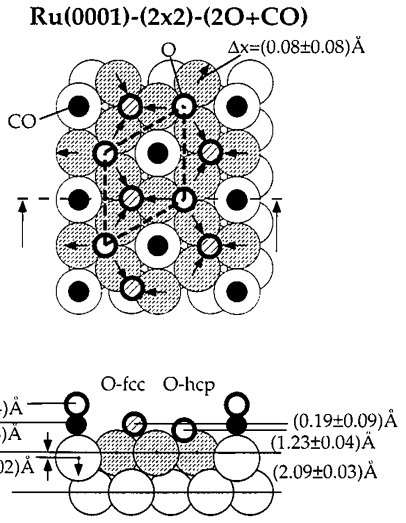

Fig. 13. The atomic geometry of the Ru(0001)−(2 × 2)−(2 O + CO) surface [85]. Oxygen atoms sit in *hcp* and *fcc* sites arranged in a honeycomb network in order to open on-top for CO chemisorption.

into the (2 × 2)−O precovered Ru(0001) surface, for instance, results in the formation of two distinct CO + O phases, namely the (2 × 2)−O + 1 CO and the (2 × 2)−O + 2 CO phase [83]. The atomic geometry of the Ru(0001)−(2 × 2)−O + 1 CO surface has been investigated by LEED [84]. It was found that CO molecules adsorb in on-top positions as also found on the clean Ru(0001) surface (cf. Fig. 12). Since the back bonding of CO is weakened by the presence of oxygen, the preference of CO for the on-top position is even enhanced compared to the clean surface. The observed static tilting of CO away from the oxygen atom is attributed to the repulsive interaction between O and CO. By dosing several 10000 L of CO one is even able to accommodate a second CO molecule in the (2 × 2)−O unit cell. From IRAS measurements [83] it was concluded that this second CO molecule adsorbs in the threefold *fcc* position. Comparing TD spectra indicate that the *fcc*-CO species is notably less stable than the on-top CO, in accordance with the electronic situation at the surface which facilitates σ donation rather than π back donation.

A peculiar situation is encountered when a (2 × 1)−O precovered Ru(0001) surface is exposed to CO. The original Ru(0001)−(2 × 1)−O surface does not provide any on-top sites for CO adsorption on steric grounds. Consequently, the (2 × 1)−O surface is not able to accommodate substantial amounts of CO at room temperature. However, if the sample temperature is raised to 500 K, appreciable amounts of CO molecules can adsorb. A recent LEED analysis [85] disclosed that the (2 × 1)−O network rearranges into a (2 × 2) honeycomb structure with one oxygen atom in the *hcp* and the other in the fcc site (cf. Fig. 13). In this way, the oxygen overlayer opens on-top sites on which CO molecules can chemisorb. The driving force of CO to occupy on-top positions is obviously so strong that even the less favorable *fcc* site is occupied by oxygen. DFT calculations indicate that the energy difference between the *fcc* and *hcp* position is 0.1 eV ... 0.3 eV at O coverages between 0.75 and 0.5 [72]. CO adsorption in on-top position might be more favorable by about this energy difference than any other adsorption sites. Altogether, these findings nicely demonstrate that on-top adsorption of CO is clearly preferred under oxidizing conditions on Ru(0001).

A quite similar picture emerges when moving on to the coadsorption of CO and O on the Rh(111) surface. Starting from a (2 × 2)−O precovered Rh(111) surface, CO coadsorption is again able to form a (2 × 2)−O + 1 CO and a (2 × 2)−O + 2 CO phase [86]. Also for the O precovered Rh(111) surface the on-top position for CO is clearly favored as also found for the clean Rh(111) surface. Only when all available on-top sites in the (2 × 2)−O overlayer are filled, CO adsorption proceeds into fcc sites. This behavior has been confirmed by high-resolution XPS measurements performed in Andersen's group [87]. On-top and threefold hollow adsorption of CO results in distinct C−1s core level shifts which in turn can be used as 'fingerprints' to identify the adsorption site. The C−1s core levels of on-top CO are shifted to higher energies. The LEED analysis [86] retrieved that the local O−Rh adsorption configuration is altered by the presence of CO: The Rh−O bond length changes from 2.00 Å ((2 × 2)−O) to 2.06 Å ((2 × 2)−O + CO) (cf. Fig. 14), i.e., the O−Rh bond strength decreases upon CO coadsorption.

CO adsorption on the clean Ni(111) surface takes place in threefold hollow sites up to moderate CO coverages, indicating that CO back bonding dominates the potential energy surface (PES). Upon coadsorption of oxygen, which degrades the back bonding of CO to the Ni surface, one might predict that CO molecules adsorb in on-top positions. It is, however, not clear whether this oxygen-induced weakening of the CO back bonding is strong enough to force a site change of CO. Therefore, it was not too surprising that a recent photoelectron diffraction study [88] found that CO molecules adsorb also on the (2 × 2)−O precovered Ni(111) surface in the threefold hollow position. Recent high-resolution XPS measurements by Held et al. [89] suggested, however, that CO prefers the on-top position on the (2 × 2)−O precovered

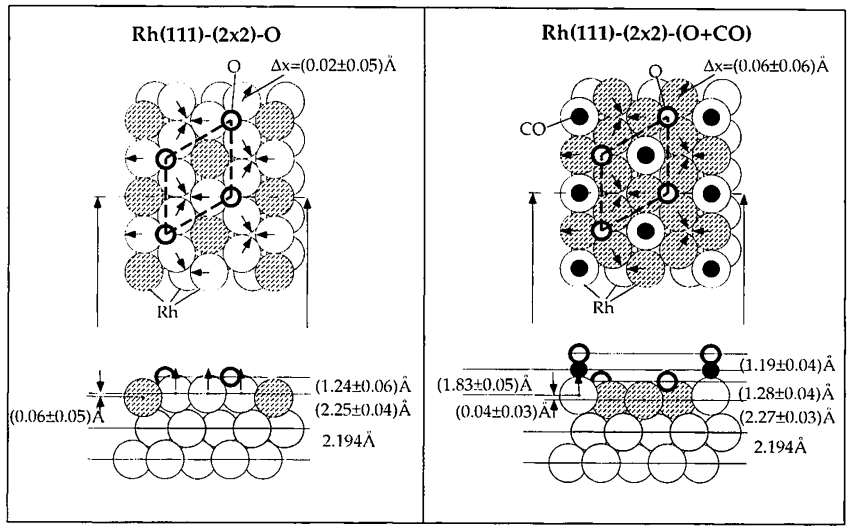

Fig. 14. The atomic geometry of the Rh(111)−(2 × 2)−(O + CO) surface [86]. Oxygen atoms occupy fcc sites, while CO adsorbs in on-top position. The coadsorption of CO weakens the O−Rh bonding, the O−Rh bond length changes from 2.00 Å (clean Rh(111)) to 2.06 Å in the coadsorbate phase.

Ni(111) surface. Motivated by this XPS study, a LEED structure analysis of the Ni(111)−(2 × 2)−O−CO coadsorbate system was carried out. The result was unequivocally in favor of CO being adsorbed in on-top position [90]. Therefore, a quite general feature of CO chemisorption is captured: Oxygen coadsorption pushes the delicate balance between σ bonding and π back bonding of CO to a transition metal surface toward on-top adsorption.

3.4 Oxygen adsorption on Ru(0001) and Ru(10$\bar{1}$0)

As outlined in the introduction, the binding energy of oxygen to the metal surface essentially determines the height of the activation barrier for the CO oxidation reaction. A peculiarity of ruthenium is that under strongly oxidizing conditions the turnover rate of CO_2 increases drastically, while for the other platinum group metals heavily oxidizing conditions inhibit the CO oxidation reaction. This demonstrates the particular relevance of oxygen adsorption on the Ru(0001) surface to the CO oxidation process and might be related to the O−Ru binding energy which decreases markedly with increasing coverage without forming a surface oxide. It should be noted that the oxidation process of Ru and Rh is still not completely understood. In addition, the adsorption geometry of the O/Ru system reveals features which are anomalous or at least counter-intuitive in that with decreasing O−Ru binding energy the O−Ru bond length becomes shorter.

The Ru(0001) surface is able to accommodate several monolayers of oxygen without building up an oxide structure such as RuO_2. At low oxygen coverages the (2 × 2)−O and (2 × 1)−O phases are formed with O coverages of 0.25 and 0.50, respectively. Detailed LEED analyses of these O phases [91, 92] indicated that the adsorption process is accompanied by pronounced local reconstructions of the top two Ru layers. The Ru−O bond lengths turned out to be 2.03 Å in both phases. Using either high O_2 exposures or applying NO_2 exposures as a source of atomic oxygen, one can bring even more oxygen on the surface transforming the (2 × 1)−O into a (2 × 2)−3O and eventually into a (1 × 1)−O phase [93]. Only when this (1 × 1)−O phase is completed, oxygen

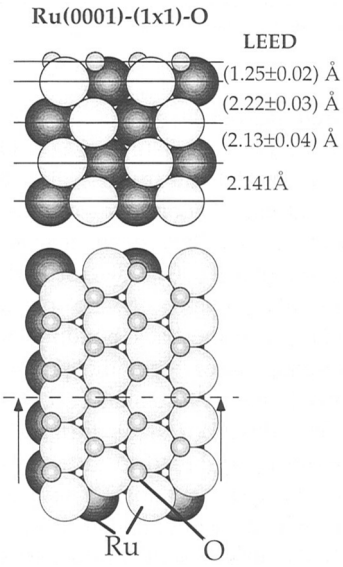

Fig. 15. The atomic geometry of the Ru(0001)−(1 × 1)−O surface [93]. Oxygen atoms reside in hcp sites and induce a quite strong expansion of the topmost Ru layer spacing by 3.5%.

incorporation into the subsurface region sets in, maintaining a (1 × 1)−O overlayer on the surface. For the pure (1 × 1)−O overlayer phase (without subsurface oxygen) the Ru−O bond length turned out to be 2.00 Å which is slightly shorter than that found in the (2 × 2)−O and (2 × 1)−O phases. The most apparent structural feature of the Ru(0001)−(1 × 1)−O surface [93] is the marked expansion of the topmost Ru layer spacing by 3.5% (cf. Fig. 15). It was argued that this expansion is required to allow for O penetration into the subsurface region [93]. For all these overlayer phases DFT calculations were performed. The Ru−O binding energies (with respect to the molecular oxygen) are compiled in Fig. 16. Clearly, the Ru-O binding energy drops by about 0.8 eV when going from the (2 × 2) to the (1 × 1) overlayer which is indicative of a net repulsion between the O atoms on the surface. Yet both DFT calculations and LEED simulations show that the Ru−O bond lengths become slightly shorter when going from the low to the high coverage O phase. A possible interpretation will be given after presenting the

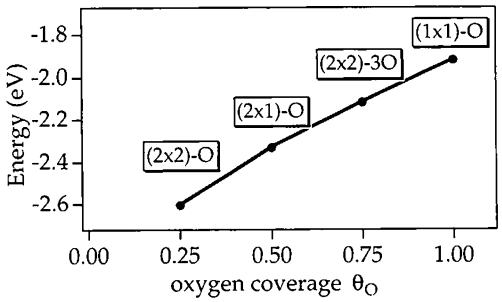

Fig. 16. The O-Ru bonding energy of *hcp*-O and *fcc*-O as a function of the O coverage with respect to the half binding energy of O_2 [93]. *hcp*-O is always preferred over *fcc*-O, although the difference amounts to only 30 meV in the high-coverage (1 × 1) phase.

structural results of the oxygen adsorption on the Ru(10$\bar{1}$0) surface. DFT calculations of the Ru(0001)–(1 × 1)–O phase also indicated an expansion of the topmost Ru layer spacing, demonstrating that this expansion is of purely electronic origin and is not due to subsurface oxygen.

Oxygen adsorption onto Ru(10$\bar{1}$0) leads to the formation of two ordered overlayers, i.e., a c(2 × 4)–2O and a (2 × 1)pg–2O phase, which were analyzed by low-energy electron diffraction [94]. The structural parameters are summarized in Figs. 17 and 18. In both phases oxygen occupies the threefold coordinated hcp site along the densely packed rows on an otherwise unreconstructed surface, i.e., the O atoms are attached to two atoms in the first Ru layer (Ru(1)) and to one Ru atom in the second layer (Ru(2)). Obviously, oxygen prefers to bind to the low-coordinated Ru atoms of the topmost layer. This finding may

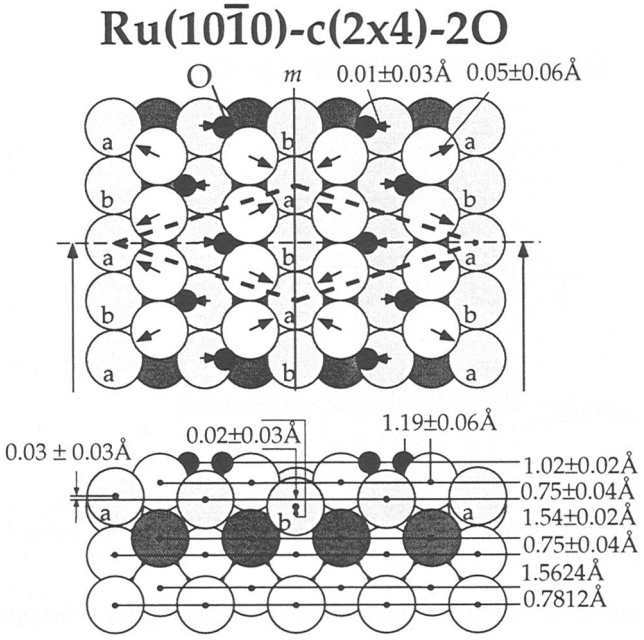

Fig. 17. The atomic geometry of the Ru(1010)–c(2 × 4)–2O surface [94]. Oxygen atoms reside in *hcp* sites on the flanks of the trenches, i.e., O atoms are attached to two atoms in the top Ru layers (Ru(1)) and one Ru in the second Ru layer (Ru(2)). Within the troughs, the O–O interaction is attractive indicated by the zigzag chains. The zigzag chains are separated by empty channels. This ensures that Ru atoms in the topmost layer are not shared by more than one O atom. The Ru–O bond lengths are d(O–Ru(1)) = 2.08 Å and d(O–Ru(2)) = 2.03 Å.

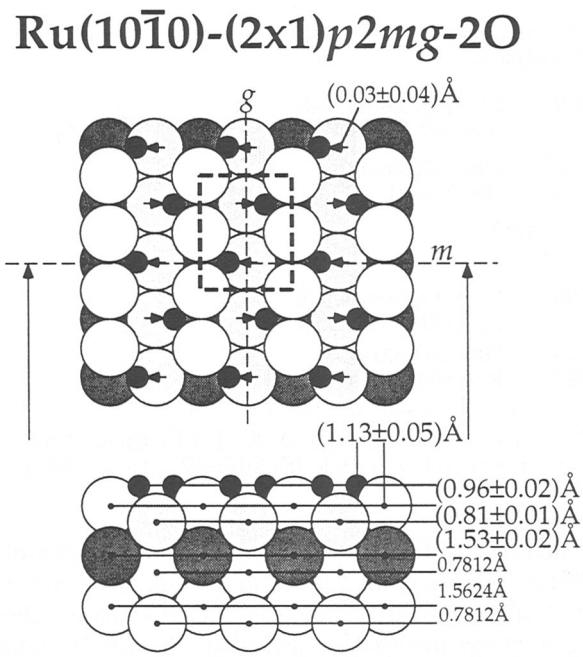

Fig. 18. The atomic geometry of the Ru(1010)–(2 × 1)pmg–2O surface [94]. The main difference to the c(2 × 4)–2O phase is the occupation of the empty troughs by oxygen. The oxygen atoms have therefore to share Ru atoms in the top layers (Ru(1)) with other oxygen atoms. The O–Ru bond lengths are *d*(O-Ru(1)) = 2.01 Å and *d*(O–Ru(2)) = 2.03 Å. The shortening of the O–Ru(1) upon O coverage can be explained by local charge density arguments.

be rationalized in the following way. The local charge density of the low-coordinated Ru atoms Ru(1) is larger than of high-coordinated Ru atoms Ru(2), since less charge density has to be supplied to the internal bonds between the Ru atoms (tight binding argument [95]). Using now effective medium theory arguments, which have been put forward by Nørskov and coworkers [96], the bonding between oxygen and Ru depends critically on the local charge density offered by the substrate: The more local charge density is available, the longer the O-Ru bond length. This aspect of the Ru–O bonding is disclosed by the structure of the Ru(10$\bar{1}$0)–c(2 × 4)–2O overlayer. The bond length of O to Ru(1) with 2.08 Å is substantially longer than that between O and Ru(2) (2.03 Å).

The next apparent structural characteristics of these O phases is the formation of zigzag chains along the troughs. Both LEED and HREELS measurements give evidence that even at low O coverages these chains are preferentially formed. This means that the interaction between the oxygen atoms along the zigzag chains is attractive. Albeit this attractive interaction, oxygen does not like to share attached Ru atoms with other oxygen atoms. This attribute becomes evident by the appearance of empty trough between the zigzag chains observed in the c(2 × 4)–2O system (cf. Fig. 17). If, however, the O coverage is increased, the empty troughs are filled up with the consequence that oxygen atoms have now to share common Ru atoms in the topmost layer. Accordingly, the local charge density offered for each O atom is smaller, and again, using the simple effective medium theory of bonding, this tells us that the oxygen atoms have to come closer to the surface to experience the same (optimum) local charge density as in the c(2 × 4)–2O phase. In fact, this aspect has been

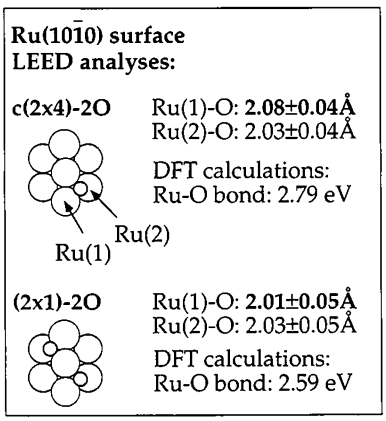

Fig. 19. A comparison of the local O–Ru bond configurations of Ru(1010)–c(2 × 4)–2O surface and Ru(1010)–(2 × 1)pmg–2O surface.

identified by a LEED analysis in that the bond lengths of O to Ru(1) changes from 2.08 Å to 2.01 Å when going from the c(2 × 4)–2O to the (2 × 1)–2O phase. The bonding between the oxygen atom and the Ru(2) atom directly underneath is not affected by the presence of additional oxygen on the surface, as reflected by the unchanged bond length of 2.03 Å. These findings (summarized in Fig. 19) cannot be easily reconciled with simple arguments adopted from coordination chemistry since there the bond length is strictly related to the bond strength: The weaker the bonding the longer the respective bond length. Total-energy calculations show that the binding energy of oxygen is reduced by about 0.26 eV when two oxygen atoms have to share one Ru atom in the topmost layer. Accordingly, the O–Ru(1) and O–Ru(2) bond lengths should increase which, however, is not observed experimentally. It seems therefore that the shortening of the Ru(1)–O bond length with O coverage is a consequence of the competition for electron charge density.

3.5 O and Cs coadsorbed on the Ru(0001) surface

The interaction of Cs with oxygen is dictated by the chemical reactivity of these two species in forming various oxides. Therefore, when both Cs and O are brought on the Ru(0001) surface, one could anticipate to find Cs–O elements reminiscent of a Cs oxide structure. The complex Cs–O chemistry on the Ru(0001) surface manifests itself in a complex phase diagram as demonstrated in Fig. 20. The coadsorption of Cs and O leads to various ordered overlayer structures; for a comprehensive discussion of the geometric structures the reader is referred to Bludau et al. [97].

We start with a horizontal cut through the qualitative Cs–O phase diagram at a Cs coverage of 0.33. The ordered Cs/Ru(0001)–($\sqrt{3} \times \sqrt{3}$) R30° structure transforms into a new incommensurate superstructure already by dosing small amounts of oxygen (0.05 L). This demonstrates a strong interaction between oxygen and the Cs adsorbate layer. Oxygen exposures between 0.3 and 0.9 L and subsequent annealing to 350 K give rise to a reappearance of the ($\sqrt{3} \times \sqrt{3}$) R30° structure exhibiting a Cs:O stoichiometry of 1:1. A respective LEED structure analysis [98] has provided a model in which Cs and O atoms are

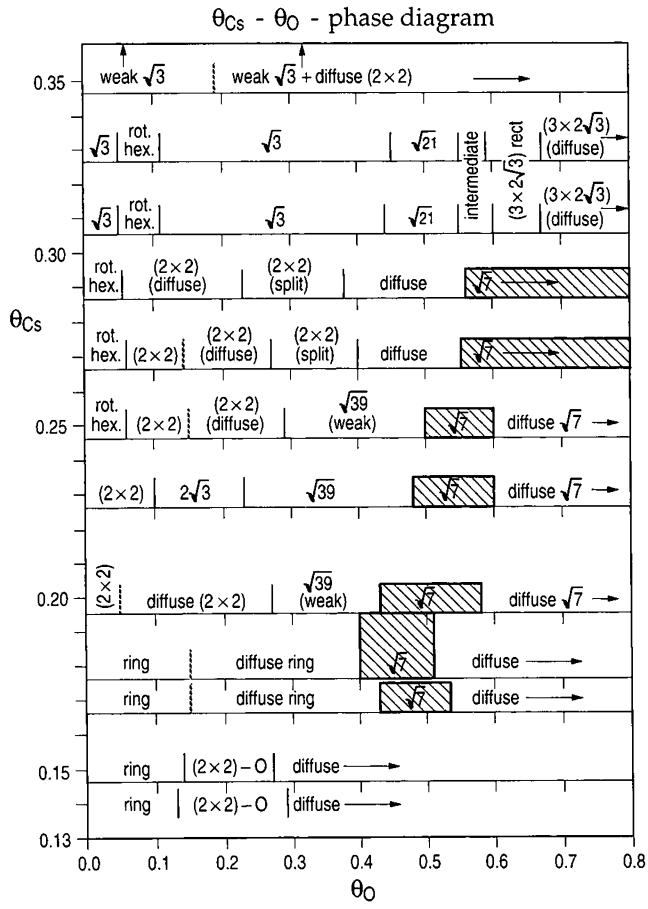

Fig. 20. Experimentally derived phase diagram for cesium and subsequently adsorbed oxygen on the Ru(0001) surface for T = 310 K (only for the preparation of the ($\sqrt{3} \times \sqrt{3}$) R30° structure annealing to 350 K was required to obtain sufficient long-range order) [97].

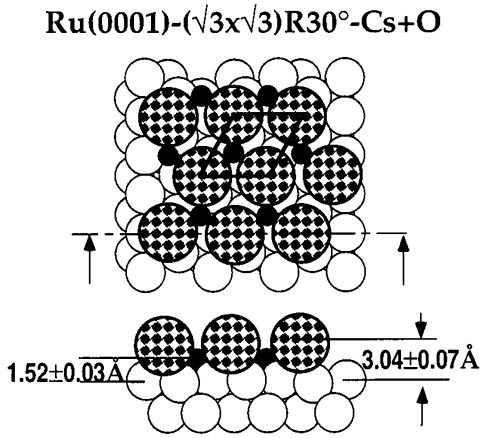

Fig. 21. Side and top view of the ($\sqrt{3} \times \sqrt{3}$) R30° structure on Ru(0001). Both Cs and O reside in hcp sites [98]. The Cs radius is 2.1 Å, the O radius is 0.8 Å.

located in hcp sites with respect to the Ru(0001) substrate lattice; structural parameters are summarized in Fig. 21. The chess board pattern of consecutive Cs and oxygen atoms reminds one of a 'salt-like' structure which allows the greatest number of oppositely charged 'ions' to touch without requiring any squeezing together of 'ions' with the same charge. Compared to the structures of the respective pure adsorbate phases, the O–Ru and Cs–Ru bond lengths are modified in a way that is consistent with a net

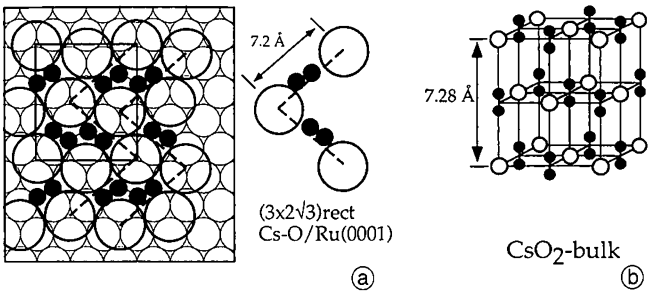

Fig. 22. A comparison of the real space model for the $(3 \times 2\sqrt{3})$ rect. structure (**a**) with the (010) surface of CsO_2 (**b**). The common structural elements in (**a**) and (**b**) are the Cs–O–O–Cs chains which are zigzag like in the $(3 \times 2\sqrt{3})$ rect. phase and linear in CsO_2(010) [97].

transfer of electronic charge from Cs to O: The oxygen hard-sphere radius increases by 0.12 Å, and the effective Cs radius decreases from 2.2 Å [99] in the clean Cs/Ru(0001) phase to 2.1 Å with the coadsorbate phase [98].

Further exposure of O_2 to the $(\sqrt{3} \times \sqrt{3})$R30°–Cs + O overlayer leads to the development of a $(3 \times 2\sqrt{3})$-rect. structure at $\theta_O = 0.68$, yielding a stoichiometry Cs:O = 1:2. Both the appearance of a glide-plane symmetry and the dominance of certain LEED beams in the LEED pattern give evidence for a model exhibiting distinctive Cs–O–O–Cs zigzag chains. The interatomic Cs spacing in these chains (7.2 Å) agrees well with that found in crystalline CsO_2 (7.28 Å) (Fig. 22); note that the stoichiometry in the (010) surface of CsO_2 is also Cs:O = 1:2. The higher density of Cs atoms in the $(3 \times 2\sqrt{3})$-rect. structure (0.052 atoms/Å^2) compared to that in the (010) surface of CsO_2 bulk (0.044 atoms/Å^2) causes appreciable stress in the Cs–O overlayer which is presumably relieved by the formation of zigzag instead of linear Cs–O–O–Cs chains.

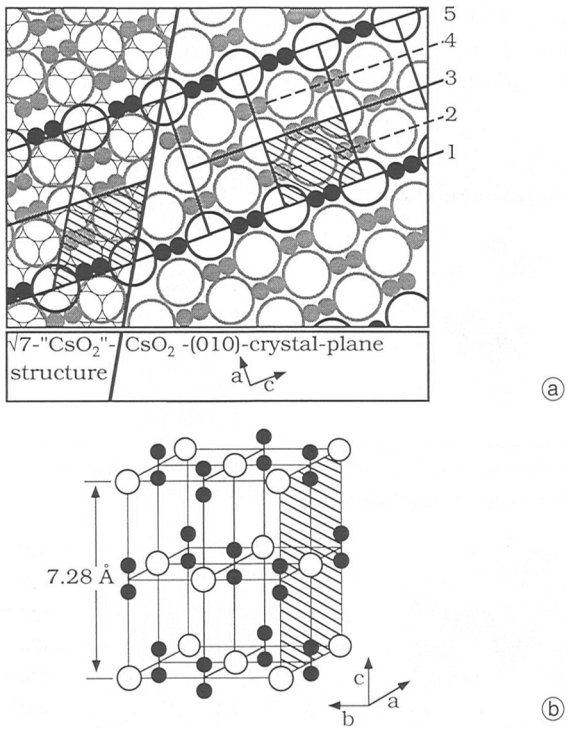

Fig. 23. Structure model for Ru(0001)–$(\sqrt{7} \times \sqrt{7})$R19.1°–Cs–O (**a**) in comparison with the (010) surface of CsO_2 bulk material (**b**) [97].

If this simple picture holds, one would expect to find linear Cs–O–O–Cs chains when reducing the Cs density at the Ru(0001) to about 0.044 atoms/Å^2, which is equivalent to a Cs coverage of 0.28. Saturating such a Cs precovered Ru(0001) with oxygen leads to the formation of a $(\sqrt{7} \times \sqrt{7})$R19.1° structure again with Cs:O stoichiometry of 1:2. A promising structure model [97] is depicted in Fig. 23, which is brought face to face with the (010) surface of CsO_2. As speculated before, the structural element now is a linear Cs–O–O–Cs chain whose appearance is a compromise of attaining a Cs–O bond length comparable to CsO_2 and the interaction of the Cs–O complex with the underlying substrate surface. The Cs density in this $\sqrt{7}$ structure (0.045 atoms/Å^2) is almost the same as in the (010) plane of CsO_2 so that in the Cs–O overlayer only the corrugation of the substrate surface exerts stress which is uniaxially relieved: Cs–O chains 2 and 3 (Fig. 23) are parallel-shifted by 3.6 Å (half length of the $\sqrt{7}$ periodicity) and compressed more tightly in the direction perpendicular to the chains.

An eye-catching feature of the phase diagram (Fig. 20) is the existence of the $(\sqrt{7} \times \sqrt{7})$R19.1° structure over a wide range of Cs coverages, while the respective optimum oxygen coverage is determined by the stoichiometry of two oxygen atoms per Cs atom. The presence of the $(\sqrt{7} \times \sqrt{7})$R19.1° LEED pattern down to coverages as low as 60% of the nominal Cs coverage demonstrates island growth and underlines the strong tendency of Cs and O to build up a CsO_2 surface species. Upon raising the sample temperature, these $(\sqrt{7} \times \sqrt{7})$R19.1° islands dissolve as observed in LEED by the transformation of a $(\sqrt{7} \times \sqrt{7})$R19.1° pattern into a ring-like pattern intersecting the nominal $\sqrt{7}$ spots [100]. The ring-like LEED pattern indicates that the $\sqrt{7}$ distance is still abundant, and since Cs is a much stronger scatterer than oxygen, this might be attributed to the persistence of Cs–O–O–Cs clusters while losing the azimuthal order of these clusters. As discussed before, even for Cs coverages higher than the density of the CsO_2 bulk (010) plane, the Cs–O overlayer forms a $(3 \times 2\sqrt{3})$ rect. lattice, exhibiting Cs–O–O–Cs zigzag chains instead of linear chains.

In summary, these findings provide compelling evidence for the formation of two-dimensional Cs oxides with a stoichiometry of two oxygen atoms per Cs atom. The commensurability of the $\sqrt{7}$ and the $(3 \times 2\sqrt{3})$ rect. phase reflects the influence of the corrugation potential of the substrate on the formation of these structures.

3.6 CO and Cs coadsorbed on the Ru(0001) surface

We will start the discussion with a few remarks on the system Cs/Ru(0001) which reveals several general features common to alkali metal adsorption on metal surfaces; a review of structural properties of the alkali metal adsorption on Ru(0001) can be found in Ref. [101]. The bonding between Cs and the Ru(0001) substrate works mainly through a charge transfer of the loosely bound Cs–6s electron to the substrate, resulting in a work function change shown in Fig. 24 [102]. At the beginning of Cs deposition the work function decreases linearly with coverage, i.e., the electric dipole moment formed by the ad-

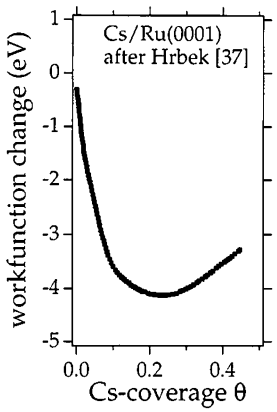

Fig. 24. The change in work function depending on the coverage of Cs adsorbed on Ru(0001) [102].

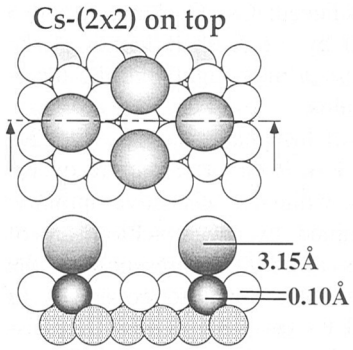

Fig. 25. Structure model for the Ru(0001)–(2 × 2)–Cs surface. Cs atoms sit in on-top positions and induce an inward displacement of the attached Ru atoms in the top Ru layer by 0.10 Å [99].

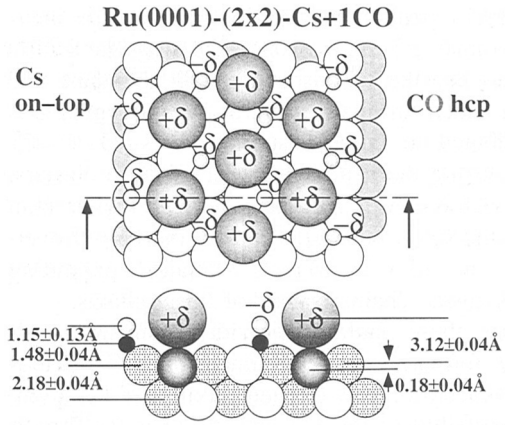

Fig. 26. The atomic geometry of the coadsorbate phase Ru(0001)–(2 × 2)–Cs–CO [40]. Cs atoms remain in on-top positions, while the CO molecules reside in hcp positions. CO molecules change the adsorption site from on-top (clean Ru(0001)) to threefold hollow sites on purely electronic grounds.

sorbate complex is independent of the coverage. With increasing coverage the mutual depolarization of the dipoles gives rise to the nonlinear variation of the work function $\Delta\Phi$ with coverage, indicating a transition of the adsorbed particles from an 'ionic' to a more 'metallic' state. In the depolarization regime the back flow of charge from the substrate (together with a decrease of the dipole moment) is accompanied by a decrease of the adsorption energy with coverage. Around a Cs coverage of $\theta = 0.25$, which is characterized by the formation of the (2 × 2) structure observed in LEED, $\Delta\Phi$ reaches a minimum, followed by a continuous increase until saturation near the value for the bulk Cs is reached. The enhanced singlet-triplet conversion of metastable He^* atoms found in MDS measurements for the (2 × 2)–Cs structure compared to lower coverages was interpreted in terms of a metallization of this overlayer [103] consistent with the interpretation of corresponding HREELS measurements [104]. The structure of the Ru(0001)–(2 × 2)–Cs phase (cf. Fig. 25) is defined by Cs atoms sitting in terminal positions and displacing the attached Ru inwards by about 0.1 Å.

Exposing this (2 × 2)–Cs surface to CO leads to the development of a mixed Cs + CO phase with (2 × 2) symmetry. A recent LEED analysis of this coadsorbate system [105] revealed that the Cs atoms remain in on-top position, while CO switches from on-top (clean Ru(0001) surface) to a threefold coordinated hcp site (Cs precovered surface). The corresponding structure is depicted in Fig. 26. The site change of CO can be explained if one recalls that high-coordination sites facilitate back donation, while on-top occupation favors the mechanism of σ donation. Hence, the actual adsorption site of CO will be the result of a delicate balance between both contributions determining the energetically lowest adsorption geometry. Furthermore, it is known from theoretical studies of related alkali-metal/metal systems that the adsorption energy difference for Cs at different adsorption sites is only very small (about 20 meV) [106]. Therefore, the total energy of the mixed (CO + Cs) system is essentially governed by the adsorption energy of CO. The presence of coadsorbed alkali-metal atoms improves the capability of back donation, due to the enhanced electron charge density at the surface, and hence forces CO to change its adsorption site from on top to high-coordination positions. Recall that the overlap of CO $2\pi^*$ orbitals with metal d_π orbitals works best in high-coordinated adsorption sites, while the overlap between CO–5σ and metal d_σ orbitals is maximized for on-top adsorption (cf. Fig. 27). Another aspect of the bonding geometry of (Ru(0001)–(2 × 2)–Cs + CO) is

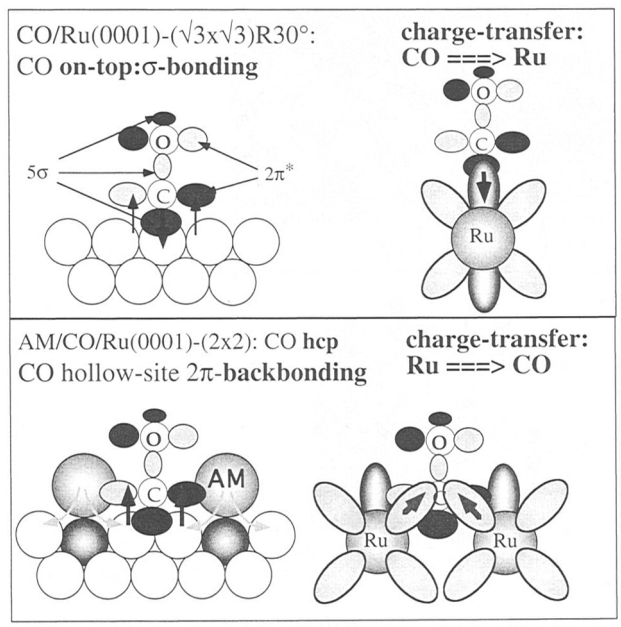

Fig. 27. The overlap of the frontier orbitals of CO with substrate orbitals assuming on-top and hcp adsorption.

the enhanced Cs-induced buckling (0.18 Å) found in the topmost Ru layer when compared to the clean (2 × 2)–Cs (0.10 Å) surface. This effect can be traced back to the additional bonding of the remaining three Ru atoms in the (2 × 2) unit cell to the CO molecules, which in turn weakens the Ru–Ru bonding to the single Ru atom beneath the Cs atom and hence allows for an enhanced rumpling of the topmost Ru layer.

The direct interaction between Cs and CO is very weak, as demonstrated by the inhibition of CO chemisorption on multilayers of Cs on Ru(0001) for temperatures above 100 K. A multilayer Cs film essentially offers electron charge density with σ symmetry which allows for a σ bonding of CO to the surface but not for a tight back bonding. However, when Cs and CO are brought together onto a Ru(0001) surface, they interact strongly with each other, as evidenced by the effect of thermal stabilization of each adsorbate. The thermodesorption spectra (cf. Fig. 28) of singly adsorbed Cs and CO in comparison with the mixed Cs + CO phase show that both species are thermally stabilized as indicated by the coincident desorption of both species at about 700 K. According to the discussion of the adsorption geometry of the Cs + CO phase, this thermal stabilization is attributed to a substrate-mediated interaction between these species: The alkali metal over-layer enriches the surface with electron charge density that the CO molecule in turn uses to establish a stronger back bonding to the Ru(0001) surface. This would explain why CO is more strongly bound to the substrate. But Cs atoms are also more strongly bound to the Ru(0001) surface since this mediated charge transfer from Cs to CO re-ionizes the Cs atom which in turn strengthens the bond of Cs to the substrate, according to the simple Langmuir-Gurney model.

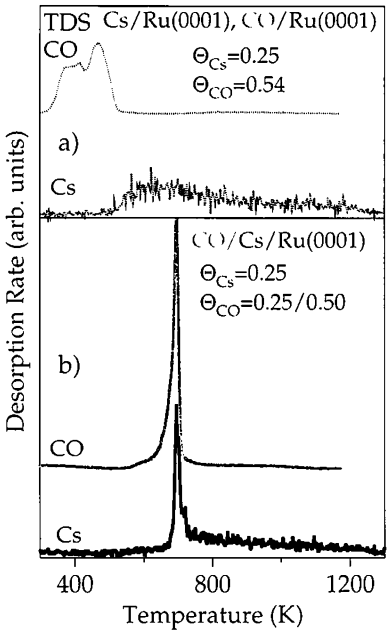

Fig. 28. Thermal desorption spectra of the systems: (**a**) Ru(0001)–CO: saturation of CO at 300 K and Ru(0001)–(2 × 2)–Cs; (**b**) Ru(0001)–(2 × 2)–Cs–CO [107]. Upon coadsorption, both Cs and CO are stabilized. The coincident desorption feature of Cs and CO at 650 K is indicative of an auto-catalytic desorption process.

The substrate mediated charge transfer from Cs to CO is supported by recent HREELS measurements which revealed that the C–O stretch frequency is reduced substantially from 252 meV for clean Ru(0001) surface to 203 meV for the (2 × 2)–Cs precovered Ru(0001) surface [104] consistent with an increased back donation into the anti-bonding CO 2π orbital. The re-ionization of the Cs overlayer has also been evidenced by HREELS by monitoring the Cs against substrate vibration. For small Cs coverages, this vibration showed up in HREEL spectra at about 8 meV. This vibrational loss, however, disappeared for Cs coverages beyond 0.25, due to the metallization of the Cs layer which efficiently screens the dipole excitation. If CO is coadsorbed into such a metallic (2 × 2)–Cs overlayer, the Cs–Ru vibration reappears [104], which is in line with the interpretation of a re-ionized or demetallized Cs overlayer. The demetallization of the Cs overlayer upon CO coadsorption was also seen by the deexcitation spectroscopy of metastable He atoms [103b].

The preceding discussion would only explain the stabilization of Cs–CO dimers. Actually, it has been observed that Cs and CO are able to form 2 × 2–(Cs + CO) islands on Ru(0001) down to Cs coverages of 0.05 [107]. These indicates a rather strong attractive interaction between Cs and CO which might be attributed to the gain in Madelung energy as proposed for the case of K + CO–Ni(100) [108, 109]. The gain in Madelung energy originates from the electrostatic attraction of oppositely charged particles ($Cs^{+\delta}$ and $CO^{-\delta}$) and the improved screening of the dipole-dipole repulsion between the $Cs^{+\delta}$ ions by immersed $CO^{-\delta}$ ions. The observed critical Cs coverage of 0.05 was rationalized by a Born-Haber cycle [110]. It is well-documented that the adsorption energy of alkali-metals (AMs) dramatically changes with coverage due to the operation of dipole-dipole repulsion among the AM atoms on the surface as observed in TDS; recall that the main effect is not related to the direct dipole-dipole repulsion but rather to the depolarization which is accompanied by a weakening of the AM to substrate bonding via charge back donation [107]. To form (2 × 2)–Cs + CO islands, the Cs atoms have to be brought together into a (2 × 2) network. If the Cs coverage is below 0.25 the hypothetical islanding costs energy and this the more the smaller the Cs coverage is (the energy difference can easily amount to several eV). This energy cost is counterbalanced by the energy gain which is achieved by coadsorbing CO molecules into the Cs-(2 × 2) lattice instead of into the dispersed Cs-phase. The energy gain constitutes the improved binding of the CO molecules to the Ru substrate (through improved back-donation into the $2\pi^*$ molecular orbital), the (2 × 2) arranged Cs atoms get more strongly ionized due to the charge flow from the Cs to the CO molecule thus strengthening also their bonding to the substrate, and last the electrostatic attraction between the partially ionized Cs atoms and CO molecules. The energy gain is independent of the particular Cs coverage as long as the Cs:CO stoichiometry is fixed in the islands. However, the energy cost for bringing the Cs atoms together increases with decreasing Cs coverage so that below a critical Cs coverage the energy cost might dominate prohibiting the for-

mation of (2×2)–Cs + CO islands on energetic grounds. In our case this critical Cs coverage turned out to be 0.05.

3.7 The ternary system consisting of O, Cs, and CO coadsorbed on Ru(0001)

To the best of our knowledge, this is the first report of a ternary coadsorption system whose structure has been determined by a surface crystallographic method. The ternary Cs + O + CO system can be considered as a model system for the Cs promoted CO oxidation reaction over Ru(0001) which was also the motivation for us to study this ternary system. Special emphasis has been put on the atomic geometry and how structural parameters change, when the three species, i.e., Cs, CO, and O, are brought together. One of the main difficulties to study the ternary C + CO + O system on Ru(0001) by using the LEED technique is the preparation of an ordered overlayer. In doing so, we started with a (2×2)–O structure on Ru(0001). At the NBL, Brookhaven [111], and also in preliminary experiments at the FHI [112], the (2×2) surface symmetry was shown to persist upon Cs and CO codeposition. Onto this (2×2)–O overlayer we adsorb $^1/_4$ ML Cs, which results in a (2×2)–O + Cs structure on Ru(0001). It should be noted that the (2×2)–O + Cs surface is (meta)stable up to 700 K and can only be prepared, when oxygen is adsorbed first. The atomic geometry of the (2×2)–O + Cs structure is shown in Fig. 29 [112]. Cesium sits in on-top position, while oxygen stays in the *hcp* threefold hollow position. The O–Ru bond length is slightly longer than on clean Ru(0001): While on the clean Ru(0001) surface the O–Ru bond length amounts to 2.03 Å, the O–Ru bond length in the (2×2)–O + Cs overlayer is about 2.06 Å. Connecting the longer Ru–O bond length with a weaker bond strength of oxygen to the substrate one might speculate that an impinging CO molecule can better recombine with such an O species to form CO_2 than with O on the clean Ru(0001) surface. For impinging CO molecules this bin-

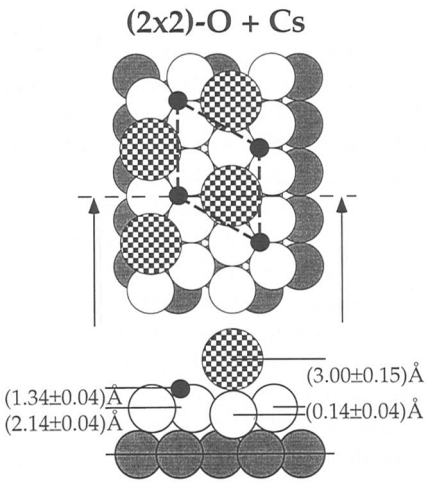

Fig. 29. The atomic geometry of Ru(0001)–(2×2)–O–Cs. Cs atoms sit in on-top positions, while oxygen atoms reside in hcp sites. Due to Cs adsorption the Ru–O bond weakens as indicated by the change in the Ru–O bond length from 2.03 Å (clean Ru(0001)) to 2.06 Å.

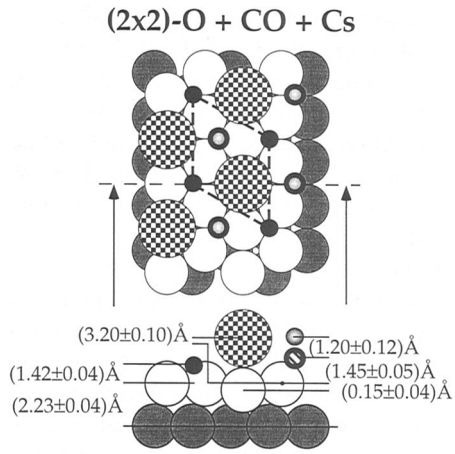

Fig. 30. The atomic geometry of the ternary phase Ru(0001)–(2×2)–O–Cs–CO. The O–Ru bond weakens even further upon CO coadsorption. The O-Ru bond length is 2.13 Å compared to (2.03 Å (clean Ru(0001) and 2.06 Å (Ru(0001)–(2×2)–O–Cs).

ary (2×2)–Cs + O overlayer offers two essentially different adsorption sites. In one adsorption site, CO molecules can bind directly to the Ru(0001) substrate and are attached to three Cs atoms. The other adsorption site would create a configuration where CO sits directly above an oxygen atom surrounded by three Cs atoms. This latter configuration would mimic an 'reaction intermediate' for the actual oxidation reaction since the O–CO complex has already the linear configuration of CO_2. A recent LEED study disclosed that an ordered ternary Cs + CO + O phase with (2×2) symmetry can indeed be prepared and that the CO molecules are sitting exclusively in those sites where no O atom is underneath. The structural characteristics of this system are summarized in Fig. 30. The O–Ru layer spacing with 1.45 Å is substantially larger than on the clean Ru(0001) surface resulting in a O–Ru bonding of 2.13 Å which is also markedly longer than 2.03 Å as found on the clean Ru(0001). A second point of interest is that the C–O bond length turned out to be 1.22 Å, i.e. the C–O bond is elongated by 0.09 Å with respect to C–O on the clean Ru(0001) surface. Both changes in bond lengths are consistent with an enhanced activity of the Cs + O + CO surface to form CO_2.

3.8 Beyond the molecular chemisorption of CO on transition metal surfaces

In this section we are concentrating on the local adsorption geometries of molecules which are bigger than CO and NO, such as benzene (pure and with electronegative coadsorbates) ethylene, and ethylidyene. All of these systems have been successfully analyzed by LEED. The study of the coadsorption of benzene C_6H_6 with electronegative molecules and atoms started with the intention to explore the atomic geometry of pure benzene layers. It was recognized on various transition metal surfaces that adsorption of pure benzene does not lead to ordering, while the addition of CO does actuate the formation of stable ordered superlattices of benzene. Adsorbed benzene is regarded as a prototypical adsorption system of organic molecules, since it is quite resistant against electron

bombardment and therefore particularly applicable for LEED. Accordingly this specific molecule has received much attention over the past 15 years in surface science applying the host of surface sensitive techniques.

The internal bonding of benzene is described within the extended Hückel theory. Carbon hybridizes in a sp^2 configuration forming a σ-bond to the attached H atom and two σ-bonds to the neighboring C atoms. The remaining half-filled p_z orbitals of carbon (z is defined to be perpendicular to the plane defined by the 6 C atoms in the benzene molecule) delocalizes into a π-system, which makes the bond order between the C atoms homogeneously to be 1.5. Adopted from coordination chemistry, the bonding of benzene to transition metal surfaces can be understood by the d-π interaction. The benzene-metal bonding proceeds via the system of delocalized p_z-electrons of benzene by interacting with (and donating electron density to) the d-bands of the substrate. In doing so the benzene molecule may loose partly its aromatic character, i.e., the delocalized character of the π-system diminishes and the consecutive C–C bonds have bond orders alternating now from 1 to 2. The C–C bond lengths should therefore be alternating between short and long. This kind of modification of the benzene molecule is called Kekulé distortion. One could anticipate to identify this chemisorption-induced distortions of the benzene molecule with surface crystallographic methods.

Spectroscopic and crystallographic investigations agree that the benzene molecule lies flat on close-packed transition metal surfaces [113, 114]. There is experimental evidence that the internal benzene structure varies from almost undistorted configuration (C_{6v} symmetry) to distorted configurations with C_{3v} symmetry. Spectroscopic studies, such as HREELS and ARUPS suggest essentially undistorted benzene molecules on close-packed transition metal surfaces [115–118]. Structural results of the benzene overlayers on *fcc*(111) and *hcp*(0001) surfaces are compiled in Table 4 and the possible high-symmetry adsorption sites for benzene molecules are illustrated in Fig. 31. Frequently, the adsorption of benzene molecules has been reported to be centered above the threefold coordinated sites although for some systems also the bridge site has been identified.

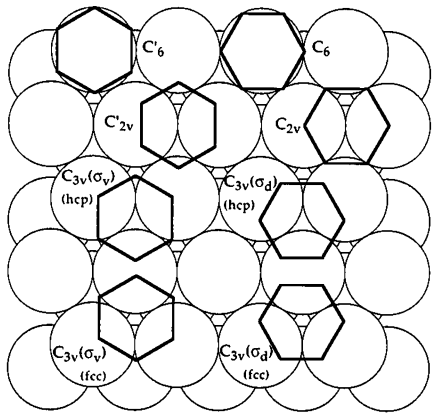

Fig. 31. Possible adsorption sites of benzene C_6H_6 on (111) surfaces of transition metal surfaces.

The system benzene on Ni(111) reveals a quite interesting feature in that the adsorption site changes from bridge to hcp sites and the azimuthal orientation of the molecule changes by 30° [119] when increasing the coverage from 0.10 to 0.14 [120]; the latter adsorption site was also identified with LEED [121]. The change in adsorption site was attributed to a steric effect by using the van der Waals radius of benzene. Benzene on Ni(111) is rather planar which is indicative of a smaller loss of molecular π-character. This is also in line with the quite small value of $\Delta\Phi$ of benzene on Ni(111), which implies a smaller net π transfer to the surface. The apparent alternation of C–C bond lengths (1.43 ± 0.15 Å and 1.55 ± 0.15 Å) is at the limits of the LEED structural analysis, although this Kekulé distortion would be in agreement with spectroscopic observations of C_{3v} symmetry for the adsorption complex [119].

In a diffuse LEED study of the disordered C_6H_6 overlayer on Pt(111) [122], the molecules were found to be centered over bridge sites. A large inverted boat-like distortion was found to occur with C–C bond lengths of

Table 4. Adsorption geometries of benzene, indicating the average carbon ring radius, the C–C bond lengths, metal-carbon distances, and the adsorption sites of C_6H_6.

Adsorption system [reference]	C_6 radius	D(C–C)/Å	d(M–C)/Å	adsite
Pd(111)–(3 × 3)–C_6H_6 + 2CO [126]	1.39 Å	1.40 ± 0.15	2.15 ± 0.05	*fcc*
		1.40 ± 0.15		$C_{3v}(\sigma_d)$
Rh(111)–(3 × 3)–C_6H_6 + 2CO [126]	1.44 Å	1.50 ± 0.15	2.07 ± 0.05	*hcp*
		1.37 ± 0.15		$C_{3v}(\sigma_d)$
Rh(111)–c(2 $\sqrt{3}$ × 4) rect–C_6H_6 + CO [125]	1.65 Å	1.81 ± 0.15	2.35 ± 0.05	*hcp*
		1.33 ± 0.15		$C_{3v}(\sigma_d)$
Pt(111)–(2 $\sqrt{3}$ × 4) rect–2C_6H_6 + 4CO [122, 125]	1.72 Å	1.76 ± 0.15	2.25 ± 0.05	bridge
		1.65 ± 0.15		C_{2v}
Ru(0001)–(3 × 3)–C_6H_6 + 2O [133]	1.39 Å	1.38 ± 0.08	2.22 ± 0.10	*hcp*
		1.40 ± 0.08		$C_{3v}(\sigma_v)$
Ru(0001)–(3 × 3)–C_6H_6 + 2NO [133]	1.32 Å	1.32 ± 0.11	2.23 ± 0.15	*hcp*
	1.44 Å	1.44 ± 0.11		$C_{3v}(\sigma_d)$
Ru(0001)–($\sqrt{7}$ × $\sqrt{7}$) R19.2°–C_6H_6 [124]	1.43 Å	1.41 ± 0.10	2.17 ± 0.05	*hcp*
		1.46 ± 0.10		$C_{3v}(\sigma_v)$
Ni(111)–C_6H_6 diffuse, $\theta = 0.10$ [120]	1.43 Å	1.40 ± 0.10	1.91 ± 0.07	bridge
		1.44 ± 0.10		C_{2v}
Ni(111)–($\sqrt{7}$ × $\sqrt{7}$) R19.2°–C_6H_6 [120, 121]	1.43 Å	1.40 ± 0.10	1.92 ± 0.05	*hcp*
		1.46 ± 0.10		$C_{3v}(\sigma_d)$

1.45 ± 0.10 Å and 1.63 ± 0.10Å. These distortions conflict with a previous NEXAFS study, which indicated equal bond lengths of 1.40 ± 0.02 Å [122, 123]. A C–C bond length of 1.63 Å is not very realistic since the C–C single bond length in organic molecules is about 1.54 Å.

On Ru(0001), C_6H_6 was found to be adsorbed on hcp sites in $C_3(\sigma_v)$ orientation, with only small distortions from the free benzene molecule [124]. The orientation of the benzene molecules on Ru(0001) is $C_{3v}(\sigma_v)$ while on Ni(111) the bond orientation is $C_{3v}(\sigma_d)$ [121]. The C–C bond lengths alternates between 1.45 Å and 1.41 Å within the adsorbed molecule. Since Ru has a high density of empty states close to the Fermi level due to its electron structure ($4d^6$), one would expect the strongest effect on the internal benzene structure among the 4*d* metals for ruthenium. Therefore Stellwag and coworkers interpreted the distortions found for Ru(0001) as an upper limit for distortions to be expected on other 4*d* metal surfaces. The found crown-like distortion of benzene on Ru(0001) was explained in terms of a loss of molecular π character, by π transfer to the surface, thus becoming closer to the configuration of cyclohexane.

Next we will be discussing the local adsorption geometry of benzene in the presence of coadsorbing electronegative molecules and atoms such as CO, NO, and O. Since the benzene molecule acts as a moderate donor, the addition of atoms and molecules serving as electron acceptors are able to stabilize and to order benzene overlayers.

By coadsorbing CO the benzene molecule rotates by 30° as found with Pt(111) [125]. In the (3×3)-benzene + NO overlayer on Ni(111) the benzene molecules are azimuthally reoriented due to minimizing the repulsive interactions in the densely packed overlayer as shown by AR-UPS [119]. For $CO + C_6H_6$ on Pt(111), benzene molecules are centered above the bridge site as in the pure phase. The C–C bond length within the molecule was found to be 1.65 ± 0.15 Å and 1.76 ± 0.15 Å. Both values seem again to be too large to be reasonable if compared to the C–C single bond length of 1.54 Å.

On Pd(111) and Rh(111) the geometric structures of benzene + CO overlayers have been determined by LEED [126]. On Pd(111), the benzene and CO molecules were all found to be centered on fcc-hollow sites, while on Rh(111) they were all centered on hcp-hollow sites. There are no chemisorption induced Kekulé distortions detected on the Pd(111) surface, while on Rh(111) small (1.37 ± 0.15 Å) and long (1.50 ± 0.15 Å) C–C bonds were found. The C–Pd bond length is larger than the C–Rh bond length and the distortions induced by benzene adsorption are smaller on Pd(111) than on Rh(111). Both findings suggest a weaker benzene-Pd than benzene-Rh bond. This structural differences may be correlated with reactive properties. Acetylene reacts on Pd(111) to produce benzene [127, 128] while Rh(111) does not. One may argue [126] that the less strongly bonded and less distorted benzene on Pd(111) can desorb intact, while the same species on Rh(111) would more likely dissociate. The observed relaxations of the metal surfaces have been explained in terms of the charge transfer from CO to benzene. Charge donation to the substrate induces an outward expansion of the substrate, while a charge acceptance from the substrate might induce an inward contraction of the substrate. Adsorbate induced reconstructions on the Ru(0001) surface were discussed recently by Menzel [129] who showed that such a simple correlation is questionable.

The adsorption site of C_6H_6 changes from bridge to hollow site on Rh(111) upon coadsorption of CO, presumably for steric reasons [126]. And conversely, benzene changes the adsorption site of CO towards higher coordination on Rh(111) similar to the case of K + CO on Rh(111) [130]. The reason might be that the high coordination site allows the CO molecules to easier accept electron density from the substrate [107]. This view is supported by the fact that C–O bond length elongates on coadsorption with hydrocarbons such as benzene. For Pd(111) and Pt(111) CO adsorbs already in hollow sites on the clean surface [131, 132], so that upon coadsorption of benzene this site will be maintained and be even stabilized. According to a LEED study, the coadsorbed C_6H_6 molecule suffers from a strong Kekulé distortion (which might be even present without CO) which depends on the C_6H_6:CO stoichiometry at the surface. For a ratio of 1:2 the short/long C–C bonds are 1.46 Å/1.58 Å and for a 1:1 mix it is 1.33 Å/1.81 Å. Here again the latter value of the long bond seemed to be too long, also if one compares this value with those found in organometallic complexes.

The coadsorption of O and NO with benzene on Ru(0001) [133] indicated that O coadsorption does not change the internal structure of the benzene within the error bars, while NO coadsorption does modify the benzene molecule significantly. The C–C bond lengths are 1.32 ± 0.11 Å and 1.44 ± 0.11 Å in the presence of NO which signifies Kekulé distortions of the benzene molecule (C–C single bond: 1.51 Å, C–C double bond: 1.31 Å). Due to steric repulsion between the H atom of C_6H_6 and the NO molecule, the benzene molecule rotates by about 20° to avoid overlapping of the van der Waals radii.

From thermal desorption spectra of benzene it is clear that coadsorption of O and NO stabilizes the benzene overlayer. Therefore it is somewhat surprising that the benzene-substrate distance increases for both coadsorbates by about 3%. This effect has already been recognized in the AM + CO coadsorption system and there it is explained by the electrostatic interaction between electronegative and electropositive species. One might expect the same effect to be operative here.

An organic molecular fragment whose local structure was determined by LEED is ethylidyne C_2H_3. Ethylidyne is produced by thermal decomposition of ethylene C_2H_4 and has been shown to adsorb upright in fcc and hcp threefold hollow sites, on Pt(111) [134] and Rh(111) [135], respectively (cf. Fig. 32). On both surfaces the adsorption is accompanied by relatively strong displacements of the substrate atoms. On Pt(111) the three Pt atoms nearest to the adsorbate site move upward in the first layer and downward in the second layer, i.e., a local expansion of the metal layer separation underneath the adsorbate occurs. On Rh(111) both the three Rh atoms attached to C_2H_3 and the second layer Rh atom directly underneath are moving outwards. While the three C_2H_3 attached sub-

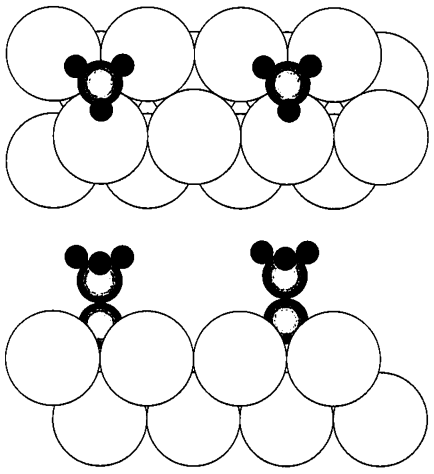

Fig. 32. Hollow site adsorption of ethylidyne C_2H_3 on Pt(111) and Rh(111).

strate atoms expand laterally for Rh(111), they contract for Pt(111). One might speculate that in this way C_2H_3 can better form a bond to the second layer Rh atom. In essence, carbon seems to like higher coordination on Rh(111) than on Pt(111) which is perhaps related to the fact that rhodium forms a carbide as opposed to platinum which does not. On Pt(111), ethylidyne is executing a wagging vibration as identified with PhD for C_2H_3 on Ni(111) [136].

Last but not least the adsorption of acetylene C_2H_2 on Pd(111) was determined by using quantitative LEED and photoelectron diffraction [137]. This particular system has attracted much attention because of its ability to form a benzene molecule by cycloaddition of three acetylene molecules [127, 128, 138]. The C_2H_2 molecules form a (2×2) structure on Pd(111) and the carbon atoms are located almost over bridge sites with a C–C bond length of 1.34 ± 0.10 Å. The center of C_2H_2 is positioned over the hcp hollow site, as indicated in Fig. 33. The found C–C bond length on Pd(111) compared to the gas phase (1.25 Å) indicates a moderate interaction of acetylene with Pd(111), which is strong enough to allow for the trimerization reaction before desorption but the bonding is weak enough to prevent decomposition of C_2H_2. Both features are important to render Pd(111) an exceptionally good catalyst for producing benzene.

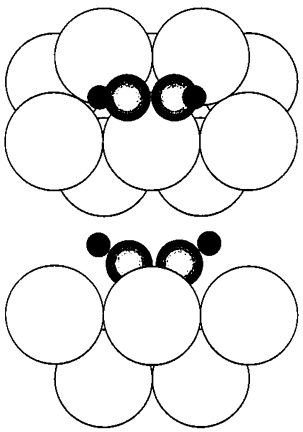

Fig. 33. Schematic diagram of the local geometry for C_2H_2 in an *hcp* hollow site.

3.9 Concluding remarks

The Cs + CO and O + CO systems are clear-cut examples for the intimate relation between the electronic modifications at a surface and how the adsorption geometry changes. Cs coadsorption strengthens the back bonding of CO to the metal substrate and forces CO to reside in high-coordination sites. By contrast, the addition of oxygen weakens the CO back bonding to the metal substrate so that the CO adsorption sites may change to on-top sites, as found for instance with CO on Ni(111).

We have demonstrated that quantitative LEED provides important information on the atomic geometry of complex coadsorbate systems. This might be relevant for the study of surface reactions as exemplified with the CO oxidation reaction and the Cs promoted CO oxidation over Ru(0001). We further showed that the adsorption geometries of molecules bigger than CO can be determined by using quantitative LEED.

IV. Structure of incommensurate overlayers

4.1 Introduction

The subject of this chapter will be the LEED analysis of incommensurate structures and coherent overlayers. Coherent overlayers can be described by a large surface unit cell with the adatoms being located in inequivalent adsorption sites. For incommensurate structures, the translational symmetry of the deposit + substrate system is lost, and it is not possible to define a surface unit cell of finite size. However, because of the limited resolution of a LEED apparatus, a coincidence lattice with a large unit cell cannot be distinguished from a true incommensurate structure. Therefore, any incommensurate structure can, for a LEED structure analysis, be modeled by a coincidence lattice. The analysis of such structures is, however, quite time consuming and cumbersome because of the size of the unit cell so that it is not surprising that the LEED structure determination of incommensurate structures is still in the very beginning. Recently, efficient approximation schemes have been developed to calculate LEED IV curves for evenly dispersed incommensurate adlayers with small modulations [139]. They lead to a considerable reduction in computing time and will be discussed further below.

The structure of incommensurate adsorbate layers is of interest especially for the study of the initial growth of ultra thin films. In the case of layer by layer growth, the structure of a growing film is accessible by LEED if the adsorbate film exhibits sufficient long-range order. A prerequisite for long-range order of the deposit films is that the deposit grows epitaxially, i.e., that the orientations of the deposit and the substrate are related to each other so that a crystal plane of the deposit is parallel to the crystal plane that forms the substrate surface, with particular directions in the two planes being parallel [140]. Otherwise, one would expect the formation of a polycrystalline film with many inequivalent domains instead of the growth of a well ordered adsorbate film.

The application of quantitative LEED to the study of thin film growth goes back to the pioneering studies performed in Jona's group, focusing mainly on pseudomorphic growth [140]. In this case, below a critical thickness the overlayer is constrained to match the substrate lattice. Pseudomorphic systems are characterized by the persistence of a (1 × 1) LEED pattern upon evaporation of the first adsorbate layers. In the submonolayer range, the LEED IV curves of the (1 × 1) beams begin to change if compared with the data of the clean substrate. When the first monolayer is completed, the IV data are characteristic of an ordered overlayer structure. LEED IV calculations can be easily performed due to the small size of the (1 × 1) unit cell, in order to determine the atomic coordinates of the deposit-substrate system. One of the first full metal monolayers on metals investigated by quantitative LEED was a Cd film grown pseudomorphically on Ti(0001) [141].

With continuing deposition, for the case of layer-by layer growth, the LEED IV data change gradually with the number of layers. For adsorbate films of more than about 4...8 layers, the IV curves become stable, and the influence of the substrate on the IV data is negligible due to the small inelastic mean free path of the electrons. Under these conditions it is possible to calculate LEED IV curves using the (1 × 1) unit cell of the overlayer structure. In doing so, several ordered grown metal films have been quantitatively analyzed by LEED. For the pseudomorphically grown four-layer Cd film on Ti(0001), for example, the IV curves turned out to be very similar to that of a Cd(0001) crystal [141]. A comprehensive overview of structural and elastic properties of pseudomorphically grown metal films can be found in Ref. 140.

Recently, the structure of ultra thin magnetic films was extensively investigated by LEED. The investigation of those systems – Fe on Cu [142], Co on Cu [143], and Ni on Cu [144] – was spurred by their interesting magnetic properties and by the prospect to stabilize configurations which are not stable in the bulk (such as fcc iron on Cu(100) at room temperature [142]).

For pseudomorphic systems, in many cases order becomes worse with progressing film growth. Since the lattice constants of substrate and adsorbate do not match perfectly, the pseudomorphic growth is accompanied by a substrate-induced strain within the adlayers. If the film exceeds a certain thickness, the substrate-induced strain is relieved by the formation of misfit dislocations, thereby destroying the long-range order.

Pseudomorphic growth can only occur if the lattice mismatch is not too large, say, less than about 10%. The lattice mismatch is defined as the ratio $(d_{ads} - d_{sub}) \times 100\%)$, d_{sub}, with d_{ads} and d_{sub} being the lattice constants of the adsorbate lattice and the substrate lattice constant, respectively. Layer by layer growth has, however, also been observed with systems with a larger lattice mismatch, such as Ru(0001)–Mg (lattice mismatch 17%) [145, 146]. For such systems, the lateral interaction between the adsorbed atoms is dominating over the corrugation potential imposed by the underlying substrate. Under these conditions, the epitaxial growth of films may take place in an incommensurate manner; i.e. the metal film has its own periodicity which is not related to the substrate periodicity. As a result, the adsorbate films are almost unstrained and may exhibit good long-range order also in the multilayer range.

With the Ru(0001)–Mg system, pseudomorphic growth is not observed. Rather, in the submonolayer range, incommensurate structures form [145, 146]. The saturation of the first monolayer coincides with a (7 × 7) LEED structure with dominant spots at ((6/7*h*, 6/7*k*) *h*, *k* integers) positions, which is stable also upon progressing uptake of Mg. LEED analyses of the structures of 1–4 monolayer films show that Mg grows in its bulk like *hcp* configuration right away from the beginning [145]. By further Mg deposition, it is possible to grow a very well ordered Mg film on the Ru(0001) substrate. Eventually, the IV curves of the dominant spots of the Mg-induced (7 × 7) structure become stable while all other spots, including those of the Ru substrate lattice, vanish. A LEED analysis revealed that the structure of the thick Mg film is identical to bulk Mg [146].

In the following, LEED structural analyses of incommensurate structures and coincidence layers will be discussed in more detail. It is not the aim of this chapter to give a complete overview of all structure analyses of such systems, but we will rather focus on illustrative examples and address the question which parameters can be determined with confidence for incommensurate structures in a LEED analysis. First of all, the structures of ultra thin layers of Mg on Ru(0001) will be discussed, and an approximation scheme for calculating the IV curves of dominant beams in incommensurate structures will be introduced: The "mirror approximation" [145] (section 4.2). Section 4.3 deals with alkali metal films, as exemplified with the system Ru(0001)–Li [147]. In contrast to Mg on Ru(0001), where both the substrate and the adsorbate layers are hcp materials, close packed surfaces of all alkali metals except Li do not possess the threefold rotational symmetry of the Ru(0001) surface since they are *bcc* metals. For Li, however, also fcc and hcp modifications exist at low temperatures and high pressures [148]. As evidenced by LEED, Li builds up an fcc(111) like structure on Ru(0001) which is strongly distorted by the substrate [147].

For the Ru(0001)–Mg and Ru(0001)–Li systems mentioned above, the LEED data provide information mainly about interlayer distances, thickness, and stacking sequences of the thin films while modulations within the adlayers, i.e. deviations of the adatoms from their positions in an evenly dispersed, flat adlayer, have not been considered. Due to the large unit cell, the determination of such modulation amplitudes by LEED is a computer demanding task. Recently, however, an efficient approximation scheme for the calculation of LEED IV curves of modulated films was developed by Grünberg and Moritz and applied to a structure determination of the Cu(100)–c(2 × 10)–Ag structure [139]. Section 4.4 will briefly discuss the determination of modulation amplitudes within the incommensurate overlayers by LEED which also close the section about incommensurate structures.

4.2 Incommensurate structures of Mg on Ru(0001)

The incommensurate overlayer structures of Mg on Ru(0001) were subject of detailed LEED structural analyses, both in the submonolayer and the multilayer regime [145, 146]. In the submonolayer range, Mg forms islands which coalesce with increasing coverage until a uniform and homogeneous Mg overlayer is created. The unit cell of this overlayer can be approximated by a (5 × 5) cell with dominating (*h*4/5, *k*4/5) superstructure spots. All other superstructure spots are weak, consistent with a evenly dispersed Mg layer with only small modulations. Note that without modulations, other superstructure spots than (*h*4/5, *k*4/5) are absent in single scattering and are present due only to multiple scattering. Assuming a homogeneous Mg film, the (5 × 5) surface structure consists of 16 Mg atoms in various sites over 25 Ru atoms within the first substrate layer (Fig. 34a).

Further uptake of Mg leads to a continuous compression of the (5 × 5) cell into a quasi (7 × 7) phase. With a homogeneous Mg layer, one obtains 36 Mg atoms adsorbed in inequivalent sites over 49 Ru atoms in the unit cell (Fig. 34b). The (7 × 7) structure corresponds to the completion of the first monolayer with a Mg coverage of 0.75.

One can extract information on the evolution of the structure in the compression phase already by comparing the experimental IV curves of measured beams at the beginning and at completion of the compression phase, i.e. in the (5 × 5)- and (7 × 7) structure. As shown in Fig. 35, these IV curves are essentially identical. This similarity gives evidence that the IV curves of those beams are almost not affected by the adsorption sites occupied by the Mg atoms, since during the compression phase the adsites of the Mg atoms change certainly while the IV curves do not. The insensitivity of LEED IV curves to the adsorption site in incommensurate overlayers is plausible because the scattering process corresponds to some kind of averaging over local Mg adgeometries in different sites which simultaneously contribute to the total scattering amplitude.

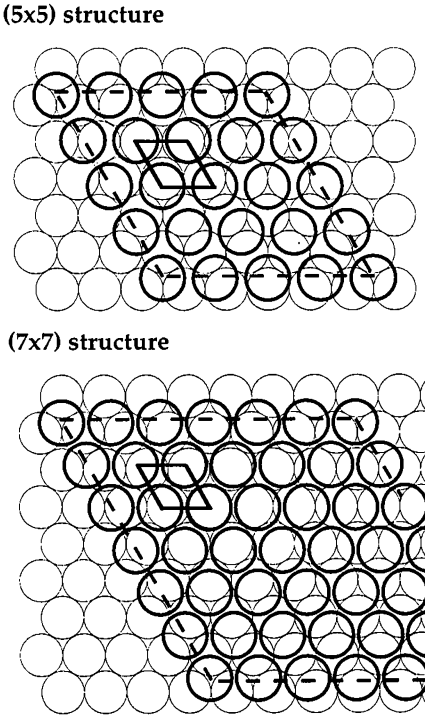

Fig. 34. Structures of Ru(0001)–(5 × 5)–Mg (top) and Ru(0001)–(7 × 7)–Mg (bottom) with an evenly dispersed Mg layer. The (5 × 5) and (7 × 7) unit cells (dashed lines), as well as the unit cells of the Mg layer (solid lines) are shown.

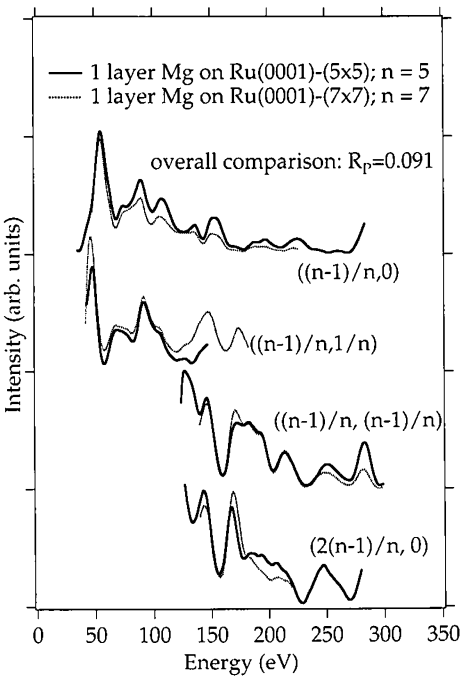

Fig. 35. Comparison of experimental IV curves at the beginning and after the completion of the compression phase of Mg on Ru(0001). The striking similarity indicates that the structural features, especially the average Ru–Mg interlayer spacing, are the same throughout the compression phase.

From the dominance of the (4/5*h*, 4/5*k*) and (6/7*h*, 6/7*k*) spots lateral and vertical modulations of the Mg adlayer are expected to be small. Therefore the most important parameter affecting the LEED IV curves of these beams is the average layer spacing between the Mg layer and the Ru substrate. As evidenced by the close similarity of the corresponding IV curves, this parameter is identical in the (5 × 5) and (7 × 7) phase.

Furthermore, the similarity of the measured IV curves demonstrates that the (7 × 7) structure can be modeled by using the smaller (5 × 5) unit cell. Calculations of LEED IV curves using a (5 × 5) unit cell and comparison with experiment yield a value of (2.32 ± 0.04) Å for the Mg-Ru interlayer spacing both in the (5 × 5) and the (7 × 7) structure. The Mg layer is almost evenly dispersed, with a buckling <0.15 Å and lateral deviations smaller than 0.3 Å (Fig. 36).

After completion of the first Mg monolayer, the (7 × 7) symmetry persists upon deposition of further Mg layers. Model calculations for a 2 layer film indicated, however, that the approximation of using a (5 × 5) unit cell instead of a (7 × 7) unit cell breaks down in the calculation of LEED IV curves of the (7 × 7) phase. This is plausible because in the multilayer regime multiple scattering between different Mg layers becomes important, and

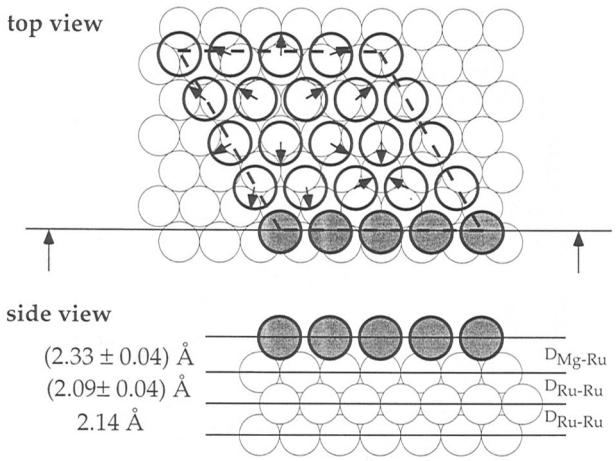

Fig. 36. Structural parameters for the optimum geometry of the submonolayer film of Mg on Ru(0001); the parameters found in the structural analysis are the same for the (5 × 5)-structure (beginning of the compression phase) and the (7 × 7) structure (completion of the compression phase).

hence the IV curves are stronger influenced by details of the Mg structure, such as for example the Mg interatomic spacings. In order to avoid a time consuming calculation with 36 atoms in each Mg layer, an efficient approximation scheme was introduced: Due to the proximity of the dominant (7 × 7) spots to the integer order beams, a mixing between the dominant Mg and (1 × 1) substrate beams is small for all but for the (0,0) beam because either scattering paths with large momentum transfer at the bulk interface are involved, or interlayer scattering between bulk and overlayer with at least one backscattering event at the overlayer is required (see Fig. 37). Thus the nondiagonal elements of the bulk matrix may be neglected for the computation of the dominant Mg beams. In addition, Mg occupies many different adsites on the Ru substrate. Therefore, only the bulk reflection matrix averaged over these local registries participates in the scattering between the Mg films and the substrate. Again, this averaging process causes the diagonal elements of the bulk scattering matrix to survive while off-diagonal bulk matrix elements are averaged out. Altogether, the substrate acts more like a mirror than a template with atomic structure, i.e., all beams coming from the Mg film are just backscattered in specular direction.

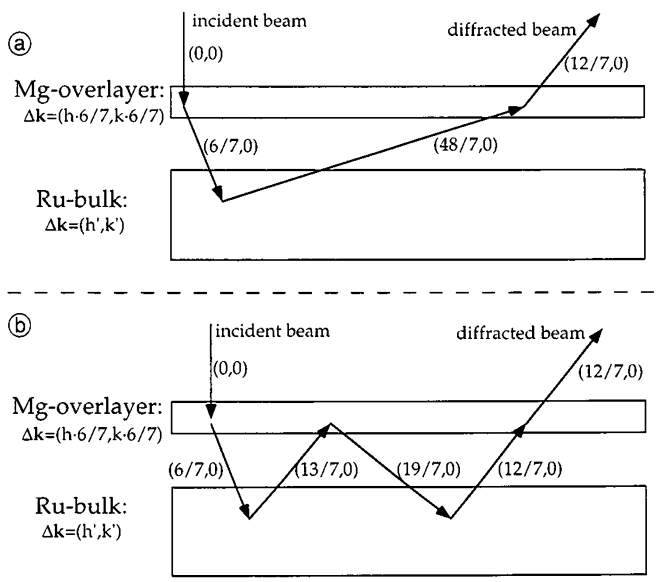

Fig. 37. Two types of scattering paths where nondiagonal elements of the bulk scattering matrix are involved; both types give only a small contribution to the total scattering amplitude: Scattering event (**a**) is negligible since a large momentum transfer imposed by the bulk is involved. (**b**) This type of scattering path requires three backscattering events (one at the overlayer, two at the substrate) and can therefore be neglected.

Based on this knowledge, an approximation scheme, the so called "mirror approximation", was developed: The evenly dispersed Mg overlayer is considered as a (7/6 × 7/6) structure above the (1 × 1) substrate, and only the diagonal elements of the Ru bulk matrix were used. The Ru bulk scattering matrix has to be calculated for the (1 × 1) geometry (especially the lattice sum) and then projected onto those beams which are associated with a (7/6 × 7/6) cell. The computational effort for this approximation is the same as for calculations of a (1 × 1) structure and hence tremendously reduced if compared with the full (7 × 7) unit cell.

With this approximation at hand, the geometry of 2–4 monolayer Mg films was determined. It turned out that the Mg film grows right from the beginning in a hcp stacking sequence. In Fig. 38, the geometry of the two layer Mg film is shown. The topmost layer spacing of (2.73 ± 0.03) Å is expanded compared to the bulk value (2.60 Å). For the thicker films, the optimization of interlayer spacings revealed that the expansion of the topmost Mg–Mg layer spacing of (2.68 ± 0.04) Å is less pronounced.

The good long-range order of the Mg film persists also upon further Mg deposition. A LEED analysis of a 9 monolayer Mg film grown on Ru(0001) revealed bulk like interlayer distances except for a slight expansion of the topmost spacing which turned out to be 2.64 Å. This result is consistent with a LEED analysis of a single crystal Mg(0001) surface [149]. The structure analysis of the thick Mg film on Ru(0001) was simplified by the fact that the influence of the substrate on the IV curves was negligible owing to the small elastic mean free path of the electrons. Hence the calculations could be performed with the (1 × 1) unit cell of the Mg film.

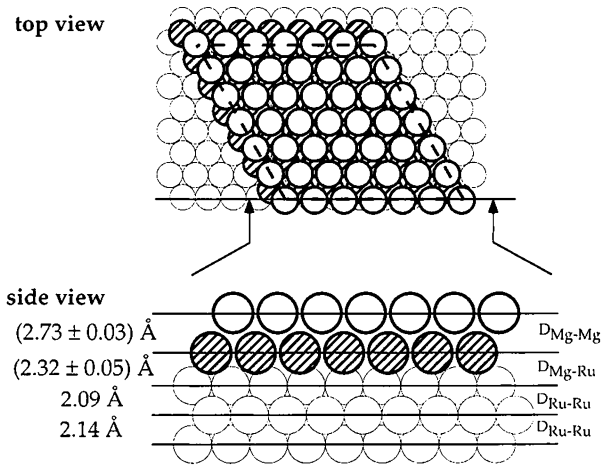

Fig. 38. Optimum geometry determined for the two layer Mg film on Ru(0001).

The LEED analyses of thin Mg films on Ru(0001) demonstrated that the structure is identical to that of a thick Mg film or a Mg bulk crystal. Even the expansion of the topmost layer spacing, compared to its bulk value, is already observed with the 2 ... 4 layer films. As the valence shell of Mg ($3s^2$) is full, this expansion can be traced back to a $s-p$ hybridization necessary to form a bonding between the Mg atoms [150]. The hybridization costs a substantial amount of energy (about 2.7 eV) which is compensated for by the energy gain due to the bonding between the Mg atoms. At the surface, this gain is smaller since the coordination number of Mg atoms in the topmost layer is reduced, compared to bulk Mg. The total energy of the surface can therefore be minimized by reducing the hybridization, which, in turn, causes the observed expansion of the topmost Mg–Mg interlayer spacing.

4.3 Incommensurate structures of alkali metals: Li on Ru(0001)

The structures of alkali metal atoms adsorbed on metal surfaces have been the subject of many investigations, also because alkali metals with only one valence electron are regarded as simple model systems to study the genuine adsorption process [151]. While most structural analyses were performed for commensurate overlayers of alkali atoms, only a few studies were also devoted to the structure of incommensurate overlayers and thin films, although the formation of incommensurate structures of alkali metals on metal substrates is frequently observed [152].

Upon exposure of alkali atoms (Li, Na, K, Rb, Cs) to a Ru(0001) surface, commensurate (2 × 2) and ($\sqrt{3} \times \sqrt{3}$) R30° structures form at coverages of $\theta = 0.25$ and $\theta = 0.33$. The coverage θ is defined as the ratio of the atomic density of the adsorbate layer and the atomic density of the topmost substrate layer. Except for the (2 × 2)–Li phase, all other structures were analyzed by LEED [101]. In the ($\sqrt{3} \times \sqrt{3}$) R30° structure, alkali atoms reside in the threefold hcp site while threefold fcc sites are occupied in the (2 × 2) structure, except for Cs which sits in the onefold coordinated on top position. Near the completion of the first monolayer, incommensurate structures or coincidence layers were observed for Li, Na, and K.

One of those coincidence structures, the Ru(0001)–(3 × 3)–Na structure, has been subjected to a detailed LEED analysis [153]. The average Na-Ru spacing turned out to be 2.60 Å, with vertical modulations being smaller than 0.15 Å. As a result of the structure analysis, the Na atoms form an evenly dispersed adlayer and are adsorbed close to threefold hollow and bridge sites (Figs. 39a, b). A model with the Na atoms being located in highly symmetric on-top and threefold hollow sites (cf. Fig. 39c) could clearly be ruled out. An unambiguous determination of the surface structure was, however, not possible since the models shown in Fig. 39a and Fig. 39b give very similar r-factors. Furthermore, the sensitivity to lateral displacements of the Na atoms away from their positions in an evenly dispersed adlayer turned out to be quite low.

On Ru(0001) for coverages exceeding one monolayer, no LEED pattern with sharp spots could be observed for all alkali metals but Li. The absence of long-range order may be related to the threefold $p3m1$ symmetry of the Ru(0001) surface. Assuming that the alkali atoms form closed packed *bcc*(110) structures, the $p3m1$ symmetry of the Ru(0001) surface imposes the coexistence of different inequivalent rotational bcc(110) domains, thus preventing the growth of thick monocrystalline multilayer films.

Unlike the other alkali metals, Li multilayers on Ru(0001) reveal sufficient long-range order to produce LEED patterns with sharp spots. Compared to Na, K, Rb, and Cs, the bulk properties of Li are qualitatively different in that Li transforms below 70 K partly into *hcp*-like configuration [148]. At very low temperatures, x-ray diffraction experiments indicated that the structure in this phase is more complicated, with a ABCBCACAB stacking sequence [148c]. Applying stress, even a *fcc* configuration can be stabilized. Na, K, Rb, and Cs, on the other hand, exist only in the *bcc* configuration (with some exceptions for very low temperatures <10 K) [148a].

A sequence of Li-induced LEED patterns follows the completion of the first monolayer (Fig. 40, after Ref. [147]). Similarly to Mg, the Li film continuously compresses up to the completion of the first monolayer, as indicated by incommensurate structures with superstructure spots moving radially towards the substrate spots with increasing coverage (cf. Fig. 40a). The coverage was determined by integration of thermal desorption spectra, whereby the coverage in the ($\sqrt{3} \times \sqrt{3}$) R30° structure was assumed to be $\theta = 0.33$. At a Li coverage of $\theta = 0.64$, the incommensurate Li film can be modeled using a (5 × 5) unit cell with the 4/5(h, k) beams being dominant amongst the superstructure spots. This (5 × 5)–Li structure has

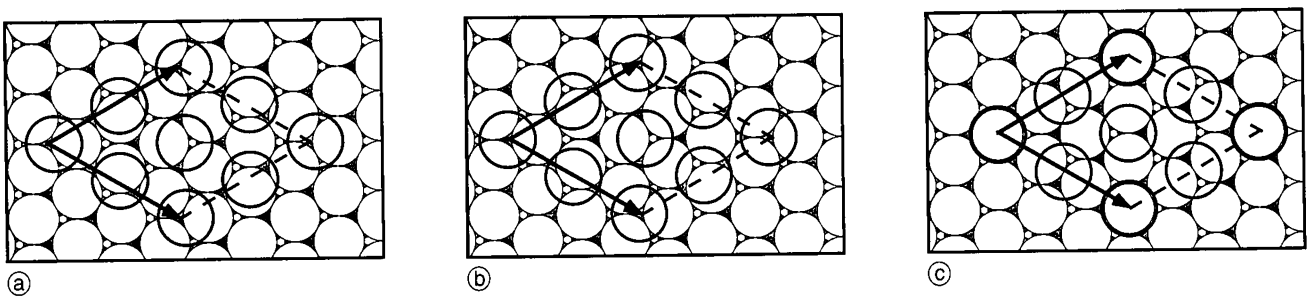

Fig. 39. Structural models tested for Ru(0001)-Na. The unit cell of the (3 × 3) coincidence layer is indicated. The models shown in (**a**) and (**b**) correspond to r-factor minima with very similar r-factors while the model depicted in (**c**), with Na atoms adsorbed in atop and bridge sites, can clearly be ruled out.

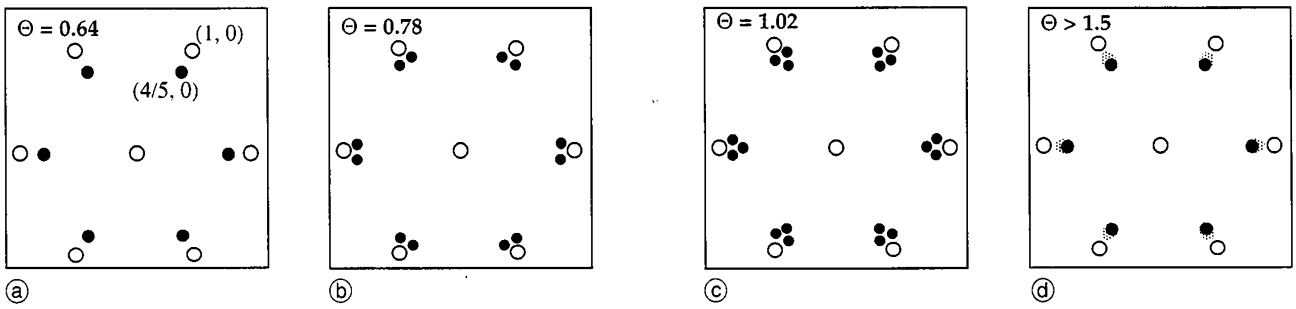

Fig. 40. Schematics of the LEED patterns observed for the Ru(0001)–Li system before and after completion of the first monolayer (after Ref. [121]). (**a**) compression phase observed in the submonolayer range (for coverages larger than 0.60). The adsorbate-induced spots (full circles) are moving towards the substrate spots (empty spots) with increasing coverage, thus indicating a continuous lateral compression of the adsorbate film. (**b**) Completion of the first monolayer: The adlayer is slightly rotated with respect to the high-symmetry axes of the Ru substrate. (**c**) At coverages above one monolayer, new adsorbate spots appear close to (5 × 5) positions. (**d**) These spots persist also for coverages in the multilayer range; for coverages above three monolayers, a broadening of the adsorbate-induced spots (as indicated by the dashed areas in the figure) indicates a worsening of the long-range order within the Li film.

been analyzed by LEED. Since IV curves of only the (4/5, 0) beam and its symmetrically equivalent spots could be measured, the only parameter which could be determined was the Ru–Li interlayer spacing; its value is (2.17 ± 0.10) Å.

The saturation of the first monolayer takes place at $\theta = 0.78$, corresponding to an average Li–Li distance of 3.06 Å; this value is close to the bulk value of 3.1 Å for the hcp configuration of bulk Li [148]. As indicated by the splitting of the superstructure spots in the respective LEED pattern (Fig. 40b), the Li monolayer is slightly rotated away from the high symmetry directions of the substrate. At coverages above one monolayer, superstructure spots appear close to the (4/5, 0) position (cf. Fig. 40c) and persist upon further Li exposure up to about 3 monolayers. The hexagonal symmetry of the pattern is consistent with the growth of hcp- or fcc like Li films.

LEED analyses of ordered structures with two and three monolayers revealed that Li builds up a fcc(111) like stacking sequence with interlayer distances of (2.35 ± 0.10) Å between the Li layers and (2.35 ± 0.10) Å between lithium and ruthenium (see Fig. 41). The in plane lattice constant of Li was determined from the positions of the Li-induced superstructure spots to be (3.34 ± 0.04) Å.

The 3-layer Li film is strongly distorted by the substrate as indicated by a smaller value for the Li–Li interlayer spacing (2.35 Å compared to 2.45 Å for the bulk fcc configuration) together with a larger in-plane lattice constant if compared with the pure *fcc*(111) Li structure (3.34 Å for the 3-layer film, compared to 3.10 Å for the bulk). This distortion may indicate an attractive interaction between the second Li layer and the substrate. Despite the large distortions, the atomic density within the 3 monolayer Li film on Ru(0001) of 0.044 atoms/Å^3 turns out to be quite similar with that in the *fcc* bulk phase (0.0467 atoms/Å^3).

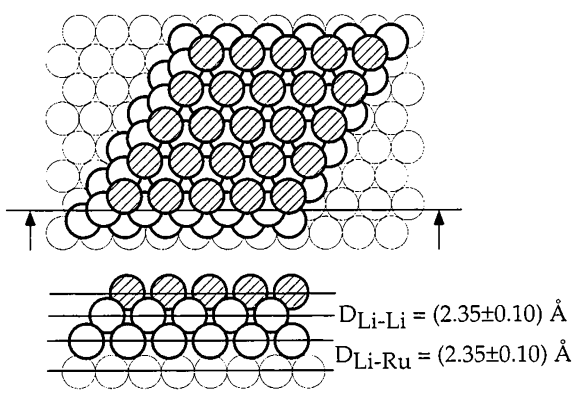

Fig. 41. Optimum geometry derived for the 3 layer Li film on Ru(0001); the film grows in an fcc stacking sequence.

Further uptake of Li beyond 3 monolayers leads to a considerable worsening of the long-range order (cf. Fig. 40d), in contrast to the Ru(0001)–Mg system discussed in the last section. While Mg on Ru(0001) builds up its bulk structure, the first Li adlayers grown on Ru(0001) are distorted compared to their volume structure and hence heavily strained. This strain is probably relieved by the formation of misfit dislocations if the film exceeds a 3 monolayer thickness, thus destroying the long-range order. This behavior is also known for pseudomorphic films grown on metal substrates.

A system where it was possible to grow a thick well ordered alkali metal film on a metal substrate, is Ni(100)–K [154, 155]. The surface of the Ni(100) crystal used for this study was slightly rippled, indicating the existence of steps that may break the fourfold orientational symmetry and permit growth of the K layer only in one orientation. The long-range order of the potassium film was sufficient to measure IV curves and determine the structure. It turned out that K forms a bcc(110) structure, with bulk like interlayer spacings except for the top layer. Within the top layer, a lateral relaxation of the K atoms was determined. Due to the thickness of the film, only the K atoms influence the IV curves, and the calculations could be carried out using the unit cell of the potassium film.

4.4 Modulations within thin films

The preceding sections mainly dealt with interlayer spacings and stacking sequences of incommensurate adlayers. The adsorbate layers were considered as being evenly dispersed, i.e., it was assumed that the individual substrate and adsorbate layers are periodic, although the translational symmetry of the adsorbate + substrate system is lost or reduced. A further level of sophistication is introduced

into the structural analysis if the translational symmetry of the individual adlayers is broken by allowing modulations within the adlayer films, i.e., deviations of the atoms away from their positions in an evenly dispersed adlayer.

Recently, progress has been made in calculating LEED IV curves for modulated, incommensurate structures. An efficient approximation scheme was developed by Grünberg and Moritz [139], which has some similarity to the widely used Tensor LEED method [156]. Thereby, the undistorted, evenly dispersed adlayer is used as "reference structure"; the full multiple scattering calculation is carried out only with the small unit cell of the undistorted adlayer, while modulations within the adsorbate films are treated by a perturbation method. Despite the small size of the unit cell, calculations using this approximation are still rather computing time consuming because many plane waves are required in order to couple the wave field of the adsorbate film properly with that of the substrate. Within the framework of the method (developed by Grünberg and Moritz) the number of plane waves is limited and reduced by employing the "beam set neglect" approximation which was developed first for the structural analysis of adsorbed large molecules [157].

The method was tested and applied for a structural analysis of the Cu(100)–c(2 × 10)–Ag coincidence phase [139]. It turned out that the Ag atoms occupy positions close to fourfold or bridge sites. Sine-like modulations were assumed, as shown in Fig. 42. As a result of the structure analysis, the modulation amplitude of the Ag film amounts to 0.2 Å, whereby atoms close to bridge sites are located about 0.2 Å above the atoms in fourfold hollow sites. A comparison with IV curves calculated fully dynamically revealed that the approximation described above is well applicable for modulation amplitudes of up to 0.3 Å. For amplitudes larger than 0.5 ... 0.7 Å, the influence of the lattice distortions on multiple scattering becomes large enough for the approximation to break down.

While the problem of calculating IV curves of modulated, incommensurate structures seems to be tractable, further investigations have to disclose how sensitive LEED data are to these parameters. With the Ru(0001)–Mg and Ru(0001)-Li systems treated in the last section, average interlayer spacings, registries, and the number of adsorbate layers could be determined with confidence, while a precise determination of modulations was hampered by the low sensitivity of the IV curves to vertical and lateral bucklings. At this point it is important to recall that the dominant spots observed in the incommensurate phases of Li and Mg on Ru(0001) belong to the reciprocal lattice of an evenly dispersed adlayer, and that modulations of the adlayer may have a similar effect on these particular spots as thermal disorder. Hence, the low sensitivity of the IV curves to modulations may be rationalized by the fact that LEED is in general less sensitive to that kind of "disorder" than to interlayer spacings or other structural parameters. It may be necessary to measure also IV curves of weaker spots being absent in the kinematic limit for an evenly dispersed overlayer, which may contain more information on the modulation amplitudes.

The determination of lateral modulation amplitudes may be simplified in those cases where the variation of the intensities of the LEED spots with the momentum transfer parallel to the surface, $k_{||}$, is strongly affected by modulations. An instructive example is provided by ultra thin 2 ... 4 layer *fcc* Fe films on Cu(001) which can be described by a (5 × 1) coincidence lattice [142]. The LEED pattern of this system exhibits a very characteristic feature: Among the observed spots, only the (1, $^1/_5$), (1, $^4/_5$), and (1, $^6/_5$) reflections have notable intensities while the intensities of all other Fe-induced spots are very weak in the whole energy range (cf. Fig. 43a). Sine like lateral modulations, as shown in Fig. 43b, can explain the pattern and the observed weakening of most of the superstructure spots. A fully dynamical structure analysis of a 4 layer Fe film confirmed this speculation [142]. Large deviations of several tenths of an Å from the positions in an unmodulated film in lateral (and also vertical) directions gave evidence that the 4 layer Fe film is strongly distorted by the copper substrate.

In summary, the determination of modulation amplitudes in incommensurate structures is quite involved and still in its beginning. Very useful information on film thickness, interlayer spacings and stacking sequence in incommensurate thin films can, however, already be ex-

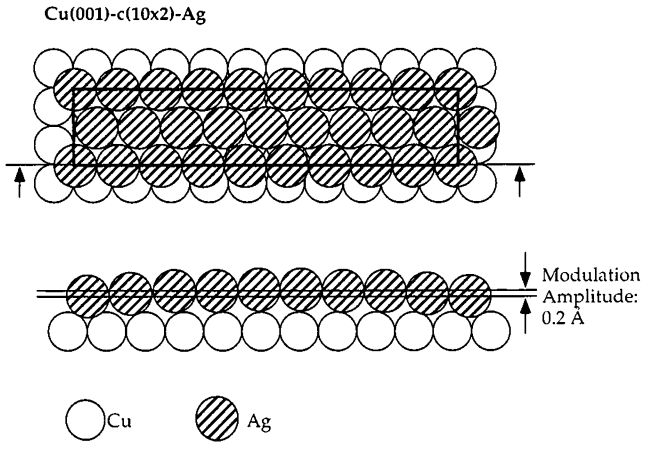

Fig. 42. Structure of the Cu(001)–c(10 × 2)–Ag structure, together with the modulation amplitude of the Ag film (see Ref. [115]); a sine-like vertical modulation of the film was assumed.

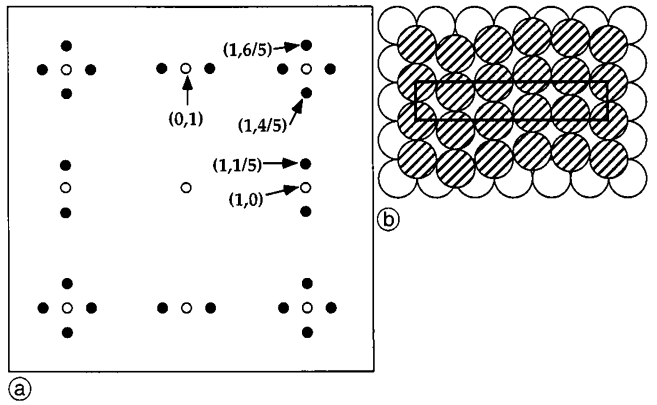

Fig. 43. (**a**) Schematic of the dominant spots in the Cu(001)–(5 × 1)–Fe phase and corresponding structural model for the lateral modulations within the Fe film. (**b**) The positions of the intense reflections are consistent with sine-like lateral modulations; the (5 × 1) unit cell is shown (solid rectangle). (after Ref. [116]).

tracted from the LEED data if one neglects those modulations and assumes that the individual adlayers are periodic. For this case, efficient approximation schemes like the "mirror approximation" introduced in section 4.2 can be applied, allowing the use of the small (1 × 1) unit cell of the evenly dispersed adlayer for the LEED structure analysis.

V. Surface structure of quasicrystals

5.1 Introduction

In this section, we turn to LEED investigations of quasicrystalline surfaces. Quasicrystals, which were discovered by Shechtman et al. in 1984 [158], are a new class of materials which combine long-range translational and rotational order with the absence of a periodic crystal lattice. This is evidenced by diffraction patterns with sharp spots, indicative of long-range order, which exhibit symmetries which are forbidden for a periodic crystal lattice. As an example, a LEED pattern obtained for the quasicrystalline $Al_{70}Pd_{21}Mn_9$ alloy is shown in Fig. 44 [159, 160]. Its fivefold rotational symmetry is forbidden for periodic lattices, while the sharp spots point towards good long-range order within the coherence length of the electron beam. The aperiodic long-range order manifests itself also in irregular, non periodic spacings between the spots in the diffraction pattern. As discussed further below (section 5.3), the positions and intensities of the spots in the aperiodic diffraction pattern already contain important information on characteristic lengths and distances in quasicrystalline surfaces.

Recently, surfaces of quasicrystals have attracted much interest due to their special properties such as their corrosion resistance, their hardness, and their low friction coefficients [161]. Because of these properties, quasicrystalline alloys may find important technical applications, for example as surface coatings for wear resistance in corrosive environments. The properties of interest – friction, adhesion, and corrosion – are all determined by phenomena at surface or interfacial regions. Up to know, very little is known about these underlying phenomena; a knowledge of the surface structure may be an important step for a deeper understanding of the surface properties of quasicrystalline alloys.

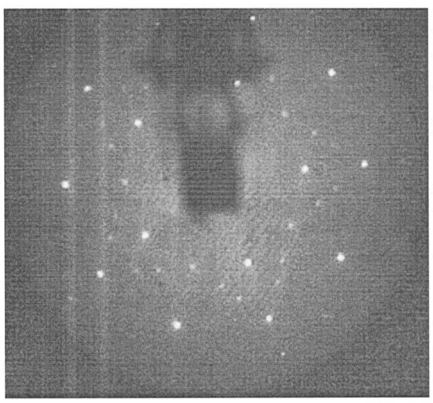

Fig. 44. LEED pattern for the fivefold $Al_{70}Pd_{21}Mn_9$ surface at 80 eV incident electron energy and normal incidence. Two rings with intense spots can be discerned, with spots of weaker intensity in between. Each ring consists of two sets of five spots which are symmetrically equivalent. Some spots are obscured by the sample manipulator (dark shadow at top and in the middle).

In order to analyze quasicrystalline surface structures by LEED, several difficulties have to be overcome, both on the experimental and the theoretical front. For the LEED calculations, one is confronted with the problem that it is not possible to define a surface unit cell with finite size for the aperiodic surface of a quasicrystal. Because the time required for the calculation of LEED I(E) curves for a structure model strongly increases with the size of the surface unit cell, LEED analyses of quasicrystal surfaces are not possible without using efficient approximations. A similar problem arises with the incommensurate structures described in the last section. Compared to the incommensurate systems, quasicrystalline surfaces introduce, however, a further level of complication in that it is impossible to describe quasicrystalline structures using one or more periodic layers with small modulations. With the incommensurate structures treated in the last sections, the translational symmetry of adsorbate and substrate taken together is lost or reduced, but the individual adlayer and substrate layers still maintain an average periodic structure; the approximation schemes discussed in the last section, like the "mirror approximation", are based on this fact. Recently, suitable approximations were developed also for LEED calculations with quasicrystalline surfaces [162], and a structural analysis of the fivefold $Al_{70}Pd_{21}Mn_9$ surface demonstrated that quasicrystalline structures are accessible to LEED theory.

Experimentally, one of the main impediments to studies of quasicrystal surfaces is the scarcity of good, large samples. The first quasicrystalline alloys discovered, as for example the AlMn alloy by Shechtman et al. [158], were thermodynamically unstable. Only small, μm-sized grains could be produced by very rapid cooling using the melt-spinning technique, thus freezing the solid in the quasicrystalline state (A grain is thereby a region of the solid that contains atomic clusters with a single coherent orientation). This situation changed after the discovery of alloys which are stable up to the melting point; among them are $Al_{65}Cu_{20}Fe_{15}$ [163] and $Al_{70}Pd_{21}Mn_9$ [164]. Their degree of quasiperiodic order could be improved by heating close to the melting point, and is similar to the degree of order in periodic crystals, as derived from the sharpness of the spots in their x-ray or neutron diffraction patterns.

With $Al_{65}Cu_{20}Fe_{15}$ and $Al_{70}Pd_{21}Mn_9$, one can produce single grains large enough to apply surface sensitive techniques [165]. For $Al_{70}Pd_{21}Mn_9$, large single grains (of the order of several cm^3) can be obtained using conventional crystal-growing techniques like the Bridgman method. Also because it is routinely possible to grow large samples, most of the investigations of quasicrystal surfaces deal with the $Al_{70}Pd_{21}Mn_9$ system. Only recently, large single grain samples of quasicrystalline $Al_{65}Cu_{20}Fe_{15}$ were obtained [165b]. For this alloy it was, however, not sufficient to apply conventional crystal growth techniques. It does not grow directly from the liquid but is the product of a peritectic solidification reaction between different high-temperature crystalline phases. For potential applica-

tions as surface coatings, quasicrystalline AlCuFe is receiving much attention, also because it consists of inexpensive, non toxic metals.

The $Al_{70}Pd_{21}Mn_9$ and $Al_{65}Cu_{20}Fe_{15}$ materials mentioned above belong to the class of icosahedral quasicrystals, i.e. they have the same point group symmetry as an icosahedron. Diffraction patterns along different directions of an icosahedral crystal may have onefold, twofold, threefold, or fivefold rotational symmetry. Icosahedral phases were discovered among aluminum based alloys, as well as among alloys of titanium and transition metals, among alloys of gallium, magnesium and zinc and also among alloys of uranium, palladium and silicon (for reviews, see, e.g., [166]).

The fivefold symmetric surface of $Al_{70}Pd_{21}Mn_9$ has been subjected to detailed investigations by LEED, whereby symmetry and positions of the spots showed that the quasicrystalline long-range order at the surface is similar as in the bulk [159, 160, 162], The fully dynamical LEED structural analysis for $Al_{70}Pd_{21}Mn_9$ revealed that the surface consists of a mixture of very similar, bulk like terminations [162]; the bulk structure was determined by x-ray and neutron diffraction [167]. More recently, it was shown that it is possible to prepare stable structures of a twofold $Al_{70}Pd_{21}Mn_9$ surface [168] and a fivefold surface of $Al_{65}Cu_{20}Fe_{15}$ [169]; for the latter, the LEED pattern is akin to the pattern obtained for fivefold $Al_{70}Pd_{21}Mn_9$ shown in Fig. 44.

Other stable aperiodic systems were found among decagonal alloys, which are quasicrystalline in a plane and periodic perpendicular to that plane. The decagonal phase produces a diffraction pattern with a tenfold rotational axis if the direction of incidence is perpendicular to the quasiperiodic planes. Among these materials is the decagonal phase of AlCoCu [170], the first quasicrystalline system for which a LEED study was carried out [171].

In the following, we will describe LEED studies of quasicrystalline surfaces in more detail. The chapter about quasicrystalline surfaces is organized as follows: In section 5.2, we will consider the special, quasicrystalline long-range order in more detail and will briefly describe how quasicrystalline models with atomic coordinates can be derived. Then, we turn to LEED studies of quasicrystalline surfaces and discuss how information on characteristic distances and long-range order can be extracted from the positions and relative intensities of the spots in the LEED pattern (section 5.3); thereby, we mainly concentrate on surfaces of $Al_{70}Pd_{21}Mn_9$. In section 5.4, we describe fully dynamical LEED analyses of the fivefold and twofold surfaces of $Al_{70}Pd_{21}Mn_9$. We will briefly explain the approximations which are applied for the calculation of I(E) curves for quasicrystalline structures. The results for the $Al_{70}Pd_{21}Mn_9$ icosahedral phase will be given and discussed in the context of other surface sensitive experiments.

5.2 Some aspects of quasicrystalline order

Although they are not periodic, quasicrystals exhibit translational and orientational long-range order. Orientational long-range order means that the orientation of local atomic clusters is correlated over long distances resulting in the same orientation of all clusters of the same type. An illustrative example is provided by the surface of the $Al_{70}Pd_{21}Mn_9$ icosahedral alloy which was investigated by Schaub et al. using LEED and STM [159]. After sputtering and annealing in ultra high vacuum, microfacets were obtained which grow perpendicular to a fivefold axis of the bulk alloy and exhibit fivefold symmetry in their LEED patterns. The surface topology of these facets can be described by a set of atomically flat terraces. STM images of the terraces reveal pentagonally shaped holes (Fig. 45). All of those fivefold objects have the same orientation, even if they are on different terraces, thus indicating long-range orientational order.

Beyond the long-range orientational order, quasicrystals possess also a special kind of translational long-range order. Unlike crystals, which have translational symmetry, the structure of quasicrystals is quasiperiodic, a well defined but more subtle kind of translational order. Quasiperiodic order resembles the ordinary periodic order insofar as it determines the position of all atomic clusters up to infinity when starting with an initial arrangement of clusters. Let us consider, for example, the fivefold surface of the $Al_{70}Pd_{21}Mn_9$ icosahedral alloy with the pentagonal holes visible with STM. By connecting the edges of the pentagonal holes, one obtains a pentagrid with five sets of lines, one of which is shown in Fig. 45. Two line separations are found, namely a wide one (W) and a narrow one (N); the ratio between W and N is close to the golden mean $\tau = (1 + \sqrt{5})/2$, an irrational number which plays also an important role in the geometry of pentagons and icosahedra. The succession of distances between neighboring grid lines is part of the infinite Fibonacci chain, and the distribution of the pentagonally shaped holes is determined by the Fibonacci pentagrid as depicted in Fig. 46. The long-range order described above is quasiperiodic: While the positions of the pentagonal clusters are determined by the Fibonacci grid up to infinity, the resulting structure is aperiodic, as reflected by the occurrence of two distances W and N, whereby W/N is irrational. Quasi-

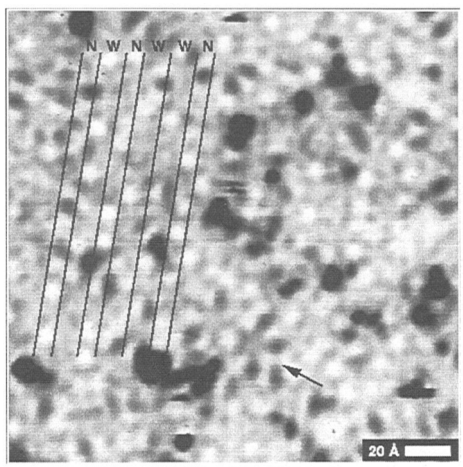

Fig. 45. STM image of a fivefold symmetric terrace with pentagonally shaped holes (from [159c]). A Fibonacci pentagrid can be constructed by connecting the edges of the pentagons with straight lines. Only one set of lines is partially shown; the ratio W/N is close to the golden mean τ.

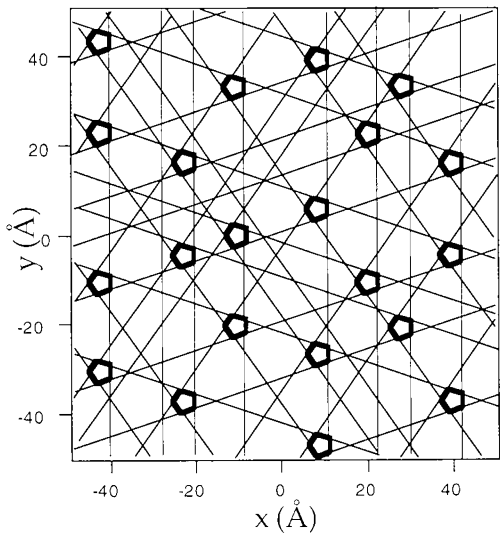

Fig. 46. Fibonacci grid that describes the distribution of the pentagonally shaped holes at the fivefold $Al_{70}Pd_{21}Mn_9$ surface. All pentagons (thick lines) have the same size and orientation (see [159]).

periodic order was found also perpendicular to the fivefold symmetric surface of $Al_{70}Pd_{21}Mn_9$: The terraces are separated by steps of two different heights in a succession corresponding to a Fibonacci sequence. The ratio between the heights of the large and the small step is again close to the golden mean τ (Fig. 47) [159].

While there are only a few investigations of the surface structure of quasicrystals so far, much more structural studies deal with their bulk geometry; a knowledge of the bulk configuration may, however, be very helpful in order to find suitable starting models for an analysis of the surface structure by LEED. The most important tools used for quantitative bulk structure determination are x-ray and neutron diffraction [167, 172]. For the structural modeling of quasicrystals, two approaches are used: 1) In the tiling approach, a quasiperiodic arrangement of atoms is made up by two or more different unit cells (or tiles) which are "decorated" with atomic clusters. The well known Penrose tiling shown in Fig. 48 consists, for example, of a fat and a skinny rhombus and has fivefold rotational symmetry. As shown in Fig. 49, the Penrose tiling exhibits quasicrystalline long-range order which can be described by a Fibonacci pentagrid (very much like the fivefold $Al_{70}Pd_{21}Mn_9$ surface). 2) In the higher dimensional approach, quasiperiodic structures are described as irrational sections of extended "hyperatoms" on a higher dimensional periodic lattice; detailed descriptions of the higher dimensional crystallography of quasicrystals can be found, for example, in [173]. A simple example of the higher dimensional approach is shown in Fig. 50: It is possible to construct a quasiperiodic Fibonacci chain by a cut through a two dimensional, periodic square lattice along an axis rotated by an angle $\arcsin(1/\sqrt{(1+\tau^2)}) = 31.7°$ with respect to the

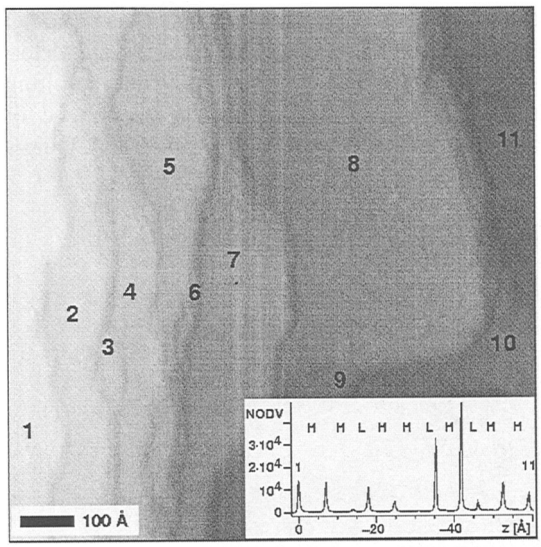

Fig. 47. STM image of icosahedral AlPdMn after annealing close to the melting point. The atomically flat terraces visible on this 1000×1000 Å^2 image are separated by steps of two different heights. Bottom right: Histogram obtained from the STM image. Shown is the absolute frequency of measured z-values, whereby z points along the surface normal (NODV: Number of data values). The heights of steps separating neighboring terraces take only the values L (L = "low step") and H = τL (H = "high step"). The sequence of step heights between terrace #1 and terrace #11 is part of the Fibonacci chain (From Ref. [159c]).

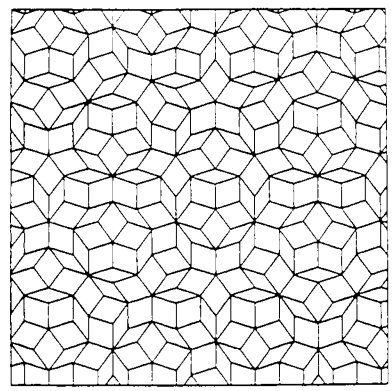

Fig. 48. Section of a Penrose tiling with fat and skinny rhombic unit cells. The tiling has perfect pentagonal orientational order and quasiperiodic translational order.

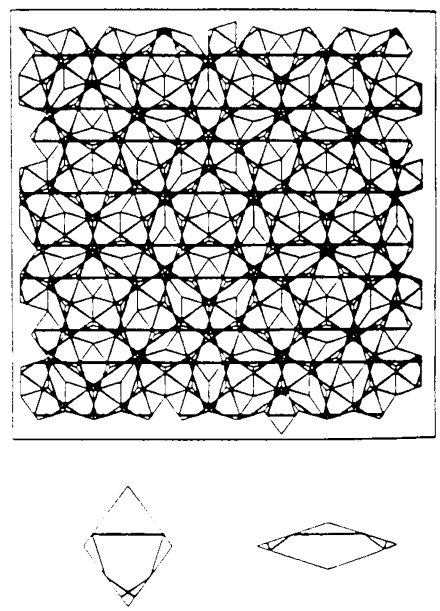

Fig. 49. Each tile of the Penrose tiling has been decorated with line segments as shown at the bottom. These line segments join to form a Fibonacci pentagrid, thus demonstrating that the Penrose tiling has quasiperiodic long-range order (from Ref. [173a]).

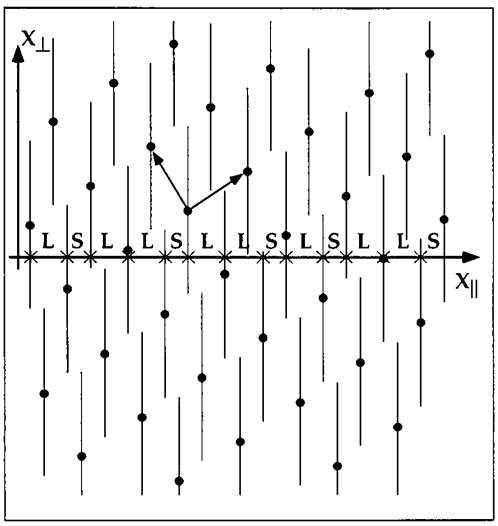

Fig. 50. Construction of a Fibonacci sequence by projection of a periodic, two-dimensional lattice with extended atomic objects onto the one-dimensional physical space $x_\parallel$; the basis vectors of the two-dimensional lattice are shown. In the two-dimensional periodic lattice, the atomic objects are not point-like but they are represented by line segments. The intersections of these line segments with $x_\parallel$ determine the atom positions in the physical space. In $x_\parallel$, the atoms form a Fibonacci chain. The ratio of the long distance L and the short distance S is equal to the golden mean τ.

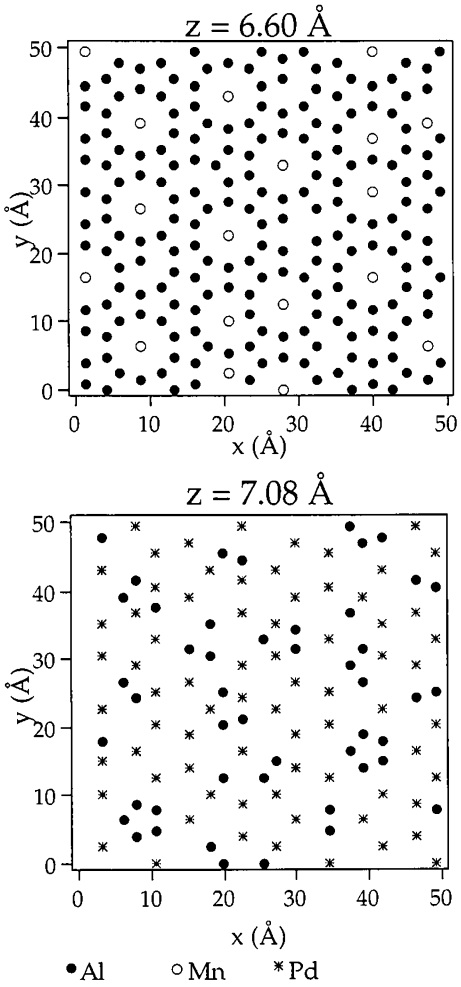

Fig. 51. Two successive planes of icosahedral AlPdMn perpendicular to a fivefold axis.

axes of the square lattice. This axis is called the "physical space" and labeled as $x_\parallel$ while its orthogonal partner is denoted by $x_\perp$. In order to produce point-like atoms in the physical space, the atoms in two dimensions can be represented by extended objects, such as the line segments of length L in Fig. 50. The intersection of the atomic objects with $x_\parallel$ determines the positions of atoms in the physical space. In the same way, a three dimensional quasicrystalline structure can be obtained by a cut along a three dimensional hyperplane $x_\parallel$ through a six-dimensional periodic lattice. Thereby, the atoms have to be represented as extended, 3-dimensional objects in the 6-dimensional space in order to get point-like objects in the 3-dimensional "physical" space. Using diffraction methods, such as x-ray or neutron diffraction, it is possible to get insight into the positions and shapes of the atomic objects in the 6-dimensional lattice. x-ray and neutron diffraction led, for example, to a model for the icosahedral phase of AlPdMn, consisting of shells of spheres located on the nodes of a 6-dimensional bcc lattice [167]. By projection to the three-dimensional "physical space", one obtains the coordinates of the atoms in the $Al_{70}Pd_{21}Mn_9$ quasicrystal. These coordinates were used as starting configuration in the LEED structural analysis of this surface [162].

In the structure of $Al_{70}Pd_{21}Mn_9$ obtained by x-ray and neutron diffraction, dense atomic planes show up perpendicular to the fivefold direction. Two bulk planes perpendicular to a fivefold axis are shown in Fig. 51 while in Fig. 52 the planes are drawn at their respective depths z.

As evidenced by x-ray and neutron diffraction analyses, the basic "building blocks" of many icosahedral quasicrystals are icosahedral or dodecahedral clusters; thus, also the local environment of the majority of the

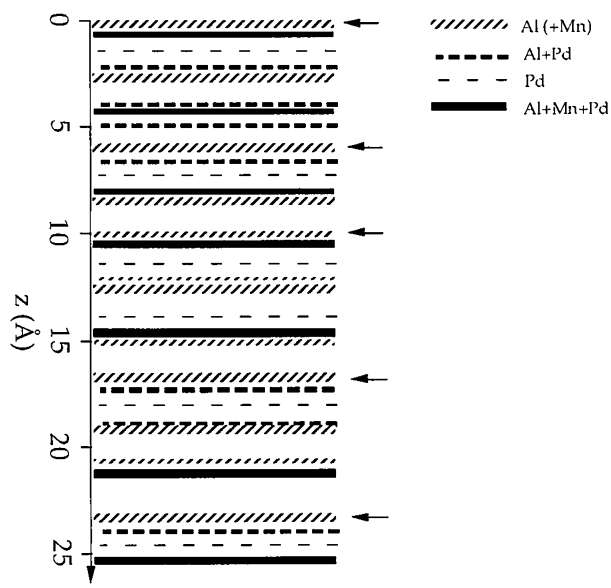

Fig. 52. Atomic planes of icosahedral AlPdMn are drawn at their respective depths z, as bars with thickness proportional to the atomic density in each plane, together with their approximate composition as symbolized at the right of the figure (parentheses indicate minority species). The origin was chosen arbitrarily. By the arrows, the topmost layers of a class of very similar terminations are indicated. These terminations are separated by step heights as visible with STM [159] and give good agreement in the LEED analysis (see section 5.4); the z axis points towards the bulk.

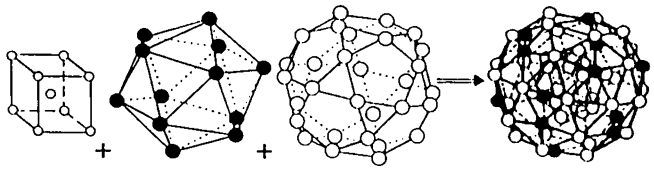

Fig. 53. Pseudo Mackay icosahedron which is considered to be the basic building block of the icosahedral Al–Pd–Mn quasicrystal. It consists of an inner shell (partially occupied small dodecahedron, left), an icosahedron (middle) and an outer shell (icosidodecahedron, right).

atoms has icosahedral symmetry. For $Al_{70}Pd_{21}Mn_9$, the x-ray and neutron diffraction analysis in [167] suggests that most of the atoms form so called pseudo Mackay icosahedra (Fig. 53). They consist of a part of a small dodecahedron, surrounded by an icosahedron and an outer shell (icosidodecahedron). A x-ray photoelectron study of icosahedral $Al_{70}Pd_{21}Mn_9$ gave direct evidence for the existence of icosahedral clusters in the surface region [174]. It should, however, be pointed out that the details of the bulk structure of AlPdMn are still subject of debate, and that there is evidence for disorder and complexity in this structure [175]. Also the nature and detailed structure of the atomic clusters forming the $Al_{70}Pd_{21}Mn_9$ quasicrystal is still under discussion [176].

Further evidence for the existence of Mackay type clusters in the surface region of $Al_{70}Pd_{21}Mn_9$ was obtained in recent STM studies of samples prepared by in situ cleavage along twofold and fivefold directions [177]. In that study the surface structure was found to be determined by cluster aggregates on the basis of an elementary cluster whose diameter of about 10 Å points toward the pseudo Mackay icosahedron. The surface was found to be rough, in contrast to the investigations by Schaub et al. [159] discussed above, which revealed the occurrence of large, flat terraces. Obviously, the surface morphology is strongly influenced by the effects of various preparation techniques: Flat and well ordered surface regions form only after annealing close to the melting point [159, 178].

5.3 LEED studies of quasicrystals: Information from the diffraction pattern

Important information on the ordered part of quasicrystalline surfaces can already be extracted from the LEED pattern. The first LEED study for a quasicrystalline system was carried out for the decagonal phase of $Al_{65}Cu_{15}Co_{20}$ [171], giving rise to a tenfold symmetric LEED pattern if the direction of incidence is perpendicular to the quasiperiodic planes, and a twofold pattern if it is along those planes; the twofold pattern is periodic in one direction. The LEED patterns of the twofold and tenfold surfaces indicate that the long-range order in the surface region of $Al_{65}Cu_{15}Co_{20}$ is similar to that in the bulk: From the spot positions of the twofold pattern, one can estimate the interlayer spacing between the quasiperiodic layers which turns out to agree with the bulk value within the error bars; the spot positions of the tenfold pattern indicate that the long-range order of the tenfold surface is similar to that in the bulk. Temperature-dependent measurements revealed the existence of an unusual disordering transition

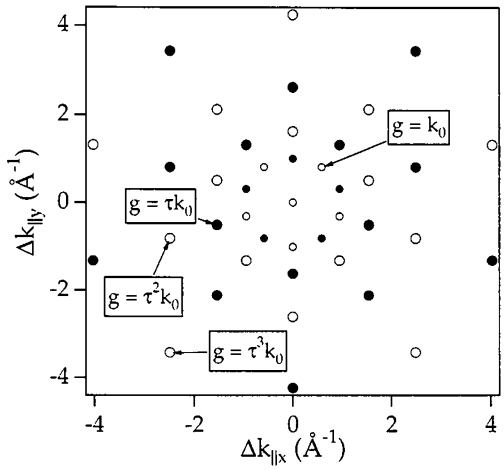

Fig. 54. Schematic of the LEED pattern of the fivefold $Al_{70}Pd_{21}Mn_9$ surface, showing the spots visible in the 70–240 eV range (The second and third ring are clearly visible in the LEED pattern in Fig. 44 which was taken at E = 80 eV). The pattern consists of rings with intense reflections. The weak spots between the rings are not shown in the figure. The radii of the rings are related by the golden mean τ, as indicated in the figure, g is the modulus of the parallel momentum transfer (k_0 = 1.00 Å^{-1}).

for the tenfold planes, as evidenced by a sudden weakening of the non specular LEED spots at a critical temperature $T = 715$ K (well below the bulk melting point of 1280 K). The nature of this phase transition is not clear at the moment.

From the positions of the LEED spots, characteristic lengths can be deduced; these lengths may correspond to distances between atomic clusters, as exemplified with the fivefold surface of $Al_{70}Pd_{21}Mn_9$ in the next paragraphs.

As shown by Schaub et al., the major spots in the LEED pattern of fivefold $Al_{70}Pd_{21}Mn_9$ are located on rings whereby the radii of consecutive rings r_j, normalized to the smallest such radius r_0, should equal the golden mean $\tau(\tau = (1 + \sqrt{5}))/2)$ raised to integral powers: $r_j/r_0 = \tau^j$ (see also the schematic in Fig. 54). Two of these rings with bright spots can be discerned in the LEED pattern in Fig. 44. It can be shown that the spot positions in the LEED pattern are a consequence of the quasiperiodic long-range order which is determined by the Fibonacci pentagrid shown in Fig. 46. To this end, it is instructive to consider the Fourier transform of a one-dimensional Fibonacci chain [159]. As shown in Fig. 55, the Fourier transform exhibits an infinite number of Bragg peaks which are dense in the reciprocal space. Only a few of these peaks, however, have notable intensity, and they are located at wave vectors k_0, τk_0, $\tau^2 k_0$, and $\tau^3 k_0$, with $k_0 = 2\pi\sigma^2/\sqrt{5}N$ and N being equal to the narrow spacing in the Fibonacci chain. Accordingly, Fourier transformation of a Fibonacci pentagrid leads to rings with intense spots at those positions, as observed also in the diffraction pattern of fivefold $Al_{70}Pd_{21}Mn_9$. From these spot positions in the LEED pattern, one can estimate the narrow and wide separation of the Fibonacci pentagrid, which amount to N = (7.24 ± 0.10) Å and W = τN = (11.72 ± 0.16) Å, respectively [159]. These values agree within the error bars with those found by STM. The LEED pattern of the surface furthermore indicates that the quasicrystalline long-range

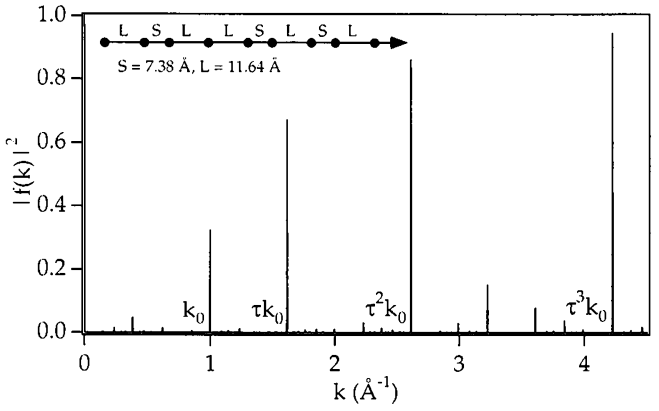

Fig. 55. Fourier transform of a Fibonacci chain with N = 7.38 Å and W = 11.76 Å (values expected for an unreconstructed fivefold $Al_{70}Pd_{21}Mn_9$ surface). The Fibonacci chain is shown in the inset (upper left). The Fourier transform exhibits an infinite number of Bragg peaks which are dense in k space; only a few of them have notable intensity, for example the reflections at k_0, τk_0, $\tau^2 k_0$, and $\tau^3 k_0$, with $k_0 = 2\pi\sigma^2/(\sqrt{5}N)$. The positions correspond to the radii of the rings with intense spots in the LEED pattern (Figs. 44, 54).

order is similar to that in the bulk, since the spots are at the positions of an unreconstructed surface [159, 162].

For $Al_{70}Pd_{21}Mn_9$, also a stable quasicrystalline twofold surface could be prepared by sputtering and annealing [168]. After sputtering, but prior to annealing at temperatures above 600 K, no LEED pattern could be observed while Auger spectroscopy revealed a composition of $Al_{62}Pd_{32}Mn_6$, well away from the composition of the icosahedral phase. After resputtering and annealing at approximately 600 K, a "rhombic" LEED pattern exhibiting twofold symmetry was observed. The diffraction spots were, however, quite broad, and did not coincide with the 2-fold or any other pattern derived from the bulk structure. At best, this structure may be characterized as a highly disordered and distorted icosahedral phase. After annealing above 800 K, the LEED pattern changed dramatically: The diffuse spots were replaced by a new sharp, rectangular LEED pattern, which exhibits twofold symmetry (Fig. 56). In order to confirm whether this pattern is characteristic of an ordered surface of the icosahedral phase, the LEED pattern expected for an unreconstructed surface

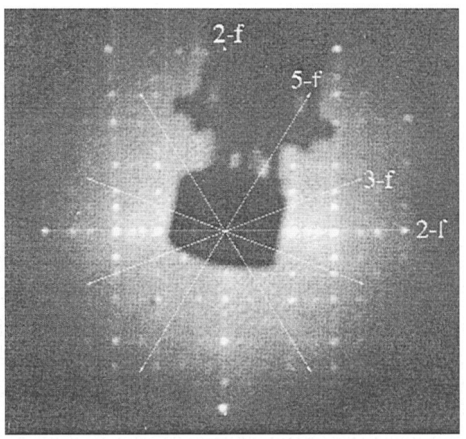

Fig. 56. LEED pattern of a two-dimensional $Al_{70}Pd_{21}Mn_9$ surface, recorded at E = 70 eV (from Ref. [168]).

was calculated. In doing so, the bulk x-ray structure factors as measured by Boudard et al. [167] for $Al_{70}Pd_{21}Mn_9$ were employed and used to assign a relative intensity to rods parallel to the surface normal. The positions and intensities derived in this way qualitatively agreed with those measured in the LEED pattern, thus indicating that the quasicrystalline long-range order at the twofold surface is similar as in the bulk.

5.4 LEED structural analysis of quasicrystalline AlPdMn surfaces

The LEED studies described above have been limited to observations and discussions of the symmetry and spacing of the diffraction spots, in order to determine whether the surface retains the quasicrystallinity of the bulk. They did not exploit the strength of dynamical LEED as a tool for obtaining atomic-scale information on surface structure and composition.

Quasicrystals pose special challenges to diffraction theory, previously worked out for the cases of x-rays and neutrons. In LEED, multiple scattering adds further complications: The aperiodicity of quasicrystals, and of quasicrystal surfaces in particular, implies a wide variety of local structures, and an intractable number of atoms with different scattering properties; note that the scattering properties of an atom depend in effect on its local environment in the case of multiple scattering [54]. The time necessary to calculate LEED I(E) curves for a structure model strongly increases with the number of atoms with different scattering properties. In periodic crystals, this number is restricted by the size of the two dimensional surface unit cell and the number of atomic planes to be taken into account, which is determined by the inelastic mean free path of the electrons [5]. For a quasicrystal, however, this consideration does not hold since it is not possible to define a surface unit cell of finite size. Thus, approximations in the LEED theory are necessary, and an appropriate LEED formalism had to be developed for a quasicrystalline surface region. In the following, we will describe this approach and its application for a LEED structure analysis of the fivefold symmetric surface of the icosahedral $Al_{70}Pd_{21}Mn_9$ alloy. The approach can be applied, however, also for LEED analyses of other quasicrystal surfaces.

As a starting point for the LEED analysis, the bulk structure of icosahedral AlPdMn determined by x-ray and neutron diffraction [167] was used, and a large set of possible ideal bulk-like fivefold surface terminations was considered, bounded by a box of 100×100 Å^2 which is 50 Å deep (see also Fig. 52). As a result of quasiperiodicity, all of these terminations are, in principle, different. Many of them have, however, very similar chemical compositions and geometries so that only a finite number of qualitatively different terminations has to be considered. Each of these surfaces is represented as individual layers (parallel to the surface) of coplanar atoms with a particular composition and density.

To account for multiple scattering, efficient approximations have to be used. In this paragraph, we describe the concept of these approximations, as illustrated also in

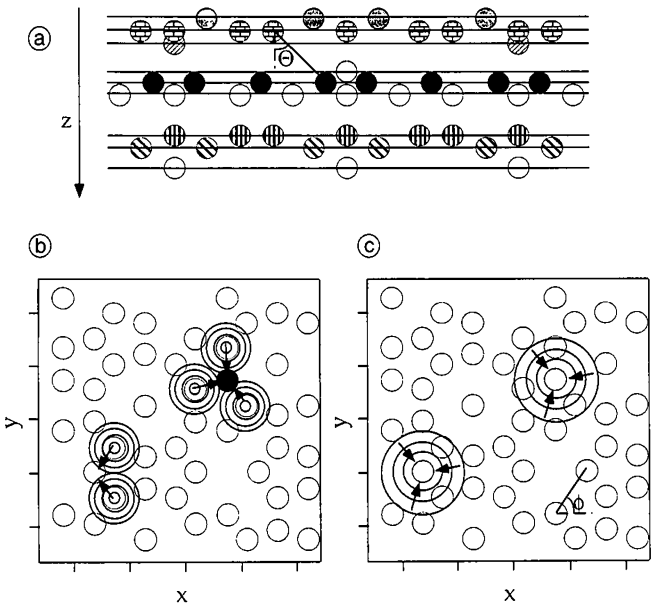

Fig. 57. Illustration of the approximations used for LEED I(E) calculations with quasicrystal surfaces: (**a**) The scattering properties of all atoms in a coplanar layer are assumed to be equal (spheres filled with the same pattern stand for atoms whose scattering properties are assumed to be equal). (**b**) In a quasicrystal, the neighborhood of each atom is different, due to the aperiodicity. The atoms symbolized by the filled spheres have, for example, a different local environment. In the case of multiple scattering, the neighborhood influences also the scattering properties of an atom, because the wave field of the incident beam is modulated in the presence of the neighbors (the circles symbolize spherical waves emitted by the neighboring atoms, changing the incident wave field at the positions of the atoms marked by filled spheres). (**c**) The neighborhood of all atoms in a coplanar layer is replaced by a simplified, averaged neighborhood which is independent of the azimuth; in this case the incident wave field, symbolized by the circles, depends only on the distances to the neighboring atoms and on the polar angle θ but not on the azimuth φ.

Fig. 57. For details, the reader is referred to Ref. [162b]. First, one has to reduce the number of atoms with different scattering properties used in the calculation. As mentioned above, the time required for calculations of I(E) curves is determined by this number. To this end, the scattering properties of all atoms within a coplanar layer were assumed to be equal (Fig. 57a). In doing so, the calculations can be performed with one atom per layer, i.e., 10 different atoms if 10 layers have to be taken into account (note that contributions of deeper lying layers are strongly damped due to inelastic scattering). Under these conditions, the contribution of each layer to the scattering amplitude can be written as a product of a form factor with a lattice factor. The lattice factor is determined by the lateral, aperiodic arrangement of the atoms and has sharp maxima at those positions where the spot positions in the LEED pattern are. The atomic form factor is in the case of LEED strongly influenced by multiple scattering and is determined not only by the scattering matrix of an atom itself but also by its local environment; this environment strongly modulates the incoming wave field of the LEED electrons. Within the approximation, the complex local environments of the atoms in a quasicrystal are replaced by a simplified, averaged neighborhood, which is assumed to be equal for each plane. As illustrated in Fig. 57b, c, it is assumed that the distribution of neighbors around each atom in the averaged neighborhood depends only on the polar angle (perpendicular to the surface, cf. Fig. 57) and the interatomic distances, but not on the azimuth. This approximation should hold especially for highly symmetric structures (such as fivefold surfaces). Under these conditions one obtains a simplified expression for the propagator matrix describing the propagation of the electron wave field between the atoms.

Using this approach, the experimental data of the fivefold symmetric surface of $Al_{70}Pd_{21}Mn_9$ were successfully analyzed. In a first step, the topmost interlayer spacings were optimized for each termination. It was found that the better fitting terminations are very similar, exhibiting a densely packed, Al-rich outermost atomic layer followed by a layer containing about 50% Al and 50% Pd; some of the better fitting terminations are indicated by arrows in Fig. 52. The topmost interlayer spacing of 0.38 Å is systematically reduced by 0.1 Å from the bulk value of 0.48 Å, which trend is consistent with clean single-crystal results of comparable local buckled structures (e.g., stepped fcc surfaces). The interlayer spacings of deeper layers are almost bulk-like. In line with the STM observations of Schaub et al., many of these terminations are separated by steps with heights of 4.08 or 6.60 Å. Low-energy ion scattering data also support the composition of the favored layers [162b].

Next, different terminations were averaged together with equal weight to model the case of terraces, each having one of the different terminations. By mixing the intensities obtained for the 10 best terminations, the Pendry R factor could be reduced from 0.40 to 0.31. This agreement is comparable to that found in many other successful structure determinations, particularly for complex surfaces. The resulting optimum geometry is shown in Fig. 58.

In the following, we describe results of calculations of a strongly corrugated surface with intact Mackay type clusters. These calculations were motivated by the fact

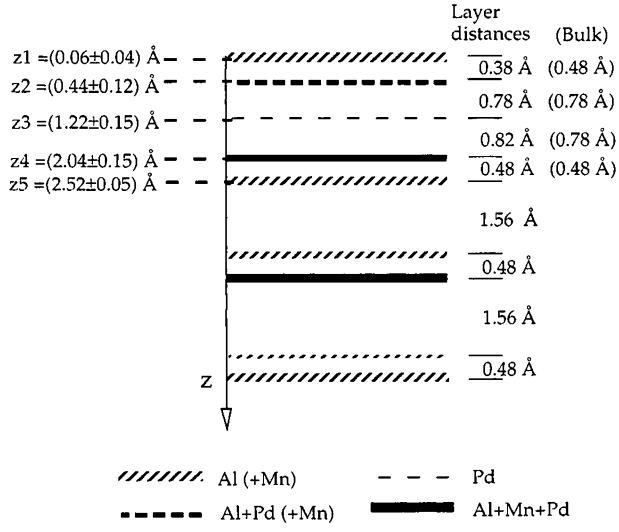

Fig. 58. Optimum geometry found in the LEED structural analysis of the fivefold $Al_{70}Pd_{21}Mn_9$ surface. Given are the topmost layer spacings, compared with their bulk values (bulk values in parentheses). The planes are drawn at their respective depths z, as bars with thickness proportional to the atomic density in each plane, together with their approximate composition (as labeled below).

that there is evidence for surface roughness after cleaving in situ, with aggregates of Mackay type clusters at the surface [177]. The termination chosen for these calculations belongs to the group of better fitting terminations described above and contains many intact pseudo Mackay icosahedra in the surface region (see Fig. 59a). In a first step, only atoms within the Mackay clusters were taken into account for the topmost layers. The equatorial plane of the clusters, 4.56 Å underneath the surface layer, is the first layer for which all atoms are taken into account in the calculation. An optimization of the topmost interlayer spacings led, however, to a very bad agreement between theory and experiment ($R_{Pendry} = 0.68$) so that this configuration can be ruled out.

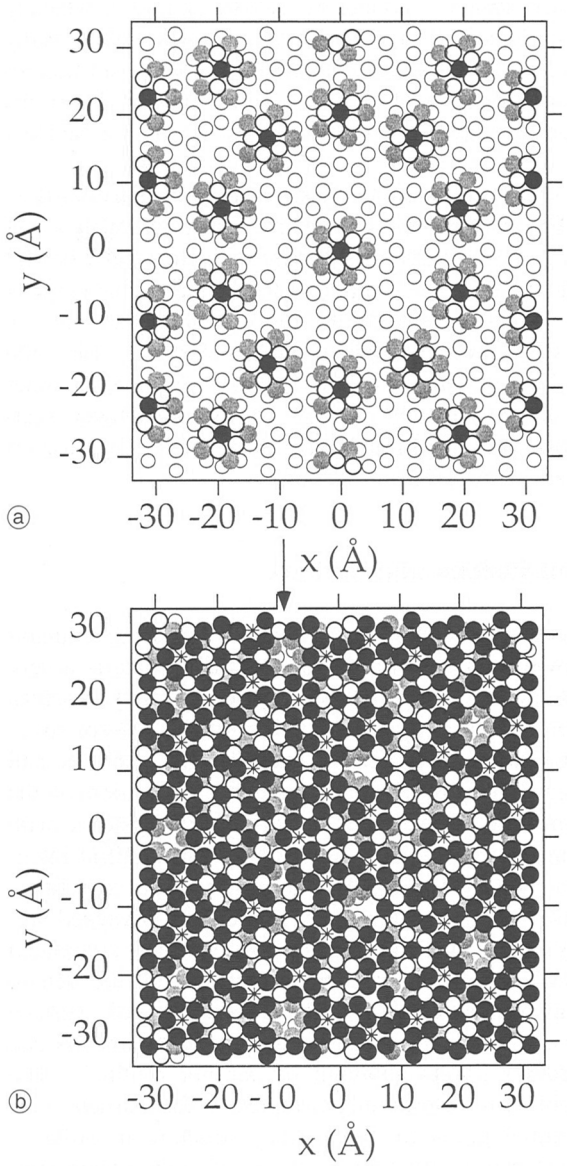

Fig. 59. Configurations used for the I(E) calculations of a rough surface of fivefold $Al_{70}Pd_{21}Mn_9$. For these configurations, one of the better fitting terminations was chosen. (**a**) Only atoms within pseudo Mackay icosahedra (PMI) were taken. Full circles: topmost atoms of the PMI, open circles: 2nd plane (0.48 Å underneath), gray circles: 3rd plane (1.26 Å underneath). Small open circles: plane 4.56 Å underneath; this is the first plane where all atoms are taken into account in the I(E) calculation. The equatorial planes of the Mackay clusters lie within this plane and consist of rings with 10 atoms. (Two further planes, located 2.52 Å and 4.08 Å underneath the topmost plane, are not shown). (**b**) Complete, bulk-like termination. Only the topmost two planes of the Mackay icosahedra are exposed to the surface, showing up as pentagons with an Al (or Mn) atom in the topmost plane, surrounded by five Al or Pd atoms underneath (indicated by the pentagon in the figure). The PMI lie on a Fibonacci pentagrid, as well as the larger and deeper holes indicated by the arrow.

Much better agreement was achieved for the "flat" surface termination shown in Fig. 59b. A LEED calculation for this termination leads to an R_{Pendry} value of 0.38, thus indicating that the surface is not strongly corrugated at an atomic level.

The dense, Al-rich terminations found in the structure analysis correlate with factors known to govern surface compositions of crystalline alloys. At those simpler surfaces, one finds preferential segregation by components with lower surface free energy, larger atomic volume and more positive heat of solution [179]. The surface free energy typically is the dominant factor. The Al-rich terminations found here are expected if these factors are taken into account [179].

The LEED structural analysis of $Al_{70}Pd_{21}Mn_9$, as well as the STM measurements by Schaub et al. [159], point towards an atomically flat surface after the surface treatment with sputtering and annealing: In order to get such a flat surface it is necessary to anneal to temperatures close to the melting point. While the LEED I(E) data are consistent with a surface which is flat on an atomic level, the sharpness of the LEED spots indicates that the surface is not rough on a larger scale of several 100 Å (the coherence length of the LEED beam). Otherwise, one would expect a broadening of the spots due to the worsening of the long-range order. In contrast, STM investigations of AlPdMn prepared by in-situ cleavage revealed significant atomic scale roughness [177], with cluster aggregates on the surface formed on the basis of Mackay type clusters. Although the surface morphology is different, many Mackay type clusters are present also in the structure found by LEED (cf. Fig. 59). They are, however, embedded within an Al rich surface layer. It is also instructive to compare the positions of the topmost atomic planes with the vertical positions of atoms in a pseudo Mackay icosahedron (PMI) oriented along a fivefold axis. It turns out that each plane of the Mackay cluster has its counterpart in the AlPdMn surface structure (see Fig. 60). This gives evidence for many intact, Mackay type clusters in the surface region, with some of the atoms in the surface layer being the topmost atom of a PMI and the others filling in the spaces between the PMIs to yield a flat surface.

The terminations found in this structure analysis compare well with the step structure seen in STM (cf. Fig. 45 and Fig. 47). Next, one can try to correlate other surface features seen with STM to local structures in the model favored by LEED. One may speculate, for example, that the fivefold symmetric holes seen with STM (Fig. 45) correspond to Mackay clusters embedded within the topmost layer. Both the fivefold symmetric holes and the Mackay type clusters lie on a Fibonacci pentagrid. With the densely packed surface of Fig. 59b, only the topmost two planes are exposed to the surface, showing up as pentagons with an Al (or Mn) atom in the topmost plane, surrounded by five Al or Pd atoms underneath. These Al/Pd pentagons can be seen for all terminations found by

LEED, and their orientation is always the same. Another fivefold symmetric feature is the deeper and larger fivefold symmetric hole marked by the arrow in Fig. 59b. These holes are also located on the nodes of a Fibonacci pentagrid and have the same orientation for all terminations. Also this feature may give rise to the appearance of the fivefold symmetric holes in STM.

Also for the twofold surface of $Al_{70}Pd_{21}Mn_9$, LEED I(E) calculations have been performed, which led to a very similar result as for the fivefold surface; because of the still unsatisfactory agreement between theory and experiment, the results have, however, to be regarded as preliminary. As for the fivefold surface, also for the twofold surface different terminations of the bulk configuration of $Al_{70}Pd_{21}Mn_9$ have been tested. The geometry found for the twofold surface is depicted in Fig. 61. The topmost layer has a high density and is Al rich. As shown in Fig. 60 (bottom), for the twofold surface, as well as for the fivefold surface, the succession of layer spacings in the surface structure found by LEED and in a Mackay cluster is identical. This provides evidence that many Mackay type clusters are indeed present in the surface region also in the twofold surface, with some of the atoms in the topmost layer being the topmost atom of a Mackay cluster.

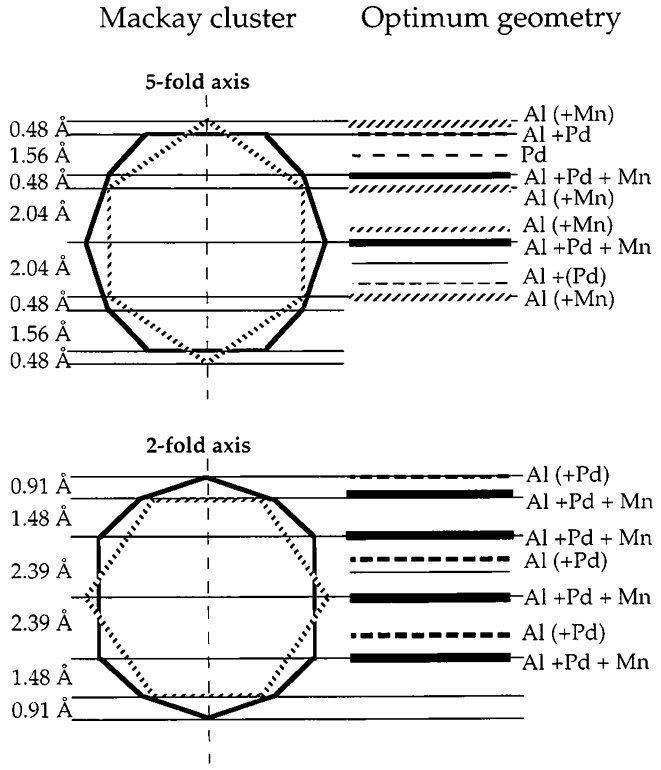

Fig. 60. The geometry of a pseudo Mackay icosahedron oriented along a fivefold (twofold) axis, compared with the layer sequence of the optimum geometry determined in the LEED analysis of the fivefold (twofold) $Al_{70}Pd_{21}Mn_9$ surface. Grey: dodecahedron, black: icosidodecahedron of the PMI (the small dodecahedron, with atoms lying 2.52 Å underneath the topmost atom, is not shown. Each plane of the Mackay cluster has its counterpart in the AlPdMn surface structure. The topmost layer of the structure found by LEED coincides with the topmost plane of many Mackay icosahedra.

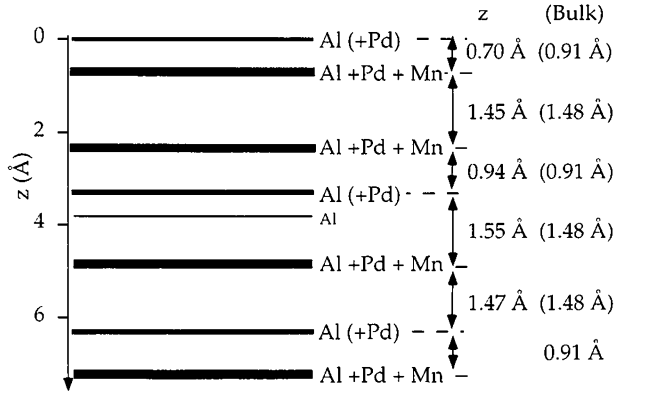

Fig. 61. Optimum geometry found for the twofold $Al_{70}Pd_{21}Mn_9$ surface. Given are the topmost layer spacings, compared with their bulk values (bulk values in parentheses). The planes are drawn at their respective depths z, as bars with thickness proportional to the atomic density in each plane, together with their approximate composition (as labeled below).

The structural analyses described above demonstrate that LEED can be applied to the structural analysis of aperiodic, quasicrystalline structures which cannot be described using a surface unit cell of finite size. The approximations newly developed for the LEED calculations of quasicrystals were applied and checked for the $Al_{70}Pd_{21}Mn_9$ system, but they should work also for other quasicrystals, especially if they consist of weaker scatterers, compared to Mn or Pd as, for example, the icosahedral phases of AlLiCu and AlCuFe.

VI. Conclusions and outlook

In this review we demonstrated that the quantitative analysis of low-energy-electron diffraction LEED data is a very powerful tool to determine the atomic geometry of clean and adsorbate-covered surfaces. Most of the present structural work was performed on well-ordered surfaces and overlayers. It is possible to expand the application of the LEED method to the cases of disordered systems with well-defined local order by analyzing diffuse LEED intensity data [180]. The complexity of surface structures, which have been investigated by LEED, has advanced significantly since the introduction of efficient automated search algorithms [181] and the application of the Tensor LEED approximation [156]. As a consequence, surface structures with several dozens of structural parameters can be treated by LEED although by far not routinely. The main problem in determining complex surface structures is a good initial guess for the surface structure in order to pin down the true structure. In terms of optimization strategies, this represents the familiar problem of finding the global minimum in the (R-factor) hypersurface. Promising global optimization schemes are simulated annealing [182], genetic algorithms [183], or maximum entropy method [184] which was recently applied to surface x-ray diffraction. These methods have, however, to be combined with efficient approximation schemes because otherwise they consume prohibitively much computer time. To make further significant progress in LEED (and generally in surface crystallography), one needs methods which are able to find a good initial guess for the structure model. With SXRD such methods are partially at hand with the two- and three-dimensional Patterson analysis and the Fourier

synthesis [185]. A big advantage of SXRD is also the possibility of breaking up the complexity of a surface structure into less complex pieces. In a first step, the projected in-plane structure of the overlayer slab can be solved by examining in-plane data only. In a second step, the out-of-plane structure of the overlayer slab can be extracted from the fractional order rods, and finally the registry to the bulk like substrate can be determined by using the crystal truncation rods.

Of course, even more attracting would be a direct inversion of diffraction data into three-dimensional atomic coordinates and images. Here we are faced with the so-called phase problem which does not allow to derive the phase information directly from the diffraction amplitude. From optics, however, it is known that phase information can be readily stored via holographic plates which rely on the effect of interference of a reference and an object wave. From this intensity modulation both diffraction amplitude and diffraction phases can be retrieved. The transfer of the holographic idea to diffraction methods in surface science started about 10 years ago [186, 187], and it was considered promising to bring diffraction methods in fashion in comparison to 'direct imaging' methods such as STM. However, up to now, the application of holographic reconstruction methods has been limited to simple and often already known surface structures. Most recently, Heinz and coworkers [188] demonstrated that the conventional LEED method in combination with a holographic reconstruction method is able to supply useful structure information on an unknown surface phase for the special case that the unit cell is large and a single scatterer is dominating the diffraction amplitudes; this situation may, however, not be encountered that frequently.

Another, more traditional approach to narrow down the number of possible structure models is to combine the results of several surface-sensitive methods. In this context, a particularly powerful combination of methods is SXRD and LEED since these techniques are complementary in many respects. We have seen that a long-standing problem, such as the atomic geometry of the Si(111)–(3 × 1) reconstruction, could be resolved by analyzing SXRD and LEED data. Even more important, none of these techniques alone would have been able to determine the complete surface structure. It was just the synergistic effect of both methods which allowed the unequivocal determination of this complex surface geometry.

The future of LEED and also of other diffraction techniques is closely related to the issue of exploring and discovering new and also fashionable fields in surface science. One route could be the investigation of increasingly more complex systems, such as coadsorbate systems and how coadsorbate-induced structural changes are connected with the interaction between the coadsorbed species (cf. paragraph 1). Structure determination of moderately large molecules beyond benzene represents another future prospect. Another exciting track of the LEED method is to extend its application to electrochemically prepared surfaces [189] and to surfaces where strong reactions had taken place. LEED structural investigation under reaction conditions in the mbar range would require the use of a differentially pumped electron gun as already in use for RHEED. Yet, SXRD would be the method of choice if one is going to investigate structural properties at surfaces under high-pressure and also in-situ electrochemical conditions. Further progress in LEED is also connected with structural investigations of new materials like SiC [190], GaN, and quasicrystals (cf. paragraph 4). Temperature-dependent LEED measurements and their proper simulations open the world of very soft adsorbate vibrations, as demonstrated recently [191, 139]. Using short electron pulses in a pump-and-probe way one can combine the spatial domain in LEED with the time domain. Thus, new physical phenomena could be explored, such as the alteration of the atomic geometry of adsorbates upon phononic and electronic excitation.

A further important route for future improvement in LEED concerns the experimental data collection. In order to determine complex structures, one needs a sufficiently large experimental data set. For this reason, it is very helpful to measure also at off-normal incidence at various well-defined angles using a high-precision goniometer. For the structure determination of molecules at surfaces it is necessary to improve the sensitivity of LEED by applying (routinely) either high-sensitive CCD cameras or multichannel plates in order to reduce electron-induced damaging.

Acknowledgments. We are grateful to M. Richard who carefully prepared some of the line drawing.

References

[1] Jona, F.: Low-energy electron diffraction (LEED) spectra: Aluminum. IBM J. Res. Dev. **14** (1970) 444–452.
[2] Jona, F.: Private communication, Sept. 1997.
[3] Pendry, J. B.: Low-Energy Electron Diffraction. Academic Press, London-New York 1974.
[4] Jona, F.; Strozier Jr., J. A.; Yang, W.S.: Low-energy electron diffraction for surface structure analysis. Rep. Prog. Phys, **45** (1982) 527–585.
[5] Van Hove, M. A.; Weinberg, W. H.; Chan, C.-M.: Low-Energy Electron Diffraction. Springer, Berlin-Heidelberg 1986.
[6] Heinz, K.: LEED and DLEED as modern tools for quantitative surface structure determination. Rep. Prog. Phys. **58** (1995) 637–704.
[7] Determination of Surface Structure by LEED, edited by P. M. Marcus and F. Jona, Plenum Press, New York 1984.
[8] Tong, S. Y.; Huang, H.; Wei, C. M.: Bonding and structure on semiconductor surfaces. In: *Chemistry and Physics of Solid Surfaces VIII*, Eds. R. Vanselow and R. Howe. Springer Series in Surface Sciences, Vol. 22. Springer, Berlin 1990, 395–417.
[9] Duke, C. B.: Semiconductor surface reconstruction – The structural chemistry of two-dimensional surface compounds. Chem. Rev. **96** (1996) 1237–1259.
[10] Mönch, W.: Semiconductor Surfaces and Interfaces. Springer, Berlin-Heidelberg 1995.
[11] Waltenburg, H. N.; Yates, J. T.: Surface chemistry of silicon. Chem. Rev. **95** (1995) 1589–1673.
[12] Schlier, R. E.; Farnsworth, H. E.: Structure and adsorption characteristics of clean surfaces of germanium and silicon. J. Chem. Phys. **30** (1959) 917–926.
[13] a) Yin, M. T.; Cohen, M. L.: Theoretical determination of surface atomic geometry: Si(001)–(2 × 1). Phys. Rev. **B24** (1981) 2303–2306; b) Yang, W. S.; Jona, F.; Marcus, P. M.: Atomic structure of Si(001)2 × 1. Phys. Rev. **B28** (1983) 2049–2059; c) Tromp, R. M.; Hamers, R. J.; Demuth, J. E.; Si(001) dimer structure observed with scanning tunneling microscopy. Phys. Rev. Lett. **55** (1985) 1303–1306.

[14] Over, H.; Wasserfall, J.; Ranke, W.; Sawitzki, R.; Ambiatello, C.; Moritz, W.: Surface atomic geometry of Si(001)–2 × 1: A low-energy electron-diffraction structure analysis. Phys. Rev. **B55** (1997) 4731–4736.

[15] Dabrowski, J.; Scheffler, M.: Self-consistent study of the electronic and structural properties of the clean Si(001)–(2 × 1) surface. Appl. Surf. Sci. **56–58** (1992) 15–19.

[16] Krüger, P.; Pollmann, J.: Dimer reconstruction of diamond, Si, and Ge(001) surfaces. Phys. Rev. Lett. **74** (1995) 1155–1158.

[17] Chadi, D. J.: Atomic and electronic structures of reconstructed Si(100) surfaces. Phys. Rev. Lett. **43** (1979) 43–47.

[18] Landmark, E.; Karlsson, C. J.; Chao, Y.-C.; Uhrberg, R. I. G.: Core-level spectroscopy of the clean Si(001) surface: Charge transfer within asymmetric dimers of the 2 × 1 and c(2 × 4) reconstructions. Phys. Rev. Lett. **69** (1992) 1588–1591.

[19] Hamers, R. J.; Köhler, U. K.: Determination of the local electronic structure of atomic-sized defects on Si(001) by tunneling spectroscopy. J. Vac. Sci. Technol. A7 (1989) 2854–2859.

[20] Yin, M. T.; Cohen, M. L.: Theoretical determination of surface atomic geometry: Si(001)–(2 × 1). Phys. Rev. **B24** (1981) 2303–2307.

[21] Tabata, T.; Aruga, T.; Murata, Y.: Order- disorder transition on Si(001): c(4 × 2) to (2 × 1). Surf. Sci. **179** (1987) L63–L70.

[22] Ihm, J.; Lee, D. H.; Jaonnopoulos, J. D.; Xiong, J. J.: Structural phase diagrams for the surface of a solid: A total-energy, renormalization-group approach. Phys. Rev. Lett. **51** (1983) 1872–1875.

[23] Wolkow, R. A.: Direct observation of an increase in buckled dimers on Si(0001) at low temperatures. Phys. Rev. Lett. **68** (1992) 2636–2639.

[24] a) Rossmann, R.; Meyerheim, H. L.; Jahns, V.; Wever, J.; Moritz, W.; Wolf, D.; Dornisch, D.; Schulz, H.: The Ge(001)–(2 × 1) reconstruction: asymmetric dimers and multilayer relaxation observed by grazing incidence X-ray diffraction. Surf. Sci. **279** (1992) 199–209; b) Torrelles, X.; van der Vegt, H. A.; Etgens, V. H.; Fajardo, P.; Alvarez, J.; Ferrer, S.: The structure of the Ge(001)–(2 × 1) reconstruction investigated with X-ray diffraction. Surf. Sci. **364** (1996) 242–252.

[25] a) Craig, B. I.; Smith, P. V.: The structure of the Si(100)2 × 1:H surface. Surf. Sci. **226** (1990) L55–L58; b) Zheng, X. M.; Smith, P. V.: Hydrogen chemisorption on the Si(100) surface. Surf. Sci. **279** (1992) 127–136 and references therein.

[26] Chabal, Y. J. : High-resolution infrared spectroscopy of adsorbates on semiconductor surfaces: Hydrogen on Si(100) and Ge(100). Surf. Sci. **168** (1986) 594–608.

[27] Pflanz, S.; Buchtler, R.; Moritz, W.; Over, H.: Dimer bond geometry in D/Ge(001)–(2 × 1): A LEED structure analysis. Phys. Rev. **B54** (1996) R8313–8316.

[28] Boland, J. J.: Evidence of pairing and its role in the recombinative desorption of hydrogen from the Si(100)–2 × 1 surface. Phys. Rev. Lett. **67** (1991) 1539–1542.

[29] Boland, J. J.: Scanning tunneling microscopy of the interaction of hydrogen with silicon surfaces. Adv. Phys. **42** (1993) 129–171.

[30] a) Feidenhans'l, R.; Pedersen, J. S.; Bohr, J.; Nielsen, M.; Grey, F.; Johnson, R. L.: Surface structure and long-range order of the Ge(111)-c(2 × 8) reconstruction. Phys. Rev. **B38** (1988) 9715–9720;
b) van Silfhout, R. G.; van der Veen, J. F.; Norris, C.; Macdonald, J. E.: Structure of the Ge(111)–c(2 × 8) surface as determined from scattered X-ray intensities along crystal truncation rods. Faraday Disc. Chem. Soc. **89** (1990) 169–180.

[31] Takayanagi, K.; Tanishiro, Y.; Takahashi, M.; Takahashi, S.: Structural analysis of Si(111)–7 × 7 by UHV-transmission electron diffraction and microscopy. J. Vac. Sci. Technol. A3 (1985) 1502–1506.

[32] Over, H.; Tong, S. Y.: Chemically adsorbed layers on metal and semiconductor surfaces. In: *Physical Structure. Handbook of Surface Science*, Vol. 1, Chapter 9, Ed. W. N. Unertl. Elsevier, Amsterdam 1996, 425–502.

[33] Ding, Y. G.; Chan, C. T.; Ho, K. M.: Structure of the $(\sqrt{3} \times \sqrt{3})$ R30°–Ag/Si(111) surface from first-principles calculations. Phys. Rev. Lett. **67** (1991) 1454–1457 and references therein.

[34] Takahashi, T.; Nakatani, S.; Okamoto, N.; Ichikawa, I.; Kikuta, S.: Study on the Si(111)–$\sqrt{3} \times \sqrt{3}$–Ag surface structure by X-ray diffraction. Jpn. J. Appl. Phys. **27** (1988) L753–L755.

[35] Dornisch, D.; Moritz, W.; Schulz, H.; Feidenhans'l, R.; Neilsen, M.; Grey, F.; Johnson, R. L.: Au/Si(111): Analysis of the $(\sqrt{3} \times \sqrt{3})$ R30° and 6 × 6 structures by in-plane x-ray diffraction. Phys. Rev. **B44** (1991) 11221–11230.

[36] Quinn, J.; Jona, F.; Marcus, P. M.: Atomic structure of Si(111)–$(\sqrt{3} \times \sqrt{3})$ R30°–Au. Phys. Rev. **B46** (1992) 7288–7291.

[37] Ding, Y. G.; Chan, C. T.; Ho, K. M.: Theoretical investigation of the structure of the $(\sqrt{3} \times \sqrt{3})$ R30°–Au/Si(111) surface. Surf. Sci. **275** (1992) L691–L696.

[38] CRC Handbook of Chemistry and Physics, 67th ed., Ed. R. C. Weast (CRC, Cleveland 1986) F169–F170.

[39] Howes, P. B.; Norris, C.; Finney, M. S.; Vlieg, E.; van Silfout, R. G.: Structure of Ge(111)–$(\sqrt{3} \times \sqrt{3})$ R30°–Au determined by surface x-ray diffraction. Phys. Rev. **B48** (1993) 1632–1642.

[40] Dornisch, D.; Moritz, W.; Schulz, H.; Feidenhans'l, R.; Nielsen, M.; Grey, F.; Johnson, R. L.; Le Lay, G.: Ag on Ge(111): 2d x-ray structure analysis of the $(\sqrt{3} \times \sqrt{3})$ superstructure. Surf. Sci. **274** (1992) 215–221.

[41] Huang, H.; Over, H.; Tong, S. Y.; Quinn, J.; Jona, F.: Atomic geometry of Ge(111)–$\sqrt{3} \times \sqrt{3}$ R30°–Ag determined by low-energy electron diffraction. Phys. Rev. **B49** (1994) 13483–13487.

[42] Over, H.; Wang, C. P.; Jona, F.: Atomic bond configuration of Ge(111)–$(\sqrt{3} \times \sqrt{3})$ R30°–Au: A low-energy electron-diffraction study. Phys. Rev. **B51** (1995) 4231–4235.

[43] Over, H.; Huang, H.; Tong, S. Y.; Fan, W. C.; Ignatiev, A.: Low-energy electron diffraction as a direct identification technique: Atomic structures of Ag- and Li-induced Si(111)–$(\sqrt{3} \times \sqrt{3})$ R30°. Phys. Rev. **B48** (1993) 15353–15357.

[44] Fan, W. C.; Ignatiev, A.: Reconstruction of the clean and metal-adsorbed Ge(111) surface. Phys. Rev. **B40** (1989) 5479–5483.

[45] Over, H.; Wang, C. J.; Jona, F.: The atomic geometry of the Ge(111)–$(\sqrt{3} \times \sqrt{3})$ R30°-Li surface: A LEED analysis. submitted to Phys. Rev. B.

[46] Tikhov, M.; Surnev, L.; Kiskinova, M.: Na-induced (7 × 7)-to-(3 × 1) structural transformation on a Si(111)7 × 7 surface and the resulting passivation of the surface towards interaction with oxygen. Phys. Rev. **B44** (1991) 3222–3225.

[47] Jeon, D.; Hashizume, T.; Sakurai, T.; Willis, R. F.: Structural and electronic properties of ordered single and multiple layers of Na on the Si(111) surface. Phys. Rev. Lett. **69** (1992) 1419–1422.

[48] Weitering, H. H.; DiNardo, N. J.; Perez-Sandoz, R.; Chen, J.; Mele, E. J.: Structural model for the metal-induced Si(111)3 × 1 reconstruction. Phys. Rev. **B49** (1994) 16837–16840.

[49] Wan, K. J.; Lin, X. F.; Nogami, J.: Comparison of the (3 × 1) reconstructions of the Si(111) surface induced by Li and Ag. Phys. Rev. **B46** (1992) 13635–13638.

[50] Weitering, H. H.; Shi, X.; Erwin, S. C.: Band dispersions of the π-bonded chains reconstruction of Si(111)3 × 1–Li: A critical evaluation of theory and experiment. Phys. Rev. **B54** (1996) 10585–10592.

[51] Erwin, S. C.: New structural model for the alkali-induced Si(111)–(3 × 1) reconstructions from first principles. Phys. Rev. Lett. **75** (1995) 1973–1977.

[52] a) Pandey, K. C.: New π-bonded chain model for Si(111)–(2 × 1) surface. Phys. Rev. Lett. **47** (1981) 1913–1917; b) Pandey, K. C.: Reconstruction of semiconductor surfaces: Buckling, Ionicity, and π-bonded chains. Phys. Rev. Lett. **49** (1982) 223–226. c) Himpsel, F. J., Marcus, P. M., Tromp, R., Batra, I. P., Cook, M. R., Jona, F., Liu, H: Structure analysis of Si(111)–2 × 1 with low-energy electron diffraction. Phys. Rev. **B30** (1984) 2257–2259.

[53] a) Fan, W. C.; Ignatiev, A.: Reconstruction of the clean and metal-adsorbed Ge(111) surface. Phys. Rev. **B40** (1989) 5479–5483; b) Fan, W. C.; Ignatiev, A.: Metal-adsorbate induced Si(111)–(1 × 3) reconstruction. Phys. Rev. **B41** (1990) 3592–3595.

[54] Over, H.; Gierer, M.; Bludau, H.; Ertl, G.; Tong, S. Y.: Fingerprinting technique in low-energy electron diffraction. Surf. Sci. **314** (1994) 243–268.
[55] Landemark, E.; Nielsen, M.; Smilgies, D.-M.; Feidenhans'l, R.; Lottermoser, L.; Seehofer, L.; Falkenberg, G.; Johnson, D. L.: Metal-induced Si(111)3 × 1 structures investigated by surface x-ray diffraction. ICSOS-5, Aix en Provence, July 1996.
[56] Over, H.; Gierer, M.; Jona, F.: A new method to solve heavily reconstructed semiconductor surfaces in an iterative way. To be submitted.
[57] Gierer, M.; Kleine, H.; Bludau, H.; Over, H.; Kim, S.K.; Jona, F.: LEED analyses of the Li-induced (3 × 1) reconstructions of SI(111) and Ge(111): A low energy electron diffraction study. To be submitted.
[58] Lottermoser, L.; Landemark, E.; Smilgies, D.-M.; Nielsen, M.; Feidenhans'l, R.; Falkenberg, G.; Johnson, R. L.; Gierer, M.; Seitsonen, A. P.; Kleine, H.; Bludau, H.; Over, H.; Kim, S. K.; and Jona, F.: New bonding configuration on Si(111) and Ge(111) surfaces induced by the adsorption of alkali metals. Phys. Rev. Lett. **80** (1998) 3980–3983.
[59] Harrison, W. A.: Theory of polar semiconductor surfaces. J. Vac. Sci. Technol. **16** (1979) 1492–1496.
[60] Biegelsen, D. K; Bringans, R. D.; Northrup, J. E.; Swartz, L.-E.: Reconstruction of the GaAs($\bar{1}\bar{1}\bar{1}$) surfaces observed by Scanning Tunneling Microscopy. Phys. Rev. Lett. **65** (1990) 452–455.
[61] a) Kaxiras, E.; Bar-Yam, Y.; Jaonnopoulos, J. D.; Pandey, K. C.: Ab initio theory of polar semiconductor surfaces. I. Methodology and the (2 × 2) reconstructions of GaAs(111). Phys. Rev. B **35** (1987) 9625–9635; b) Kaxiras, E.; Bar-Yam, Y.; Jaonnopoulos, J. D.; Pandey, K. C.: II. (2 × 2) reconstructions and related phase transitions of the GaAs($\bar{1}\bar{1}\bar{1}$). Phys. Rev. B**35** (1987) 9636–9643.
[62] Moll, N.; Kley, A.; Pehlke, E.; Scheffler, M.: GaAs equilibrium crystal shape from first principles. Phys. Rev. B**54** (1996) 8844–8855.
[63] Tong, S. Y; Xu, G.; Mei, W. N.: Vacancy-buckling model for the (2 × 2) GaAs(111) surface. Phys. Rev. Lett. **52** (1984) 1693–1696.
[64] Setzer, C.; Platen, J.; Bludau, H.; Gierer, M.; Over, H.; Jacobi, K.: LEED intensity and surface core level shift analysis of the MBE-prepared GaAs($\bar{1}\bar{1}\bar{1}$)B(2 × 2) surface. Surf. Sci. **402–404** (1998) 782–785.
[65] Over, H.; Tong, S. Y.; Quinn, J.; Jona, F.: Refinement of the Si(111)–($\sqrt{3} \times \sqrt{3}$) R30°-Ag structure by low-energy electron diffraction. Surf. Rev. Lett. **2** (1995) 451–457.
[66] Engel, T.; Ertl, G.: Elementary steps in the catalytic oxidation of carbon monoxide on platinum metals. Adv. Catal. **28** (1979) 1–78.
[67] Langmuir, I.: Chemical reactions on surfaces. Trans. Faraday Soc. **17** (1921) 607–620.
[68] Boudart, M.: Catalysis by supported metals. Adv. Catal. **20** (1969) 153–166.
[69] Pirug, G.; Bonzel, H. P.: Interaction between alkali metal absorbates and adsorbed molecules (CO; H_2O). In: *The Chemical Physics of Solid Surfaces*, Vol. 6: *Coadsorption, Promoters, and Poisons*, Eds. D. A. King and D. P. Woodruff. Elsevier, Amsterdam, 1993, 51–111.
[70] Bludau, H.; Over, H.: Unpublished measurements.
[71] Peden, C. H. F.; Goodman, D. W.: Kinetics of CO oxidation over Ru(0001). J. Phys. Chem. **90** (1986) 1360–1365.
[72] Stampfl, C.; Scheffler, M: Theoretical study of O adlayers on Ru(0001). Phys. Rev. B**54** (1996) 2868–2872.
[73] Blyholder, G.: Molecular orbital view of chemisorbed carbon monoxide. J. Phys. Chem. **68** (1964) 2772–2778.
[74] Campuzano, J. C.: The adsorption of carbon monoxide by the transition metals. In: *Chemical Physics of Solid Surfaces and Heterogeneous Catalysis*, Vol. 3a, Eds. D. A. King and D. P. Woodruff. North-Holland, Amsterdam, 1990, 389–469.
[75] Coulston, G. W.; Haller, G. L.: The dynamics of CO oxidation on Pd, Rh, and Pt studied by high-resolution infrared chemiluminescence spectroscopy. J. Chem. Phys. **95** (1991) 6932–6944.
[76] Savchenko, V. I.; Boreskov, G. K.; Kalinkin, A. V.; Salanov, A. N.: State of oxygen on metal surfaces and catalytic activity for the oxidation of carbon monoxide. Catal. **24** (1984) 983–990.
[77] Böttcher, A.; Niehus, H.; Schwegmann, S.; Over, H.; Ertl, G.: CO oxidation over oxygen-rich Ru(0001) surfaces. J. Phys. Chem. **101** (1997) 11185–11191.
[78] Oh, S. H.; Carpenter, J. E.: The oxidation state and catalytic activity of supported rhodium. J. Catal. **80** (1983) 472–478.
[79] Gierer, M.; Barbieri, A.; Van Hove, M. A.; Somorjai, G. A:. Structural reanalysis of the Rh(111)–($\sqrt{3} \times \sqrt{3}$) R30°-CO and Rh(111)–(2 × 2)–3CO phases using automated tensor LEED. Surf. Sci. **391** (1997) 176–182.
[80] Michalk, H.; Moritz, W.; Pfnür, H.; Menzel, D.: A LEED determination of the structures of Ru(001) and of CO/Ru(001)–($\sqrt{3} \times \sqrt{3}$) R30°. Surf. Sci. **129** (1983) 92–106.
[81] Over, H.; Moritz, W.; Ertl, G.: Anisotropic temperature effects in structural analysis by low energy electron diffraction. Phys. Rev. Lett. **70** (1993) 315–318.
[82] Becker, L.; Aminpirooz, S.; Hillert, B.; Pedio, M.; Haase, J.; Adams, D.L.: Threefold-coordinated hollow adsorption site for Ni(111)–c(4 × 2)–O: A surface-extended x-ray-absorption fine-structure study. Phys. Rev. B**47** (1993) 9710–9714.
[83] A. Schiffer, A.; Jakob, P.; Menzel, D.: Präparation und Charakterisierung der (2CO + O)(2 × 2)/Ru(001) Schicht. DPG Frühjahrstagung 1996, Regensburg.
[84] Narloch, B.; Held, G.; Menzel, D.: A LEED-IV determination of the Ru(001)–p(2 × 2)(O + CO) structure: a coadsorbate induced molecular tilt. Surf. Sci. **340** (1995) 159–171.
[85] Narloch, B.; Held, G.; Menzel, D.: Structure rearrangement by coadsorption: a LEED-IV determination of the Ru(001)–p(2 × 2)(2O + O) structure. Surf. Sci. **317** (1994) 131–142.
[86] Schwegmann, S.; Over, H.; De Renzi, V.; Ertl, G.: The atomic geometry of the O and CO + O phases on Rh(111). Surf. Sci. **375** (1997) 91–106.
[87] Beutler, A.; Lundgren, E.; Nyholm, R.; Andersen, J. N.; Setlik, B. J.; Heskett, D.: Coverage and temperature-dependent site occupancy of carbon monoxide on Rh(111) studied by high-resolution core-level photoemission. Surf. Sci. **396** (1998) 117–136.
[88] Fernandez, V.; Schindler, K.-M.; Schaff, O.; Hofmann, Ph.; Theobald, A.; Bradshaw, A.M.; Fritzsche, V.; Davis, R.; Woodruff, D. P.: Structure determination of a CO/O coadsorption phase on Ni(111). Surf. Sci. **351** (1996) 1–12.
[89] Held, G.; Schuler, J.; Sklarek, W.; Steinrück, H.-P.: Determination of adsorption sites of pure and coadsorbed CO on Ni(111) by high-resolution X-ray photoelectron spectroscopy. Surf. Sci. **398** (1998) 154–171.
[90] Over, H.; Held, G.: The atomic geometry of O and CO coadsorbed on Ni(111): Oxygen coadsorption causes CO to switch from threefold hollow to on-top position. Phys. Rev. B (submitted).
[91] Pfnür, H.; Held, G.; Lindroos, M.; Menzel, D.: Oxygen-induced reconstruction of a close-packed surface: a LEED-IV study on Ru(001)–p(2 × 1)–O. Surf. Sci. **220** (1990) 43–58.
[92] Lindroos, M.; Pfnür, H.; Held, G.; Menzel, D.: Adsorbate-induced reconstruction by strong chemisorption: Ru(001)–p(2 × 2)–O. Surf. Sci. **222** (1989) 451–463.
[93] Stampfl, C.; Schwegmann, S.; Over, H.; Scheffler, M.; Ertl, G.: Structure and stability of a high-coverage (1 × 1) oxygen phase on Ru(0001). Phys. Rev. Lett. **77** (1996) 3371–3374.
[94] Schwegmann, S.; Seitsonen, A.P.; De Renzi, V.; Dietrich, H.; Bludau, H.; Gierer, M.; Over, H.; Jacobi, K.; Scheffler, M.; Ertl, G.: Oxygen adsorption on the Ru(1010) surface: structural, vibrational, and energetic properties. Phys. Rev. B**57** (1998) 15487–15495.
[95] Hoffmann, R.: Solids and Surfaces – A Chemist's View of Bonding in Extended Structures. Verlag Chemie, Weinheim, 1988.
[96] Nørskov, J. N.: Chemisorption on metal surfaces. Rep. Prog. Phys. **53** (1990) 1253–1295.
[97] Bludau, H.; Over, H.; Hertel, T.; Gierer, M.; Ertl, G.: Structural aspects of cesium-oxygen phases on Ru(0001). Surf. Sci. **342** (1995) 134–154.
[98] Over, H.; Bludau, H.; Skottke-Klein, M.; Moritz, W.; Ertl, G.: Low-energy-electron diffraction analysis of the structure of a

Cs–O–Ru(0001) coadsorbate phase. Phys. Rev. B**46** (1992) 4360–4363.

[99] Over, H.; Bludau, H.; Skottke-Klein, M.; Moritz, W.; Ertl, G.; Campbell, C. T.: Coverage dependence of adsorption-site geometry in the Cs/Ru(0001) system: A low-energy electron-diffraction analysis. Phys. Rev. B**45** (1992) 8638–8649.

[100] Trost, J.; Wintterlin, J.; Ertl, G.: Atomic scale imaging of a 2D fluid-solid equilibrium for Cs and O coadsorbed on a Ru(0001) surface. Surf. Sci. **329** (1995) L583–L587.

[101] Over, H.; Bludau, H.; Gierer, M.; Ertl, G.: Structural properties of alkali-metal atoms adsorbed on Ru(0001). Surf. Rev. Lett. **2** (1995) 409–422.

[102] Hrbek, J.: Adsorption of Cesium on Ru(001). Surf. Sci. **164** (1985) 139–148.

[103] a) Böttcher, A.; Morgante, A.; Grobecker, R.; Greber, T.; Ertl, G.: Singlet-triplet conversion of metastable He atoms at alkali-metal overlayers. Phys. Rev. B**49** (1994) 10607–16612; b) Fichtner-Endruschat, S.; De Renzi, V.; Morgante, A.; Schwegmann, S.; Bludau, H.; Schuster, R.; Böttcher, A.; Over, H.: Electronic properties of Cs + CO coadsorbed on the Ru(0001) surface. J. Chem. Phys. **108** (1998) 774– 778.

[104] Jacobi, K.; Shi, H.; Gruyters, M.; Ertl, G.: Adsorbate-induced electronic modification of alkali-metal overlayers. Phys. Rev. B**49** (1994) 5733–5736.

[105] Over, H.; Bludau, H.; Kose, R.; Ertl, G.: Structural analysis of Cs + CO coadsorbed on Ru(0001). Phys. Rev. B **51** (1995) 4661–4664.

[106] a) Neugebauer, J.; Scheffler, M.: Adsorbate-substrate and adsorbate-adsorbate interactions of Na and K adlayers on Al(111). Phys. Rev. B**46** (1992) 16067–16080. b) Stampfl, C.; Scheffler, M.: Theory of alkali-metal adsorption on close-packed metal surfaces. Surf. Rev. Lett. **2** (1995) 317–343.

[107] Over, H.; Bludau, H.; Kose, R.; Ertl, G.: Cs and CO coadsorbed on Ru(0001): low-energy electron diffraction analysis. Surf. Sci. **331–333** (1995) 62–68.

[108] Al-Sarraf, N.; Stuckless, J. T.; Wartnaby, C. E.; King, D. A.: Adsorption microcalorimetry and sticking probabilities on metal single crystal surfaces. Surf. Sci. **283** (1993) 427–437.

[109] Christensen, O. B.; Nørskov, J. K.: Modeling the potassium promotion of CO bonding to Ni(100). Chem. Phys. Lett. **214** (1993) 443–446.

[110] Bludau, H.; Schwegmann, S.; Kose, R.; Over, H.; Ertl, G.: Island formation of coadsorbed Cs and CO on Ru(0001). To be submitted to Surf. Sci.

[111] Yang, Y. W.; Hrbek, J.: Oxidation of cesium-modified graphite supported on a Ru(001) surface. J. Phys. Chem. **99** (1995) 3229–3234.

[112] Bludau, H.; Over, H.: Unpublished results.

[113] Steinrück, H. P.: Angle-resolved photoemission studies of adsorbed hydrocarbons. J. Phys. Cond. Matt. **8** (1996) 6465–6509.

[114] a) Bradshaw, A.M.: The structure of adsorbed molecules. Current Opinion in Solid States & Materials Science **2** (1997) 530–538; b) Bradshaw, A.M.: Structural studies of adsorbed molecules and molecular fragments: the surface-cluster analogy re-visited. Surf. Sci. **331–333** (1995) 978–988.

[115] Koel, B. E.; Crowell, J. E.; Mate, C. M.; Somorjai, G. A.: A high-resolution electron energy loss spectroscopy study of the surface structure of benzene adsorbed on the rhodium (111) crystal surface. J. Phys. Chem. **88** (1984) 1988–1996.

[116] Mate, C. M.; Somorjai, G. A.: Carbon monoxide induced ordering of benzene on Pt(111) and Rh(111) crystal surfaces. Surf. Sci. **160** (1985) 542–560.

[117] Neumann, M.; Mack, J. U.; Bertel, E.; Netzer, F. P.: The molecular structure of benzene on Rh(111). Surf. Sci. **155** (1985) 629–638.

[118] Bertel, E.; Rosina, G.; Netzer, F. P.: The structure of benzene on Rh(111): coadsorption with CO. Surf. Sci. Lett. **172** (1986) L515–L522.

[119] Huber, W.; Zebisch, P.; Bornemann, T.; Steinrück, H. P.: Lateral interactions and azimuthal orientation of pure and coadsorbed benzene layers on Ni(111). Surf. Sci. **258** (1991) 16–22.

[120] Schaff, O.; Fernandez, V.; Hofmann P.; Schindler, K.-M, Theobald, A.; Fritzsche, V.; Bradshaw, A.M.; Davis, R.; Woodruff, D. P.: Coverage-dependent changes in the adsorption geometry of benzene on Ni(111). Surf. Sci. **348** (1996) 89–99.

[121] Held, G.; Bessent, M. P.; Titmuss, S.; King, D. A.: Realistic molecular distortions and strong substrate buckling induced by the chemisorption of benzene on Ni(111). J. Chem. Phys. **105** (1996) 11305–11312.

[122] Wander, A.; Held, G.; Hwang, R. Q.; Blackmann, G. S.; Xu, M. L.; de Andres, P.; Van Hove, M. A.; Somorjai, G. A.: A diffuse LEED study of the adsorption structure of disordered benzene on Pt(111). Surf. Sci. **249** (1991) 21–34.

[123] Saldin, D. K.; Pendry, J. B.; Van Hove, M. A.; Sormorjai, G. A.: Interpretation of diffuse low-energy electron diffraction intensities. Phys. Rev. B**31** (1985) 1216–1218.

[124] Stellwag, C.; Held, G.; Menzel, D.: The geometry of ordered benzene layers on Ru(0001). Surf. Sci. **325** (1995) L379–L384.

[125] a) Ohtani, H.; Van Hove, M. A.; Somorjai, G. A.: Molecular structure of benzene coadsorbed with CO on Pd(111): A dynamical LEED analysis. J. Phys. Chem. **92** (1988) 3974–3982; b) Ohtani, H.; Van Hove, M. A.; Somorjai, G. A.: The structure of benzene coadsorbed with CO on Pd(111): a dynamical low-energy electron diffraction study. J. Vac. Sci. Technol. A**6** (1988) 633–634.

[126] Barbieri, A.; Van Hove, M. A.; Somorjai, G. A.: Benzene coadsorbed with CO on Pd(111) and Rh(111): detailed molecular distortions and induced substrate relaxations. Surf. Sci. **306** (1994) 261–268.

[127] Sesselmann, W.; Woratschek, B.; Ertl G.: Low temperature formation of benzene from acetylene on a Pd(111) surface. Surf. Sci. **130** (1983) 245–258.

[128] Tysoe, W. T.; Nyberg, G. L.; Lambert, R. M.: Photoelectron spectroscopy and heterogeneous catalysis: benzene and ethylene from acetylene on palladium (111). Surf. Sci. **135** (1983) 128–146.

[129] Menzel D.: Adsorbate-induced global and local expansions and contractions of a close-packed transition metal surface. Surf. Rev. Lett. **4** (1997) 1283–1289.

[130] Strisland, F.; Beutler, A.; Jaworowski, A. J.; Nyholm, R.; Setlik, B.; Heskett, D.; Andersen, J. N.: Adsorption sites in coadsorption systems determined by photoemission spectroscopy: K and CO coadsorbed on Rh(111). Surf. Sci. **410** (1998) 330–343.

[131] Orgletree, D. F.; Van Hove, M. A.; Somorjai, G. A.: LEED intensity analysis of the structures of clean Pt(111) and of CO adsorbed on Pt(111) in the c(2 × 4) arrangement. Surf. Sci. **173** (1986) 351–365.

[132] Ohtani, H.; Van Hove, M. A. Somorjai, G. A.: LEED intensity analysis of the surface structures of Pd(111) and of CO adsorbed on Pd(111) in a $(\sqrt{3} \times \sqrt{3})$ R30° arrangement. Surf. Sci. **187** (1987) 372–386.

[133] Stichler, M.; Weimar, R.; Menzel, D.: The influence of electronegative coadsorbates on the geometry of benzene on Ru(001). Surf. Sci. **384** (1997) 179–191.

[134] Starke, U.; Barbieri, A.; Materer, N.; Van Hove, M. A.; Somorjai, G. A.: Ethylidyne on Pt(111): determination of adsorption site, substrate relaxation and coverage by automated tensor LEED. Surf. Sci. **286** (1993) 1–14.

[135] Wander, A.; Van Hove, M. A.; Somorjai, G. A.: Molecule-induced displacive reconstruction in a substrate surface: Ethylidyne adsorbed on Rh(111) studied by low-energy-electron diffraction. Phys. Rev. Lett. **67** (2992) 626–629.

[136] Hofmann P.; Schaff, O.; Schindler, K. M.: Spatial Probability distribution of adsorbate atoms. Phys. Rev. Lett. **76** (1996) 948–951.

[137] a) Baddeley, C. J.; Lee, A. F.; Lambert, R. M.; Gießel, T.; Schaff, O.; Fernandez, V.; Schindler, K.-M.; Theobald, A.; Hirschmugl, C. J.; Lindsay, R.; Bradshaw, A. M.; Woodruff, D. P.: Photoelectron diffraction study of a catalytically active overlayer: C_2H_2 on Pd(111). Surf. Sci. **400** (1998) 166–175; b) Schwegmann, S.; Janssens, T. V. W, Over, H.: The adsorption geometry of acetylene on Pd(111). To be published.

[138] Gentle, T. M.; Muetterties, E. L.: Acetylene, ethylene, and arene chemistry of palladium surfaces. J. Phys. Chem. **87** (1983) 2469–2472.

[139] Moritz, W.; Landskron, J.; Grünberg, T.: Analysis of thermal vibrations and incommensurate layers by low energy electron diffraction. Surf. Rev. Lett. **4** (1997) 469–478.

[140] Jona, F.; Marcus, P. M.: LEED and epitaxy. In: *Surface Physics and Related Topics*, Eds. F. J. Yang, G. J. Ni, X. Wang, K. M. Zhang, and D. Lu (World Scientific, Singapore, 1990) 213–239 and references therein.

[141] Shih, H. D.; Jona, F.; Jepsen, D. W.; Marcus, P. M.: Low energy electron-diffraction determination of successively deposited ordered layers of Cd on Ti(0001): I. The first layer. Phys. Rev. **B15** (1977) 5550–5560. II: Second, third, and fourth layers. Phys. Rev. **B15** (1977) 5561–5566.

[142] Müller, S.; Bayer, P.; Reischl, C.; Heinz, K.; Feldmann, B.; Zillgen, H.; Wuttig, M.: Structural instability of ferromagnetic fcc Fe films on Cu(100). Phys. Rev. Lett. **74** (1995) 765–768.

[143] Müller, S.; Kostka, G.; Schäfer, T.; De la Figuera, J.; Prieto, J. E.; Ocal, C.; Miranda, R.; Heinz, K.; Müller, K.: The structure of Co films on Cu(111) up to 15 ML. Surf. Sci. **352–354** (1996) 46–49.

[144] Müller, S.; Schulz, B.; Kostka, G.; Farle, M.; Heinz, K.; Baberschke, K.: Pseudomorphic growth of Ni films on Cu(001): a quantitative LEED analysis. Surf. Sci. **364** (1996) 235–241.

[145] Schwegmann, S.; Over, H.; Gierer, M.; Ertl, G.: Initial growth of Mg films on Ru(0001): An efficient approximation scheme for the LEED analysis of incommensurate structures. Phys. Rev. B **53** (1996) 11164–11169.

[146] Over, H.; Hertel, T.; Bludau, H.; Pflanz, S.; Ertl, G.: Epitaxial growth of magnesium on Ru(0001). Phys. Rev. **B48** (1993) 5572–5578.

[147] Gierer, M.; Over, H.; Bludau, H.; Ertl, G.: Incommensurate structures and epitaxial growth of Li on Ru(0001): a quantitative low-energy electron diffraction study. Phys. Rev. **B52** (1995) 2927–2934.

[148] a) Pearson, W. B.: A Handbook of Lattice Spacings and Structures of Metals and Alloys. Pergamon, London 1985; b) Gmelins Handbuch der anorganischen Chemie; Lithium-Ergänzungsband (Verlag Chemie, Weinheim, 1960); c) Overhauser, A. W.: Crystal structure of lithium at 4.2 K. Phys. Rev. Lett. **53** (1984) 64–65.

[149] Sprunger, P. T.; Pohl, K.; Davis, H. L.; Plummer, E. W.: Multilayer relaxation of the Mg(0001) surface. Surf. Sci. **297** (1993) L48–L54.

[150] Wright A. F.; Feibelman, P. J.; Atlas, S. R.: First principles calculation of the Mg(0001) surface relaxation. Surf. Sci. **302** (1994) 215–222.

[151] Physics and Chemistry of Alkali Metal Adsorption, Eds. H. P. Bonzel, G. Ertl, A. M. Bradshaw. Elsevier, Amsterdam 1989.

[152] Diehl, R.; McGrath R.: Structural studies of alkali metal adsorption and coadsorption on metal surfaces. Surf. Sci. Rep. **23** (1996) 43–171.

[153] Hertel, T.; Over, H.; Bludau, H.; Gierer, M.; Ertl, G.: Na adsorption on Ru(0001): a low-energy electron diffraction analysis of three ordered phases. Surf. Sci. **301** (1995) 1–10.

[154] Itchkawitz, B. S.; Baddorf, A. P.; Davis, H. L.; Plummer, E. W.: Shear displacement of the K(110) surface. Phys. Rev. Lett. **68** (1992) 2488–2491.

[155] Fuhrmann, D. Hulpke, E.; Steinhögl, W.: Successive multilayer desorption from ultrathin alkali-metal films studied with helium-atom scattering. Phys. Rev. **57** (1998) 4798–4804.

[156] Rous, P. J.: The tensor LEED approximation and surface crystallography by low-energy electron diffraction. Prog. Surf. Sci. **39** (1992) 3–63.

[157] Van Hove, M. A.; Lin, R.; Somorjai, G.A.: Efficient scheme for calculation of low-energy electron-diffraction intensities in the presence of large superlattices, with application to the structural analysis of benzene adsorbed on Rh(111). Phys. Rev. Lett. **51** (1983) 778–781.

[158] Shechtman, D.; Blech, I.; Gratias, D.; Kahn, W.: Metallic phase with long-range orientational order and no translational symmetry. Phys. Rev. Lett. **53** (1984), 1951–1953.

[159] a) Schaub, T. M.; Bürgler, D. E.; Güntherodt, H. J.; Suck, J. B.: Quasicrystalline structure of icosahedral $Al_{68}Pd_{23}Mn_9$ resolved by scanning tunneling microscopy. Phys. Rev. Lett. **73** (1994) 1255–1258. b) Schaub, T. M.; Bürgler, D. E.; Güntherodt, H. J.; Suck, J. B.: Investigation of icosahedral $Al_{68}Pd_{23}Mn_9$ by LEED and STM. Z. Phys. **B96** (1994) 93–96. c) Schaub, T. M.; Bürgler, D. E.; Güntherodt, H. J.; Suck, J. B.: The surface structure of icosahedral $Al_{68}Pd_{23}Mn_9$ measured by STM and LEED. Appl. Phys. **A61** (1995) 491–501.

[160] Jenks, C. J.; Delaney, D.; Bloomer, T.; Chang, S. L.; Lograsso, T.; Thiel, P. A.: Preparation of well-defined samples of AlPdMn quasicrystals for surface studies. Appl. Surf. Sci. **103** (1996) 485–493.

[161] Dubois, J. M.: A survey of the potential applications of quasicrystals. In: New Horizons in Quasicrystals; Research and Applications, Eds. A. I. Goldman, D. J. Sordelet, P. A. Thiel, and J. M. Dubois. World Scientific, Singapore 1996, 208–215.

[162] a) Gierer, M.; Van Hove, M. A.; Goldman, A. I.; Shen, Z.; Chang, S. L.; Jenks, C. J.; Zhang, C. M.; Thiel, P. A.: Structural analysis of the fivefold surface of the $Al_{70}Pd_{21}Mn_9$ quasicrystal by low energy electron diffraction. Phys. Rev. Lett. **78** (1997) 467–470. b) Gierer, M.; Van Hove, M. A.; Goldman, A. I.; Shen, Z.; Chang, S. L.; Pinhero, P. J.; Jenks, C. J.; Anderegg, J. W.; Zhang, C. M.; Thiel, P. A.: The 5-fold surface of quasicrystalline AlPdMn: Structure determination with low-energy electron diffraction. Phys. Rev. B **57** (1998) 7628–7641.

[163] Tsai, A. P.; Inoue, A.; Masumoto, T.: A stable quasicrystal in Al–Cu–Fe system. Japan. J. Appl. Phys. **26** (1987) L1505–L1507.

[164] a) Tsai, A. P.; Inoue, A.; Yokoyama, Y.; Masumoto, T.: Stable icosahedral Al–Pd–Mn and Al–Pd–Re alloys. Mater. Trans. Jpn. Inst. Met. **31** (1990) 98–103; b) Tsai, A. P.; Inoue, A.; Yokoyama, Y.; Masumoto, T.: New icosahedral alloys with superlattice order in the Al–Pd–Mn system prepared by rapid solidification. Phil. Mag. Lett. **61** (1990) 9–14.

[165] a) De Boissieu, M.; Durandcharre, M.; Bastie, P.; Carabelli, A.; and others: Centimetre-size single grain of the perfect Al–Pd–Mn icosahedral phase. Philos. Mag. Lett. **65** (1992) 147–153; b) Lograsso, T.; Delaney, D. W.: Preparation of large single grains of the quasicrystalline Al–Cu–Fe phase. J. Mater. Res. **11** (1996) 2125–2127.

[166] a) Goldman, A. I.; Widom, M.: Quasicrystal structure and properties. Annu. Rev. Phys. Chem. **42** (1991) 685–729. b) Tsai, A. P.: The path to discovering new quasicrystals. In: *New Horizons in Quasicrystals: Research and Applications*. Eds. A. I. Goldman, D. J. Sordelet, P. A. Thiel, and J. M. Dubois. World Scientific, Singapore 1996, 1–8.

[167] Boudard, M.; De Boissieu, M.; Janot, C.; Heger, G.; Beeli, C.; Nissen, H. U.; Vincent, H.; Ibberson, R.; Audier, M.; Dubois, J. M.: Neutron and X-ray single crystal study of the AlPdMn icosahedral phase. J. Phys. C **4** (1992) 10149–10168.

[168] Shen, Z.; Jenks, C. J.; Anderegg, J.; Delaney, Lograsso, T.A.; Thiel, P. A.; Goldman, A. I.: Structure and stability of the twofold surface of icosahedral Al–Pd–Mn by low-energy electron diffraction and X-ray photoelectron spectroscopy. Phys. Rev. Lett. **78** (1997) 1050–1053.

[169] Shen, Z.; Pinhero, P. J.; Lograsso, T. A.; Delaney, D. W.; Jenks, C. J.; Thiel, P. A.: The fivefold surface of quasicrystalline AlCuFe: preparation and characterization with LEED and AES. Surf. Sci. **385** (1997) L923–L929.

[170] He, L. X.; Wu, Y. K.; Meng, X. M.; Kuo, K. H.: Stable AlCuCo decagonal quasicrystals with decaprism solidification morphology. Phil. Mag. Lett. **61** (1990) 15–20.

[171] McRae, E. G.; Malic, R. A.; Lalonde, T. H.; Thiel, F. A.; Chen, H. S.; Kortan, A. R.: Observation of quasicrystal surface order and disordering by low-energy electron diffraction. Phys. Rev. Lett. **65** (1990) 883–886.

[172] a) Janot, C.; DeBoissieu, M.; Dubois, J. M.; Pannetier, J.: Icosahedral crystals: neutron diffraction tells you where the atoms are. J. Phys. C **1** (1989) 1029–1048; b) Steurer, W.: The structure of quasicrystals. Z. Kristallogr. **190** (1990) 179–234.

[173] a) Levine, D.; Steinhardt, P. J.: Quasicrystals: I. Definition and structure. Phys. Rev. **B34** (1986) 596; b) Yamamoto, A.: Crystallography of quasiperiodic crystals. Acta Crystallogr. **A52** (1996) 509–560.

[174] Naumovic, D.; Aebi, P.; Schlapbach, L.; Beeli, C.; Lograsso, T. A.; Delaney, D. W.: Study of the 5-fold and 2-fold i-AlPdMn surfaces by full-hemispherical X-ray photoelectron diffraction. In: Proc. 6th Int. Conf. in Quasicrystals (ICQS), Eds. T. Fujiwara, S. Takeuchi. World Scientific, Singapore, in press.

[175] DeBoissieu, M.; Stephens, P.; Boudard, M.; Janot, C.; Chapman, D. L.; Audier, M.: Disorder and complexity in the atomic structure of the perfect icosahedral alloy Al-Pd-Mn. Phys. Rev. Lett. **72** (1994) 3538–3541.

[176] Yamamoto, A.; Sato, A.; Kato, K.; Tsai, A. P.; Masumoto, T.: An ideal structure of icosahedral Al–Pd–Mn quasicrystals. Mat. Sci. Forum **150–151** (1994) 211–222.

[177] Ebert, P.; Feuerbacher, M.; Tamura, N.; Wollgarten, M.; Urban, K.: Evidence for a cluster-based structure of AlPdMn single quasicrystals. Phys. Rev. Lett. **77** (1996) 3827–3830.

[178] Ebert, P.; Yue, F.; Urban, K.: Surface structures of cleaved icosahedral Al-Pd-Mn single quasicrystals after heat treatment. Phys. Rev. B, in print.

[179] a) Miedima, A. R.. Z. Metallk. **69** (1978) 455; b) Miedima, A. R.; deBoer, F. R.; Boom, R. Calphad **1** (1977) 341.

[180] Starke, U.; Pendry J. B.; Heinz, H.: Diffuse low-energy electron diffraction. Prog. Surf. Sci. **52** (1996) 53–124.

[181] Van Hove, M. A.; Moritz, W.; Over, H.; Rous, P. J.; Wander, A.; Barbieri, A.; Materer, N.; Starke, U.; Somorjai, G. A.: Automated determination of complex surface structures by LEED. Surf. Sci. Rep. **19** (1993) 191–229.

[182] Rous, P. J.: A global approach to the search problem in surface crystallography by low-energy electron diffraction. Surf. Sci. **296** (1993) 358–373.

[183] Döll, R.; Van Hove, M. A.: Global optimization in LEED structure determination using genetic alogorithms. Surf. Sci. **355** (1996) L393–L398.

[184] Vogler, H.; Moritz, W.: Maximum entropy method applied to surface x-ray diffraction. To be published.

[185] Robinson, I. K.; Tweet, D. J.: Surface x-ray diffraction. Rep. Prog. Phys. **55** (1992) 599–651.

[186] Szöke, A.: X-ray and electron holography using a local reference beam. In: *Short Wavelength Coherent Radiation: Generation and Applications*, Eds. D. T. Attwood and K. Bower, AIP Conf. Proc. No. 147 (AIP, New York, 1986) 361–367.

[187] Barton, J. J.: Photoelectron holography. Phys. Rev. Lett. **61** (1988) 1356–1359.

[188] Reuter, K.; Bernhardt, J.; Wedler, H.; Schardt, J.; Starke, U.; Heinz, H.: Holographic image reconstruction from electron diffraction intensities of ordered superstructures. Phys. Rev. Lett. **79** (1997) 4818–4821.

[189] Bludau, H.; Wu, K.; Zei, M. S.; Eiswirth, M.; Over, H.; Ertl, G.: The structure of the underpotential deposition of copper onto Pt(111) in the presence of chloride anions: a LEED analysis. Surf. Sci. **402–404** (1998) 786–789.

[190] Starke, U.: Atomic structure of hexagonal SiC surfaces. Phys. Stat. Sol. B**202** (1997) 475–499.

[191] Over, H.; Gierer, M.; Bludau, H.; Ertl, G.: Anisotropic thermal displacements of adsorbed atoms and molecules on surfaces studied by low-energy electron diffraction. Phys. Rev. B**52** (1995) 16812–16829.